Surface Effect Ferromagnetism in Pure and Reduced Strontium Titanate

by

Brandon DesRoches

Dip., Algonquin College, 2004
B.Sc., Wilfred Laurier University, 2007

A THESIS SUBMITTED IN PARTIAL FULFILMENT OF
THE REQUIREMENTS FOR THE DEGREE OF

MASTER OF SCIENCE

in

The Faculty of Mathematics and Sciences

Department of Physics

BROCK UNIVERSITY

July 5, 2010

In presenting this thesis in partial fulfilment of the requirements for an advanced degree at the Brock University, I agree that the Library shall make it freely available for reference and study. I further agree that permission for extensive copying of this thesis for scholarly purposes may be granted by the head of my department or by his or her representatives. It is understood that copying or publication of this thesis for financial gain shall not be allowed without my written permission.

(Signature) _____

Department of Physics

Brock University
St.Catharines, Canada

Date _____

Abstract

A room temperature ferromagnetic hysteresis is observed in single crystal strontium titanate substrates as purchased from several manufacturers. It was found that polishing all sides of the substrates removed this observed hysteresis, suggesting that the origin of the ferromagnetic behavior resides on the surface of the substrates. X-ray diffraction and energy dispersive x-ray spectra were measured however they were unable to detect any impurity phases. In similar semiconducting oxides it was previously suggested that ferromagnetism could originate in oxygen vacancies or from disorder within the single crystal. To this end substrates were annealed in both air and vacuum in a range of temperatures (600°C to 1100°C) to both create bulk oxygen vacancies and to heal surface damage. Annealing in vacuum was found to create a measureable number of oxygen vacancies however their creation could not be correlated to the ferromagnetic signal of the substrate. Annealing in air was found to effect the remnant moment of the substrate as well as the width of the x-ray diffraction peaks on the unpolished face, weakly suggesting a relation between surface based disorder and ferromagnetism. Argon ion bombardment was employed to create a layer of surface disorder in the polished crystal, however it was not found to induce ferromagnetism. It was found that acid etching was sufficient to remove the ferromagnetism from as purchased samples and similarly simulated handling with stainless steel tweezers was sufficient to re-create the ferromagnetism. It is suggested that the origin of this ferromagnetism in $SrTiO_3$ is surface contaminants (mainly iron).

Contents

List of Tables

List of Figures

Acknowledgements

I would like to take this opportunity to express my thanks to those who helped me with various aspects of conducting research and the writing of this thesis. First and foremost, I would like to thank Dr. David Crandles, for his guidance, patience and support throughout the research for and the writing of this thesis. Secondly, I would like to thank Dr. Fereidoon Razavi for his assistance with various experimental techniques used during my research. I would also like to thank all of the staff in the physics department for making my studies at Brock enjoyable and informative. Finally I would like to thank to my family and friends for their support throughout my studies here at Brock.

Chapter 1

Introduction

1.1 Spintronics

Spintronics (or magneto-electronics) is a recent branch of technology that takes advantage of an electron's intrinsic spin, as opposed to its charge, as a means of transferring information [1]. A spintronic device requires a means of spin-polarizing electrons in either an 'up' or 'down' state, commonly called the spin injector. This is accomplished by creating an imbalance in the number of electrons with a particular spin. This imbalance of electron spins occurs naturally in ferromagnetic (henceforth referred to as FM) materials [2, 3]. These natural imbalances stem from the shift in energy of the density of states that is available to the spin up and spin down electrons. Figure 1.1 shows this relative imbalance when compared to a normal (non- FM) metal, with the arrows indicating the direction of electron spin.

This current of spin polarized electrons can then be injected into semiconducting materials for use. When this spin polarized current is incident on the ferromagnetic metal/semiconductor barrier a significant amount of spin-scattering has been observed, as a result, several methods for injecting these electrons into the semiconductors have been devised [1]. These methods include ohmic contact injection, where the metal is evaporated onto the surface of the semiconductor. However, the contacts from the heavy doping of the semiconductor lead to high spin-scattering and the loss of much of the spin polarization. Recent work into these ohmic contacts has found

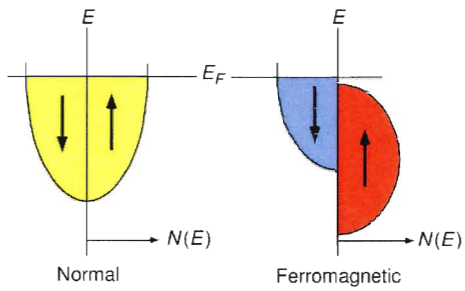

Figure 1.1: **The density of states available in a normal metal and a ferromagnetic metal. The arrows indicate the direction of electron spin. Electron energy (E), Fermi level (E_F) and density of states, N(E), are shown [2].**

that the scattering is less drastic if the conductivities of the ferromagnet and semiconductor are equal [3, 4, 5]. Tunneling injection has also been investigated through the use of FM scanning tunneling microscopy in vacuum [1] and through the use of Schottky barriers [6]. It has been found that the use of electron tunneling removes the spin-scattering dependence on the conductivity difference between the metal and semiconductor [6]. With no spin-scattering stemming from a conductivity mismatch, spin polarization is conserved. Work has also been done with electrons in the ballistic regime (where the mean free path of the electron is greater then the size of the contact), once again to avoid the conductivity mismatch problem. In order for the spin polarized electrons to be transferred successfully to the semiconductor in the ballistic regime they must not be elastically scattered back into the ferromagnet [1, 7]. This elastic scattering can be determined by the difference in the two spin conduction bands of the ferromagnet and the conduction band of the semiconductor [1, 3, 5]. Transferring electrons in the ballistic regime involves the use of a three dimensional ballistic point contact at the ferromagnet/semiconductor interface [1]. A fourth type of electron injection utilizes electrons with energies well above the Fermi level (E_F),

or so called 'hot' electrons. These hot electrons tunnel into the FM where the mean inelastic free path between the spin up and spin down electrons differs greatly [1, 8]. Thus, it is possible to construct ultra thin FM layers such that the mean free path for the majority spin electrons is greater than the layer width while the mean free path for the minority spin electrons is less than the layer width [1]. Through the application of a sufficient number of these ultrathin layers a significant amount of electron polarization can be obtained [8]. These polarized electrons can then be injected directly into the semiconductor with a transmission/reflection probability determined by the band structures of the materials used. Further information on Spintronics can be found in references [9] and [10].

1.2 Dilute Magnetic Semiconductors

As previously mentioned, a large problem with spin dependent systems comes from the metal/semiconductor interface. For a spintronic device to be a successful in todays semiconducting electronics it must be able to be incorporated without the problem of spin-scattering at the FM/semiconductor interface. To this end, work has been done to create FM semiconductors. This work has focused on semiconductors doped with magnetic impurities (Co^{2+}, Mn^{2+}, Fe^{2+}, etc). The first of such materials studied were type II-VI semiconductors, as these semiconductors can readily accept a large concentration of transition metal impurities [11]. Semiconductors doped in this fashion are called dilute magnetic semiconductors (DMS).

In the past two decades research included type III-V semiconductors, doped with various amounts of the same magnetic impurities. One of the primary type III-V semiconductors studied was GaAs doped with Mn. As seen in figure 1.2 small concentrations of 3.5 atomic percent Mn give the GaAs semiconductor a very clear

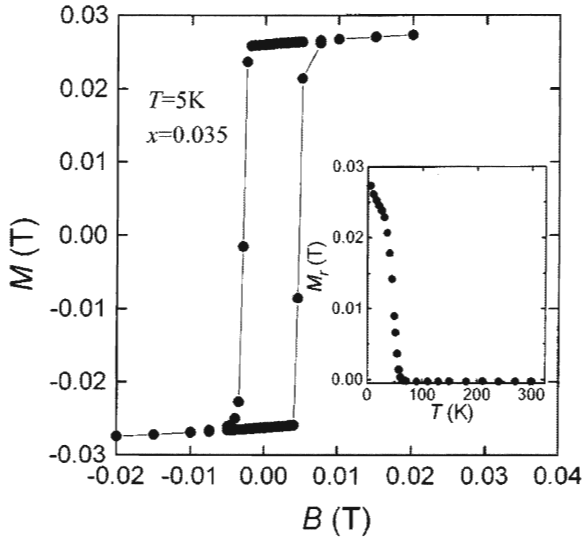

Figure 1.2: **Magnetization of $Ga_{1-x}Mn_xAs$ thin film doped with an Mn content of 0.035. Inset shows temperature dependence of remnant magnetization. [11].**

hysteresis. The downside to the $Ga_{1-x}Mn_xAs$ however is that it only operates as a ferromagnet at low temperatures (inset in figure 1.2).

1.3 Dilute Magnetic Semiconducting Oxides

More recently, in the past decade, research on DMS materials has shifted to include semiconducting oxides (HfO_2, TiO_2, ZnO, etc) [12, 13, 14, 15, 16, 17, 18]. These oxides were originally doped with small concentrations of magnetic impurities. The doped oxides would exhibit a FM response, but only when a certain concentration of doped ions were present, the doping was done under a certain pressure [15] and the temperature of the doped oxide growth was within a narrow range of temperatures [13, 16].

One of the semiconducting oxides (type II-VI) that has attracted a fair bit of

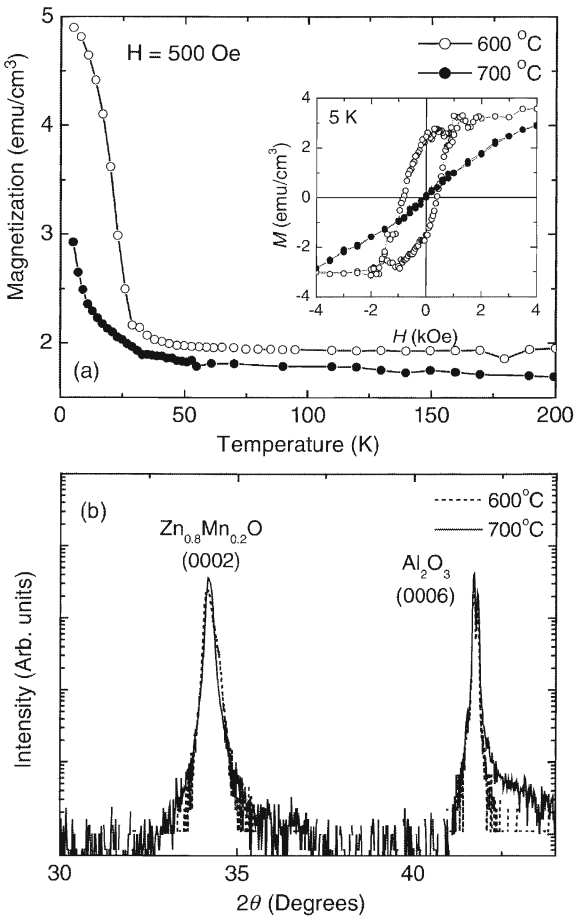

Figure 1.3: **(a)Magnetization of two $Zn_{0.8}Mn_{0.2}O$ samples grown at different temperatures and (b) x-ray diffraction patterns for the above samples [16].**

attention is ZnO when doped with Mn. When doped to properly create a FM material it exhibits room temperature ferromagnetism [16, 18], making it potentially useful for spintronic applications. However, the growth temperature has a significant effect on the final magnetic properties of the sample. This can be seen in figure 1.3 for $Zn_{0.8}Mn_{0.2}O$ where the upper panel shows a magnetometer response for two samples, with a clear hysteresis being visible for the sample prepared at 600°C but not being present for the second sample prepared at 700°C. The lower panel shows

x-ray diffraction data for the same samples, showing that they consist of the same material. It has been suggested that FM in these oxides is related to 'grouping or 'clumping of the impurities [13, 14, 16, 17]. The impurity rich regions have been observed through a variety of experimental techniques such as x-ray scattering and atomic force microscopy.

1.4 Ferromagnetic Oxides without Magnetic Impurities

The nature of ferromagnetism in oxides was originally attributed to holes created by the act of doping, however, more recent work has brought that into question [12, 18]. It has been observed that the ferromagnetism still persists in the oxide samples without intentionally doped magnetic impurities [12, 18]. One of the most intensively studied FM oxides was hafnium dioxide (HfO_2). As hafnium dioxide has a closed electron shell structure (Hf^{4+} and $2O^{2-}$) it should be diamagnetic as discussed in section 2.1.2. However, it has been observed that thin films of hafnium dioxide do have a FM moment as seen in figure 1.4. The lower panel of this figure shows a clean FM hysteresis when the diamagnetic contribution is removed. Several HfO_2 samples of different thicknesses were measured in the same method and it was found that the magnitude of the FM moment did not depend on the thickness of the film. This suggests that the FM is a surface rather than a bulk effect. This FM is thought to originate in lattice defects, such as oxygen or hafnium vacancies. Experimental results such as those seen in figure 1.5 which use similar reduction and oxidization procedures to sections 3.6.1 and 4.8, support this idea that the FM is defect based. This result however is the subject of debate as others [13, 19] have performed magnetometry measurements on hafnium dioxide samples and have not seen any FM moment.

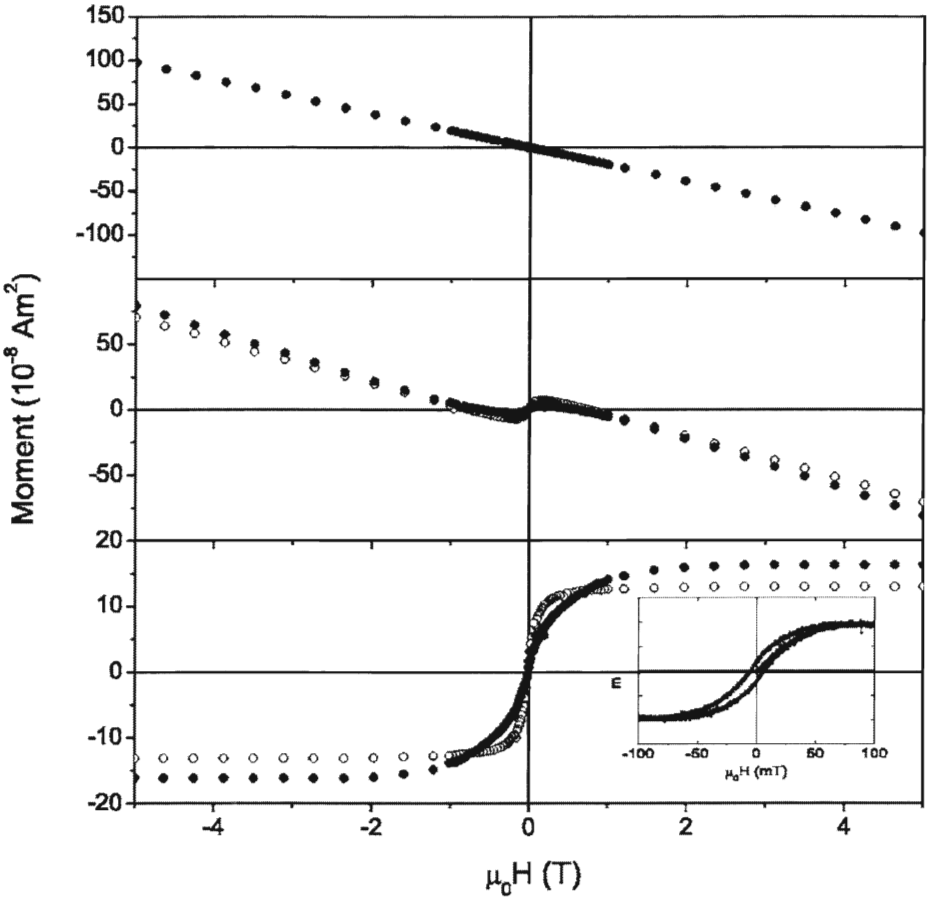

Figure 1.4: **Measured magnetic moment of sapphire substrate (top), substrate with 82nm film of HfO_2 (middle) and ferromagnetic moment of HfO_2 film (bottom). (•) Sample perpendicular to applied field, (○) sample parallel to applied field. [12].**

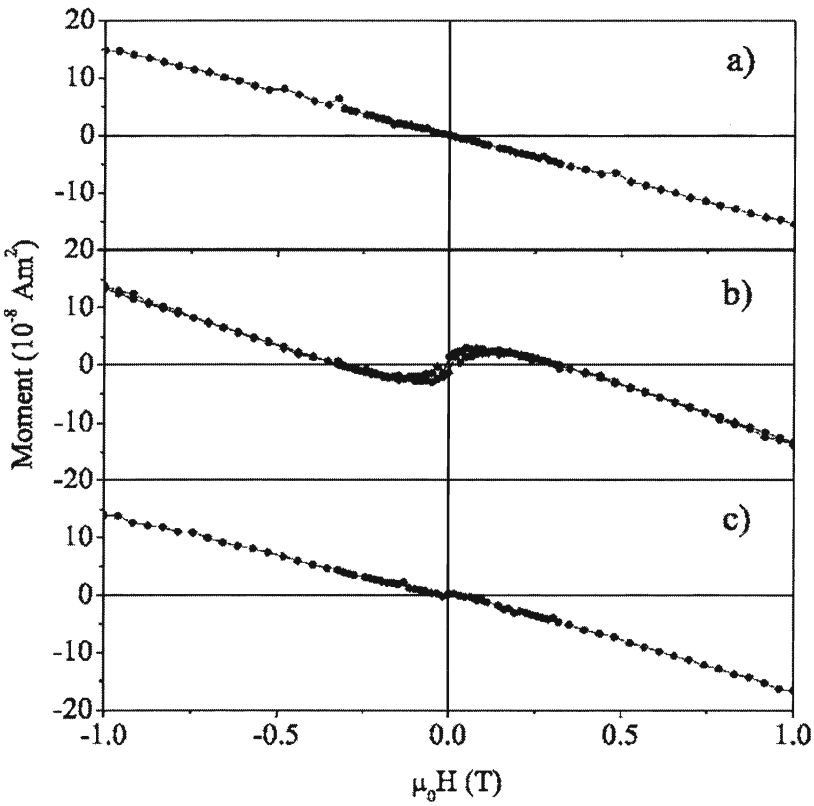

Figure 1.5: **Effect of reduction and oxidization on HfO_2. a) Powder as purchased, b) after reducing at 750°C, c) after oxidizing at 750°C. [12].**

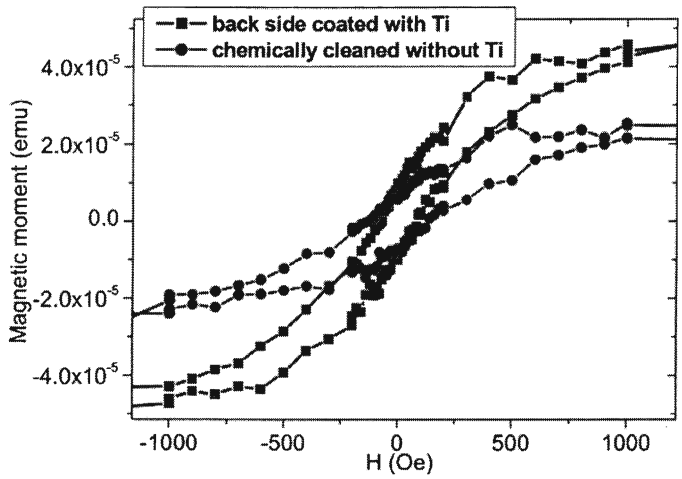

Figure 1.6: **Magnetization of Al_2O_3 with and without TiO_2 coating [18].**

Other semiconducting oxides have shown similar minute FM moments. Figure 1.6 shows a clean sample of Al_2O_3 measured before and after a coating of TiO_2. In both cases a hysteresis is seen without the addition of magnetic ions.

Ferromagnetism has also been observed in nanoparticles of normally nonmagnetic oxides [20]. Figure 1.7 shows magnetization measurements for nanoparticles of both zinc oxide and indium trioxide. Both oxides show room temperature FM after air annealing at 400°C (using a procedure similar to section 4.8) however this FM disappears when the annealing temperature is increased to 1200°C. As the annealing temperature increases the size of the nanoparticles also increases. This can be seen in figure 1.8 which shows field emission scanning electron microscopy pictures of an nanoparticle oxide after being annealed at varying temperatures. Also included in figure 1.8 is a magnetization measurement showing the removal of FM at high annealing temperature. It has been suggested that the origin of the ferromagnetism in these samples stems from unpaired electron spins which are created by oxygen vacancies [20], similar to the suggested origin of the ferromagnetism in the thin oxide films.

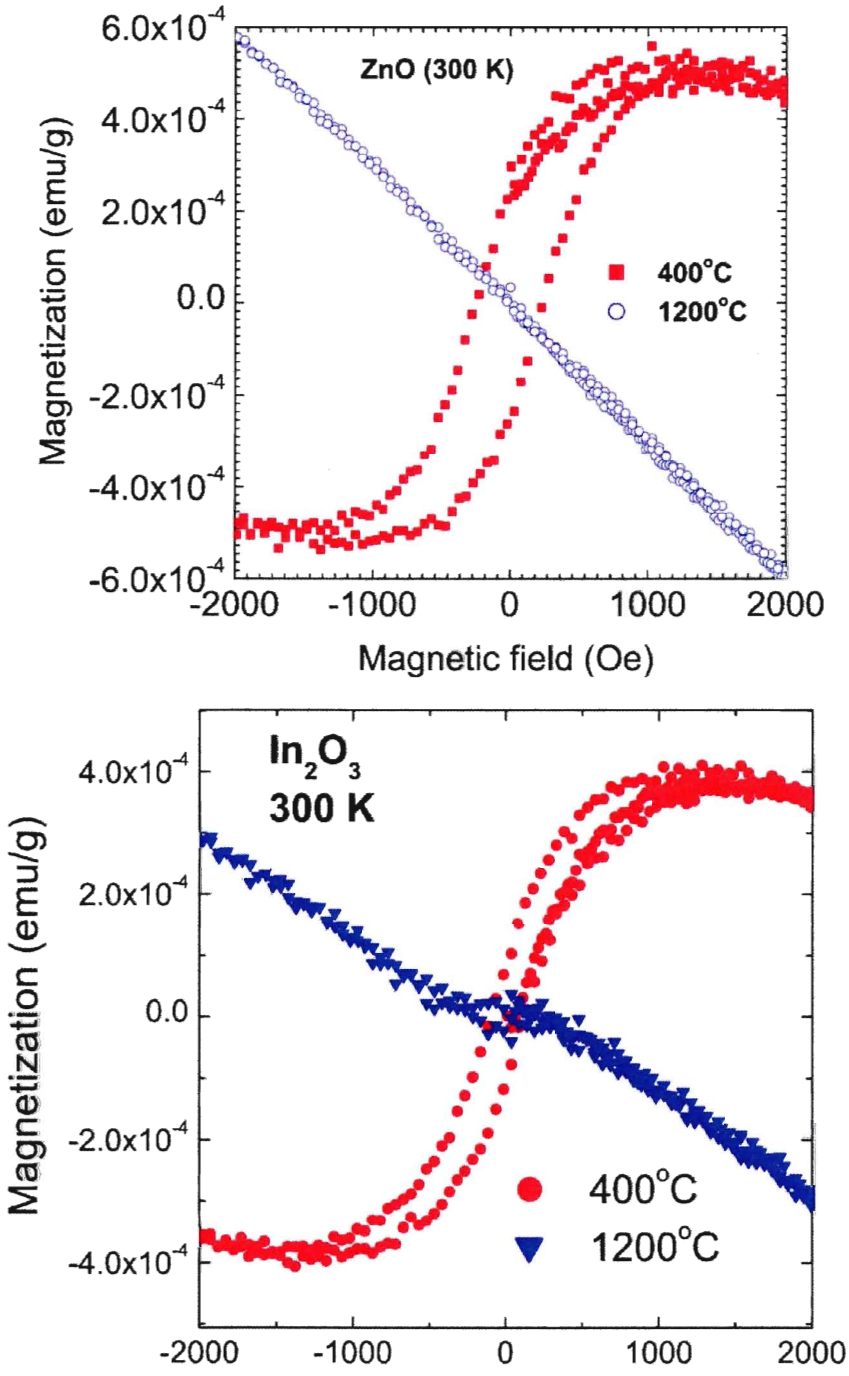

Figure 1.7: **Magnetization of ZnO and In_2O_3 nanoparticles [20].**

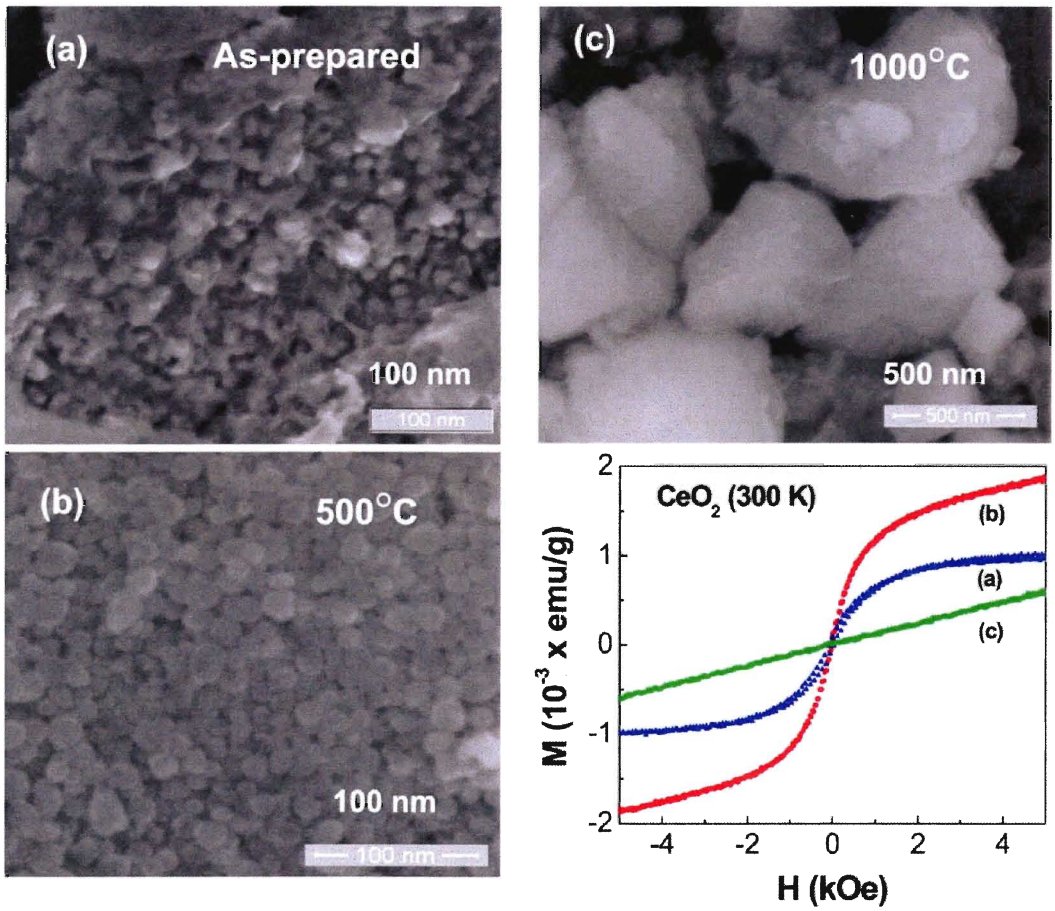

Figure 1.8: **Field emission scanning electron microscope pictures of CeO_2 nanoparticles and magnetization measurements at varying oxidization temperatures. Average particle size a)7nm, b)15nm, c)500nm [20].**

1.5 Ferromagnetism in $SrTiO_3$

A few years ago a ferromagnetic response was observed at Brock University in strontium titanate [21, 22]. Figure 1.9 shows two examples of hysteresis curves for $SrTiO_3$ substrates. This observation is of interest as strontium titanate has a closed electron shell configuration ($Sr^{2+}+Ti^{4+}+O_3^{2-}$), which should lead to a diamagnetic response. One possible explanation [12] attributes the FM to oxygen vacancies created by lattice imperfections and/or magnetic impurities present during the creation of the $SrTiO_3$ crystal. Other research has suggested that the FM is rooted in contamination of samples from handling with tweezers [19]. In order to prevent such contamination from occurring all handling of samples in this work was carried out with Teflon tweezers.

The surface of Strontium Titanate has been the subject of on-going studies and has attracted attention on its own. It has been found that the surface of Strontium Titanate restructures itself drastically when reduced or annealed [23]. This restructuring allows for the creation of non-perovskite phases (such as TiO, Ti_2O and SrO) near the surface as seen in figure 1.10. It has also been found that bubbles and dislocations are present in Strontium Titanate [24]. These bubbles and dislocations are concentrated near the cut surfaces of Strontium Titanate and their concentrations decay rapidly as a function of depth as seen in figure 1.11. It has also been observed that these dislocations act as diffusion paths within the crystal, allowing for rapid oxygen and impurity movement within the crystal [25].

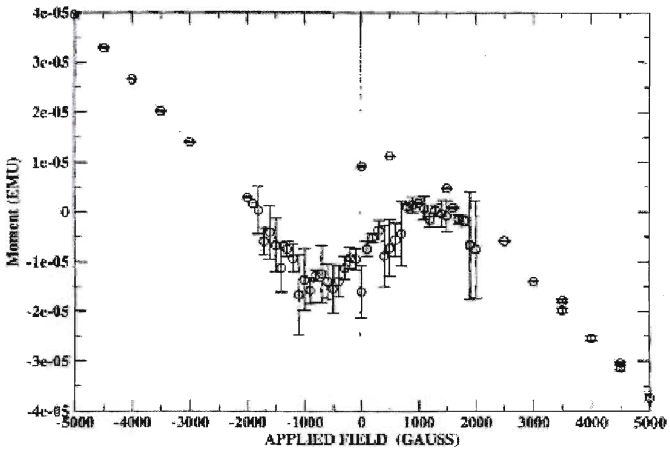

Figure 3.7: Magnetic moment vs. field at T=5K for $SrTiO_3$ sub-

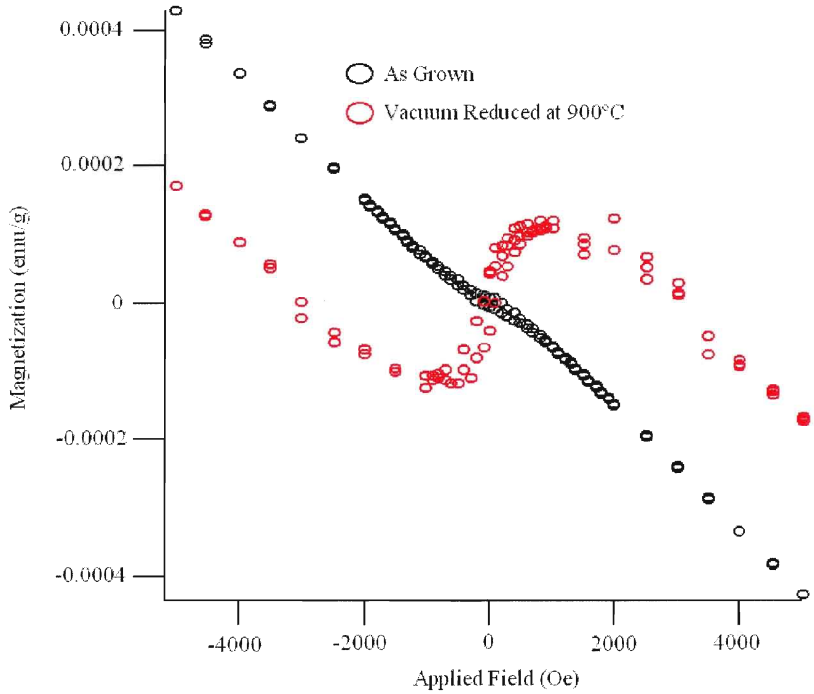

Figure 1.9: **Observed Ferromagnetism in $SrTiO_3$ form Brock University in 2004 [22] (Upper), and 2008 [21] (Lower).**

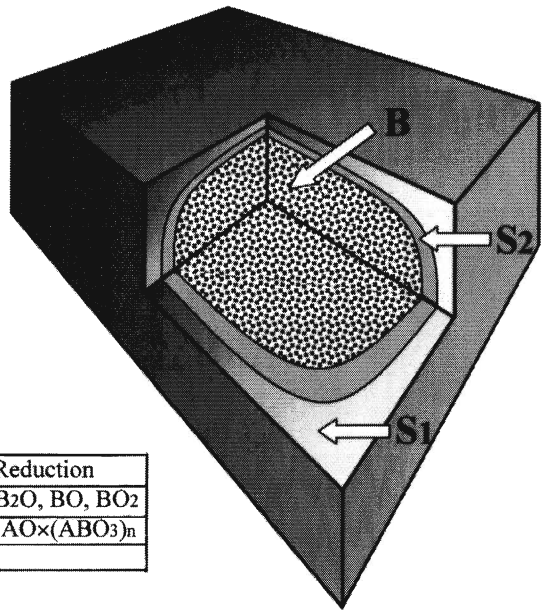

	Oxidation	Reduction
S1	$AO\times(ABO_3)_n$	B_2O, BO, BO_2
S2	B_mO_{2m-1}	$AO\times(ABO_3)_n$
B	ABO_3	

Figure 1.10: **Surface regions and phases of oxidized and reduced $SrTiO_3$ [23].**

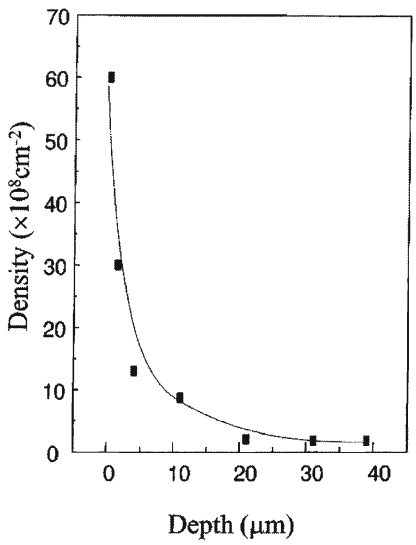

Figure 1.11: **Dislocation density as a function of depth from the cut surface [24].**

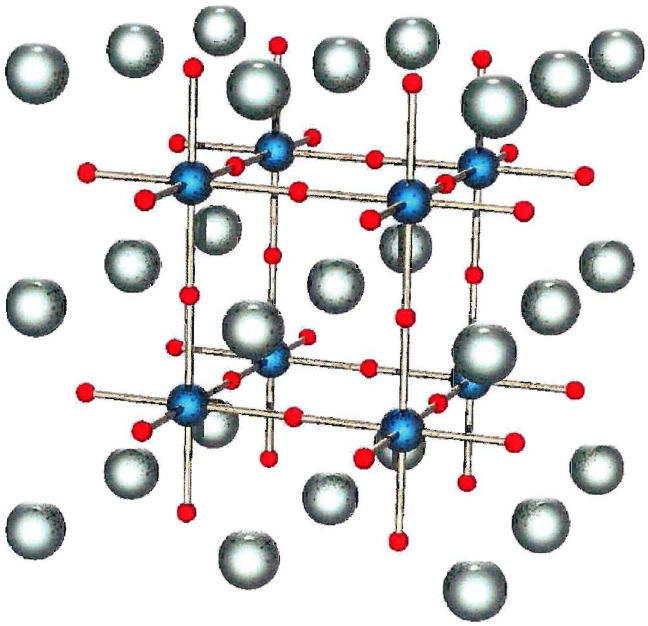

Figure 1.12: **Atomic view of Strontium Titanate with red representing oxygen atoms, blue representing titanium and green representing strontium. Picture courtesy of the Wikimedia commons.**

1.6 Strontium Titanate

1.6.1 Crystal Structure and Properties

Strontium titanate ($SrTiO_3$), also called Tausonite, is an ABO_3 type perovskite oxide. Oxides of this type all possess a simple cubic lattice structure with strontium titanate being no exception. Figure 1.12 shows an atomic view of strontium titanate's simple cubic structure with a lattice constant (a) of 3.9Å. At 105°K strontium titanate undergoes a transition from simple cubic to tetragonal however this transition is very minimal ($\frac{c}{a} \approx 1.0005$ [24]).

Pure (as grown or purchased) strontium titanate has been a topic of study for many years. These studies have shown that the surface of strontium titanate is a dynamic

system capable of many different topographies [23]. In addition to these topographies it has also been seen that the immediate surface region contains a dense collection of non-perovskite phases [23, 25, 26] as well as dislocations and bubbles [24, 25]. Work has been done to control these surface effects to reliably control their orientations to aid in the growth of thin films which use $SrTiO_3$ as a base [27]. Also, it has been suggested that the proper control of these surface effects could lead to a potential ferroelectric phase [23, 27].

Strontium titanate in its pure state acts as an insulator however, it becomes increasingly metallic when reduced [25, 28]. This transition from insulator to metal occurs as a result of the reduction removing oxygen from the $SrTiO_3$ crystal. This transition can be correlated to a change in the optical properties [25, 28, 29, 30].

1.6.2 Sample Growth and Initial Preparation

The single crystals purchased for this thesis were grown using the Verneuil method. The Verneuil method (or flame fusion method, as seen if figure 1.13) of single crystal production involves taking a high purity powder and liquefying it with an oxyhydrogen flame. This liquid falls through an oxygen environment until it comes to rest on a seed crystal mounted in a fireproof rod. This seed crystal is used to determine the orientation of the crystal being grown. As the crystal grows (through the falling liquid solidifying) it will adopt a boule shape as seen in figure 1.14. In order to keep the top of the growing boule at the optimal distance for the liquid material to solidify the fireproof rod is lowered as the crystal is grown. When the crystal boule is completely grown and allowed to cool it is then removed from the rod [31] and in the case of strontium titanate (as mentioned by all manufacturers of strontium titanate used in this work), annealed in an oxidizing atmosphere to return its clarity as when the boule is created it is in a reduced (dark) state. It is then cut, cleaned

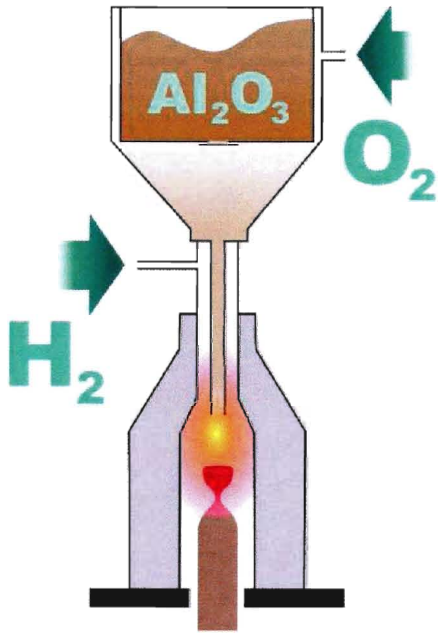

Figure 1.13: **Simplified Verneuil process diagram for Al_2O_3. Picture courtesy of the Wikimedia commons.**

Figure 1.14: **Verneuil grown Strontium Titanate boule [29].**

and polished to order. The downside to the Verneuil method of crystal growth is that the crystals produced are often filled with microscopic bubbles, dislocations and other defects. Further information on the Verneuil method for crystal growth can be found in reference [31]

Powders of strontium titanate can be formed by using an aqueous solution method. This method involves dissolving (supersaturating) a source of strontium ions (these can come from any strontium based water-soluble salt) into H_2O. Next, a source of titanium ions is added to the solution, these come from a titanium alkoxide which also doubles as the extra source of oxygen. While this mixture is cooling homogeneous nucleation occurs and a strontium titanate ($SrTiO_3$) precipitate (or powder) is formed. This powder is then extracted, dried and ready for use. There are many ways of producing $SrTiO_3$ powders, however the above steps provide a simplified example. An example of specific methods for powder production can be found in references [32] and [33].

1.7 The Plan for this Thesis

The goal for this thesis is to locate the source of the previously observed FM in $SrTiO_3$. Currently, the source of FM in oxides containing no magnetic ions is being vigorously debated, and this work will attempt to shed some light on this issue. As seen previously there are a variety of potential sources for this FM including tweezer contamination, oxygen vacancies and dislocations. To this end we will conduct several systematic oxidizations and reductions of both one and two face polished $SrTiO_3$ substrates from a variety of manufacturers. We will do this first to test if all as purchased $SrTiO_3$ single crystals are created equally. Secondly, to see if the FM is related to impurities and lastly to introduce oxygen vacancies in a controlled and systematic

fashion. As this thesis is primarily an investigation into the magnetic properties of $SrTiO_3$ it is first necessary to understand where the magnetic response comes from. Chapter 2 contains a brief overview of magnetism along with the magnetic analysis technique used extensively throughout this thesis. In order to ensure that all measurements are consistant, the above listed experiments were carried out following a rigid set of experimental procedures. These procedures along with brief descriptions of the various experimental techniques employed can be found in chapter 3. Chapter 4 presents all of the results that were obtained when utilizing the experimental techniques and analysis procedures as outlined in the previous chapters. The fifth and final chapter summarizes all of the findings from the experiments performed and draws conclusions from them. Locating the source of this FM is of importance as it has been shown that other oxides have also shown FM where it should not exist.

Chapter 2

Magnetism

2.1 Magnetic Theory

2.1.1 Origin of Magnetism

The origins of magnetism can be traced back to the components of the atom that have angular momentum; primarily the electrons because the spin magnetic moment is much larger than either the proton's or neutron's. The first and second possible origins of a magnetic moment would be from the intrinsic spin of the electrons and nucleons. The third possible origin for magnetism would be the orbital angular momentum of the electron around the nucleus. The individual contributions to the magnetic moment for the electron and nucleon differ and are dependent on mass as seen in equation 2.1 (with $\hbar$ being Planck's constant over 2π, e is electron charge and m is the rest mass) which shows a simplified calculation for the orbital magnetic moment based on the Bohr model of the hydrogen atom. The moment of the nucleus is much smaller than that of the electron and is thus ignored.

$$\mu = \frac{e\hbar}{2m} \tag{2.1}$$

Depending on the number of electrons present in the atom different types of magnetism can be observed, as how the electrons interact with one another along with what orbitals they are in will determine what type of magnetism is present. As well, the interactions between moments of neighboring atoms (short range interactions) or

interactions between moments of distant atoms (long range interactions) can determine the type of magnetism present. The resultant magnetization (magnetic moment per unit volume) of a material is a sum of all of the different types of magnetism within the material, as seen in

$$\vec{M}_{total} = \vec{M}_{paramagnetic} + \vec{M}_{ferromagnetic} + \vec{M}_{diamagnetic} + \cdots \tag{2.2}$$

equation 2.2. It should also be noted that there exist several different types of each of the above listed types of magnetism and only a select few of which are discussed in this thesis. Further information on magnetism and magnetic theory as mentioned in section 2.1 can be found in references [34] and [35].

2.1.2 Diamagnetism

Diamagnetism is the most common form of magnetism. If one assumes that electron orbits are essentially current loops then when an external field is applied a change in magnetic moment will be generated which opposes the external field. Thus diamagnetism takes the form of a negative susceptibility ($\vec{M} = (-\chi_{diamagnetic})(\vec{B})$) which is a measure of how diamagnetic a material is, an example can be seen in figure 2.1. A diamagnetic substance is composed of atoms with no net magnetic moment as the electrons exist in completely filled shells. These atoms could be alone (noble atoms), polyatomic gases (as the process of creating such a gas usually results in the filling of electron shells through electron sharing) or more complex substances (such as $SrTiO_3$, as mentioned in section 1.6.1).

2.1.3 Paramagnetism

Conduction Band (Pauli) Paramagnetism

Conduction band (or Pauli) paramagnetism originates from the spins of the electrons in the conduction band. As the conduction electrons behave as a free electron gas, an equal number of electrons are in the spin up and spin down states, creating no net magnetic moment. When an external magnetic field is applied the electrons begin to favor the lower energy spin direction (where E = -$\vec{\mu} \cdot \vec{B}$) whose intrinsic moment is aligned to the applied field, creating a net magnetic moment. However, the majority of the electrons in this free electron gas are unable to align themselves with the applied field as their corresponding orbital with the opposite spin is already occupied. Thus only the electrons within a range of $k_B T$ at the top of the Fermi distribution have the possibility of flipping their spins to align with the applied field. In the limit of $k_B T \ll \epsilon_F$, the Pauli susceptibility takes the form of a positive value independent of temperature, approximated to equation 2.3 where N is the number of atoms per unit volume, μ is the effective magnetic moment per electron and ϵ_F is the Fermi energy.

$$\chi_{Pauli} = \frac{3N\mu^2}{2\epsilon_F} \tag{2.3}$$

Local Moment (Curie) Paramagnetism

Local moment paramagnetism originates from the bound electrons which reside in the incomplete inner electron shells. As these orbitals are not completely filled the orbital and spin moments of these electrons do not cancel out. Giving rise to a net magnetic moment on the atom. These moments are generally oriented in random directions due to thermal agitation. In the presence of an external field these magnetic moments will align with the field and generate a net magnetic moment from the sample. This magnetic moment takes the form of a positive, linear susceptibility (χ_c) with respect

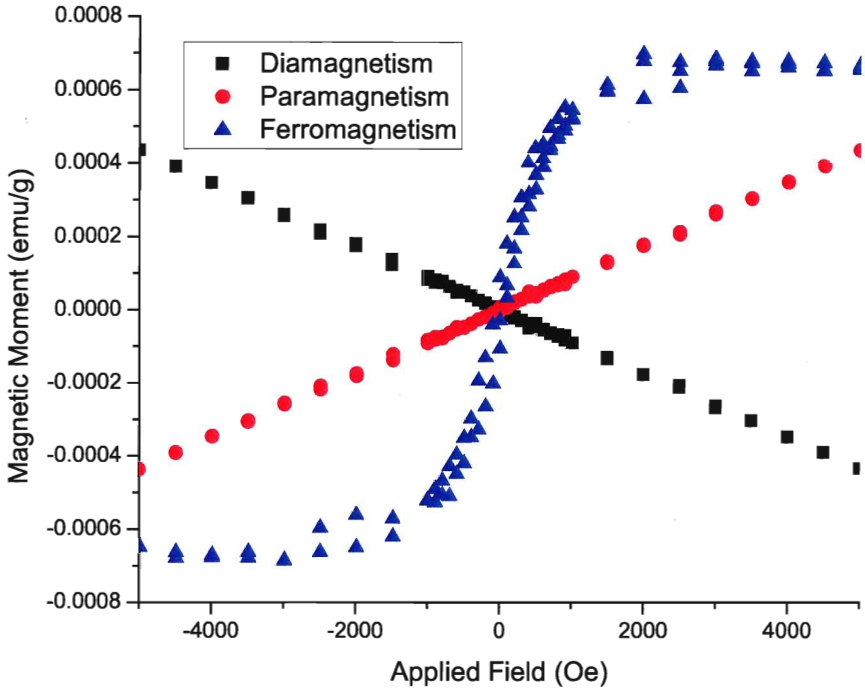

Figure 2.1: **Examples of magnetic responses for paramagnetism, diamagnetism and ferromagnetism in the presence of an external field.**

to applied field ($\vec{H}$), as seen in equation 2.4 where T is temperature and C is the Curie constant per unit gram. An example of a paramagnetic material can be seen in figure 2.1.

$$\chi_c = \frac{C}{T} \tag{2.4}$$

2.1.4 Ferromagnetism

Ferromagnetism can either originate from the same place as local moment paramagnetism or it can originate from the conduction band electrons (itinerant ferromagnetism). What makes ferromagnetism different is that in ferromagnetic materials the magnetic moments from neighbouring atoms group together and all point in the same

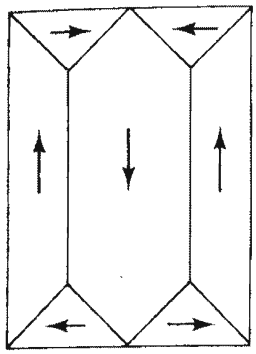

Figure 2.2: **Sample domain layout with arrows indicating direction of internal magnetic moment [34].**

direction even when the applied field is zero. This grouping of atoms with similarly directed moments is called a domain. These domains spontaneously form as, for a ferromagnetic material they represent a lower energy configuration. A ferromagnetic material will consist of a large number of domains with moments in various directions as seen in figure 2.2. When the ferromagnetic material is subject to an external field these domains will shift and change. Domains whose moment is aligned with the applied field will grow in size while other domains will shrink in size. This resizing of domains will continue until a saturation magnetization has been reached, which occurs when the domains can no longer grow any more as effectively the entire sample is now one large domain oriented in the direction of the applied field. What makes a ferromagnet special is that when the external field is removed the changes it made to the domain structure of the sample may partially remain. In short, $\vec{M} \neq 0$ when $\vec{H} = 0$. This will allow a previously non-magnetized sample to become magnetized after it has been exposed to an external field. As a result when a magnetized sample is subject to an external field in the opposite direction to its magnetization the sample will resist the change with a certain amount of remnant magnetization. All of these effects can be seen in figure 2.3 which shows the characteristic ferromag-

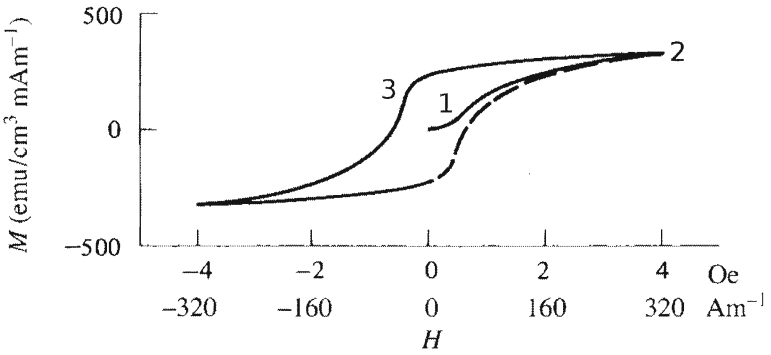

Figure 2.3: **Sample hysteresis curve with labeled features. 1) Initial curve, 2) Saturation magnetization, 3) Remnant magnetization [34].**

netic hysteresis curve created by measuring the moment of a sample in an applied field, an example can be also be seen in figure 2.1. Should the temperature of the ferromagnetic material be increased to its Curie temperature the domain walls will cease to exist as thermal agitation will randomly orient the magnetic moments of the individual atoms. Thus, the ferromagnet will lose its spontaneous magnetization and develop a linear dependance where $\vec{M} = \vec{H} \cdot \chi_{cw}$. Where χ_{cw} can be calculated using equation 2.5 where T is temperature, C is the Curie constant per unit gram and θ is the Weiss constant.

$$\chi_{cw} = \frac{C}{T - \theta} \tag{2.5}$$

2.2 Magnetic Analysis Technique

Strontium titanate (as described in section 1.6.1) possesses a completely closed shell electron structure. Combining this with section 2.1 suggests that $SrTiO_3$ should have a solely diamagnetic response. For the purpose of this thesis the bulk of the measurements performed on the $SrTiO_3$ substrates measured the magnetic moment or

magnetization when normalized by sample volume or mass ($\vec{M}_{total}$) as it varied with applied field ($\vec{H}$). As magnetic components are strictly additive the total magnetization of the sample can be broken down to a linear component (primarily diamagnetic in this case, however reduced samples will have a Pauli paramagnetic component) and a ferromagnetic component as seen in equation 2.6. The application of this equation is demonstrated in figure 2.4 in which an example of data has its ferromagnetic saturation magnetization (M_{sat}) extracted from the total magnetic moment. The upper graph shows some sample data with a pair of linear fits. These linear fits (using the least squares method) are done to the tails of the graphed data where the magnetization appears more or less linear with respect to applied field. The average of the slope of these two linear fits was taken to be the diamagnetic susceptibility ($\chi_{diamagnetic}$). As we know the applied field ($\vec{H}$) and the total magnetization ($\vec{M}_{total}$) we can then use equation 2.6 to calculate the ferromagnetic contribution which can then be plotted on its own. This plot (the lower part of figure 2.4) will show the ferromagnetic contribution including the saturation magnetization, initial curve, remnant magnetization and any hysteresis. This method of removing the diamagnetic contribution (through the diamagnetic susceptibility) from the total signal is used extensively throughout this thesis.

$$\vec{M}_{total} = \vec{M}_{linear} + \vec{M}_{ferromagnetic} = (\vec{H})(\chi_{diamagnetic}) + (\vec{H})(\chi_{Pauli}) + \vec{M}_{ferromagnetic} \tag{2.6}$$

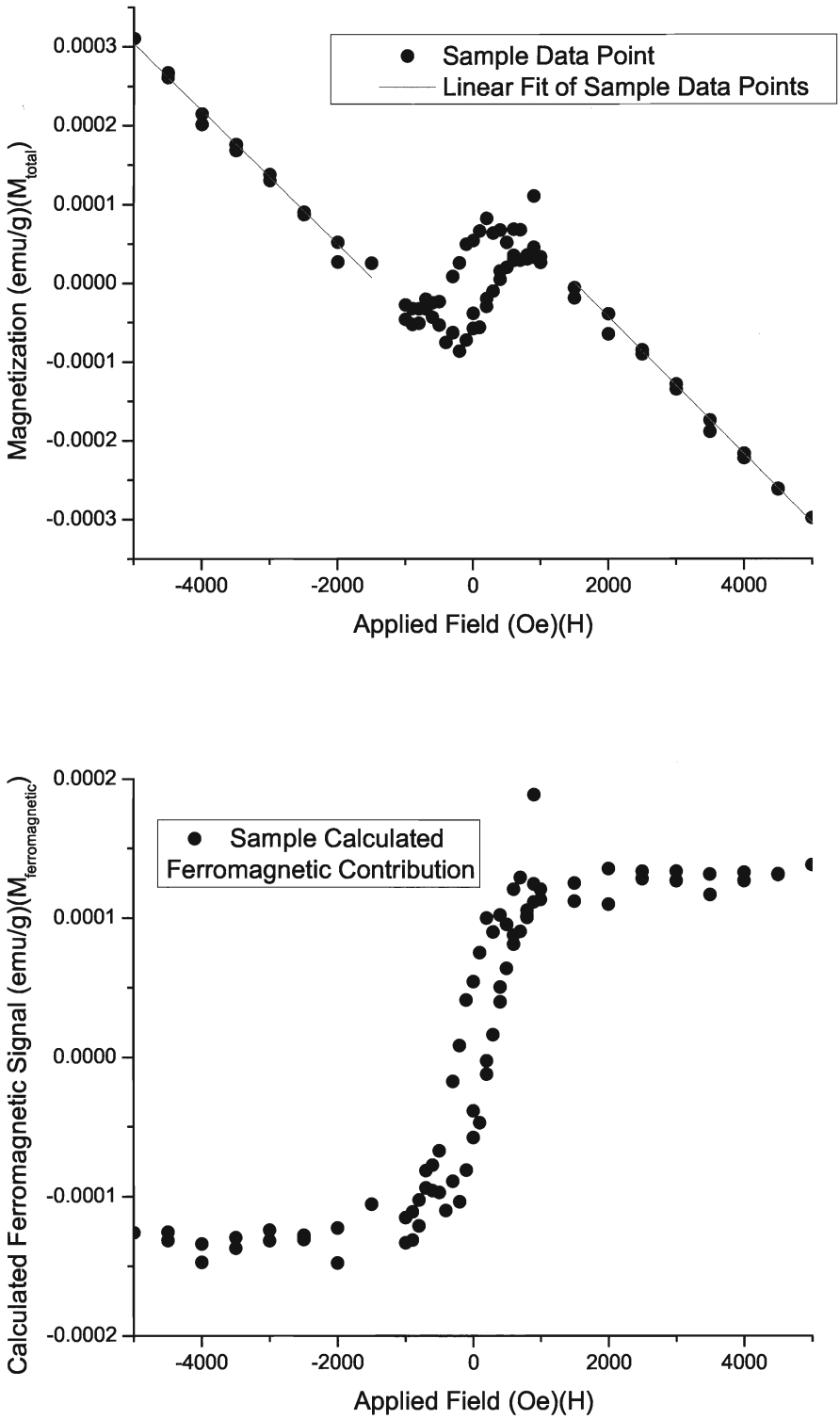

Figure 2.4: **Location of diamagnetic region linear fits (upper). Example of extracted ferromagnetic contribution (lower).**

Chapter 3

Methods

3.1 Magnetometry

As the bulk of the research for this thesis involved measuring the magnetic properties of various $SrTiO_3$ samples, the use of a highly sensitive magnetometer was essential. All magnetic moments were measured using a Quantum Design Magnetic Property Measuring System (MPMS). The MPMS utilizes a direct current superconducting quantum interference device (or a DC SQUID) to measure the magnetic moment of a sample under various conditions. All measurements were done at 295°K with a varying external field provided by a superconducting magnet. All samples were mounted for the SQUID magnetometer using separate plastic mounting straws to prevent cross sample contamination.

The DC SQUID magnetometer utilized operates by pulling the mounted sample through a superconducting, second order gradiometer as seen in figure 3.1. Surrounding the second order gradiometer is the superconducting magnet which is used to apply an external field. When the sample is then pulled through the windings in the gradiometer the magnetic properties of the sample will induce a current in the wire. This current then travels through the superconducting wire to where it is inductively coupled through the center of a superconducting ring containing two Josephson junctions connected in parallel. A Josephson junction consists of two superconducting layers separated by a very thin insulating layer. This allows superconducting elec-

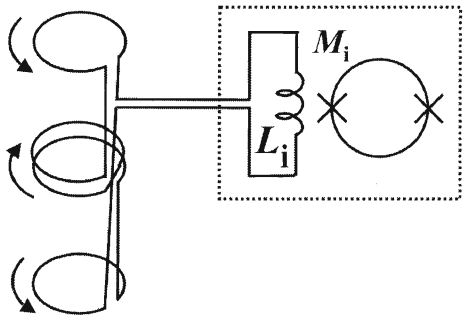

Figure 3.1: **A superconducting flux transformer consisting of a second order gradiometer connected inductively (L_i) to a superconducting ring (M_i) containing two Josephson junctions (X). The dotted box indicates a magnetically shielded component [36].**

trons to tunnel through the insulating layer, with a certain probability. The current generated by the sample then adds to the existing current in the ring. When the current in the ring exceeds a critical value [36] the ring becomes resistive, allowing for a voltage to be measured across it. For the DC SQUID to be operational this current must be kept above the critical value to keep the ring resistive. This allows for a direct relation between the measured voltage across the ring and the magnetic moment of the sample being measured. Care must be taken at all times to ensure proper calibration of the SQUID, so that the same amount of magnetic flux always generates the same change in voltage. Before all experiments the SQUID was calibrated using a platinum reference sample. More information on SQUID magnetometry can be found in reference [36].

3.2 X-ray Diffraction

X-ray diffraction (or XRD) was used as it is a versatile experimental technique that uses X-rays to determine structural properties of materials. It was used to attempt to

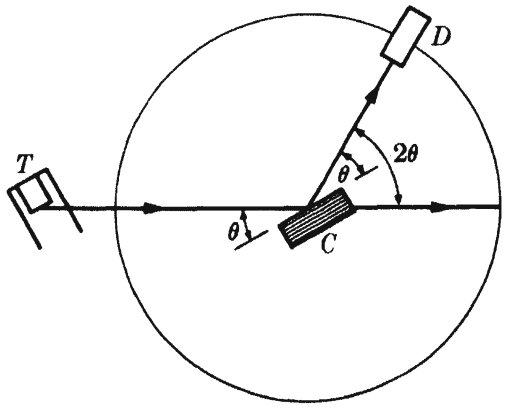

Figure 3.2: **X-ray diffraction experimental setup with T (X-ray source), D (detector) and C (sample) [37].**

identify any impurity phases that might have existed on the surfaces of the samples. Also, X-ray diffraction was used to determine how reduction affects the structural properties of both single crystals and pressed pellets. X-rays are used due to their small wavelengths, which are on the order of angstroms (Å). Characteristic X-rays, which are almost monochromatic having a very narrow line width were used to measure spectra. The operation of the experiment is quite simple; monochromatic X-rays are incident on the sample and are scattered off as seen in figure 3.2. The detector then moves in a semicircle around the sample counting the number of X-ray photons scattered at the various angles. As a result XRD data provides a measure of X-ray reflection counts versus deflection angle (2θ). Figure 3.3 shows two X-rays incident on a crystal in the (100) direction. With the distance between the adjacent lattice planes (d) working out the path difference can be seen in equation 3.1.

$$\text{Path Difference} = \overline{AB} + \overline{BC} = dsin\theta + dsin\theta = 2dsin\theta \tag{3.1}$$

If figure 3.3 is expanded to include more lattice points and reflected X-rays it will be seen that some of the reflected X-rays will overlap with one another. These overlap-

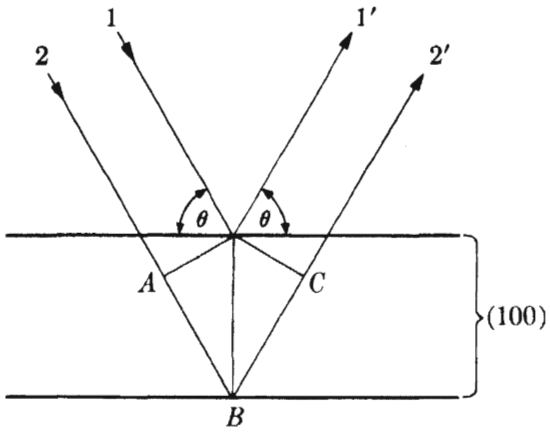

Figure 3.3: **X-ray reflection off of a crystal lattice in the (100) plane [37].**

ping reflected X-rays will produce a diffraction maximum when the path difference is equal to an integer number of wavelengths (from constructive interference) and minima at all other points (from destructive interference). This condition is called Bragg's law which can be seen in equation 3.2.

$$\lambda = 2dsin\theta \tag{3.2}$$

X-ray diffraction thus allows one to determine a set of plane spacings that are characteristic of a particular crystal structure. It can then also be used to detect the presence of impurity phases. As the Bragg maximum is determined by (d), the distance between lattice planes, it can be seen that each Bragg maximum is associated with a particular reciprocal lattice vector $\vec{G}$ where $|\vec{G}| = \frac{2\pi}{d}$. The value for $\vec{G}$ for a simple cubic lattice can be seen in equation 3.3 which leads to equation 3.4.

$$|\vec{G}| = \frac{2\pi}{a}(h\hat{x} + k\hat{y} + l\hat{z}) \tag{3.3}$$

As $SrTiO_3$ has a cubic crystal structure (as mentioned in section 1.6.1) the lattice plane spacing (d) can be related to the Miller indices (h, k, and l), lattice parameter

(a), expressed as equation 3.4.

$$\frac{1}{d^2} = \frac{(h^2 + k^2 + l^2)}{a^2} \tag{3.4}$$

When equation 3.4 is combined with Bragg's law, equation 3.2, through equating them through the lattice plane spacing (d) equation 3.5 is obtained, which directly relates the θ measured through X-ray

$$sin^2\theta = \frac{\lambda^2}{4a^2}(h^2 + k^2 + l^2) \tag{3.5}$$

diffraction with the individual lattice parameters. As λ, h, k, and l are known and θ can be measured equation 3.5 allows us to calculate the lattice parameter. Information is also contained in the diffraction peak line width which is determined by three factors: (1) particle size or coherent domain size, (2) disorder, stress or strain and (3) instrumental line width [37]. A change in these factors will cause the width of the diffraction line to change.

The Williamson-Hall equation [37], as seen in equation 3.6, can be used to separate the contributions from the crystallite size and from the stress/strain on the crystal. In this equation β represents the integral breath, θ represents an angle (either measured from the diffractometer or the diffractometer's line width), λ is the wavelength of light used, D is the volume weighted crystallite size and ϵ is a measure of the strain on the crystal.

$$\beta = \triangle\theta_{measured} - \triangle\theta_{instrument} = \frac{\lambda}{Dcos\theta} + 4\epsilon tan\theta \tag{3.6}$$

In this work we will use both single crystals and powder samples which will react differently when analyzed with the Williamson-Hall equation. To analyze x-ray diffraction data with equation 3.6 one would first calculate the integral breath (β) in radians. This integral breath can be incorporated into the Williamson-Hall equation

to create equation 3.7 [38] where θ now represents the angle of the diffraction peak. A plot of $\frac{\beta cos\theta}{\lambda}$ vs $\frac{4sin\theta}{\lambda}$ can then be created using the x-ray data from each peak and analyzed to extract the separate crystallite size contribution and strain contribution. In the above listed plot the y-intercept will correspond to the crystallite size (D) while the slope of the line will correspond to the stress term (ϵ).

$$\frac{\beta cos\theta}{\lambda} = \frac{1}{D} + \frac{4\epsilon sin\theta}{\lambda} \tag{3.7}$$

A simplified equation for the approximation of the crystallite size can be seen in equation 3.8, also called the Scherrer equation. The Scherrer formula relates the crystallite size (t) to the wavelength of the X-rays (λ) divided by the full width half maximum (B) multiplied by the cosine of the angle (θ) at the maximum point of the peak. Further information on the Williamson-Hall and Scherrer formula as well as X-ray diffraction in general can be found in references [37, 38].

$$t = \frac{\lambda}{Bcos\theta} \tag{3.8}$$

3.3 Energy-Dispersive X-ray Spectroscopy

Energy-dispersive X-ray spectroscopy (EDX) is an experimental technique used to identify which elements are present in a given sample. This experimental technique was used as a primary test to identify what elements were present on the surface of the samples. EDX uses an electron beam (with energies of keV) directed at a sample. These charged electrons will undergo collisions with the electrons bound to the atoms in the sample. These collisions will cause the bound electron to be ejected, leaving a hole in the energy levels of the atom. This hole will then be filled by a higher energy electron from the same atom, expelling energy in the process

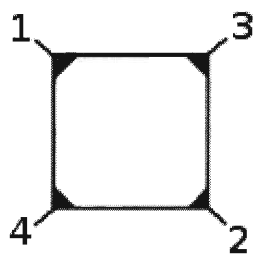

Figure 3.4: **Van der Pauw contact setup and numbering.**

in the form of an x-ray. These emitted x-rays can then be collected and used to determine what elements are present. This is possible as the energy of the emitted x-rays is directly related to the transition the electrons go through after filling the space created from an electron getting ejected by a collision from the electron beam. As these transitions are characteristic of each element the emitted x-ray energies can be used for element identification. More in depth and further information on EDX can be found in reference [39].

3.4 Van der Pauw Resistivity

All resistivity measurements performed for this thesis were done using the van der Pauw method. This method for measuring resistivity was selected as it provides an accurate measurement for square samples of uniform thickness. In order to perform the measurement four contacts must be made with the sample, these contacts should be placed as close to the corners of the samples as possible as seen in figure 3.4. To make a resistivity measurement one must first measure the resistance of the sample by applying a current through two adjacent points (such as 2 and 3) while the voltage

is measured across the two unused contacts (1 and 4 in this case). The resistance can then be labeled and calculated through equation 3.9. A second such resistance

$$R_{14,23} = \frac{|V_{14}|}{I_{23}} \tag{3.9}$$

is measured and using equation 3.10 the resistivity of the sample can be

$$\rho = \frac{\pi d(R_{14,23} + R_{24,13})f}{2ln(2)} \tag{3.10}$$

measured [40]. In equation 3.10, (d) represents the thickness of the sample and (f) is related to a ratio expressed by equation 3.11 and is

$$f\,\alpha\,\frac{R_{14,23}}{R_{24,13}} \tag{3.11}$$

exactly equal to 1 when the ratio is equal to 1. As the ratio increases the value for f decreases which means that there is a large differences between the two resistances measured. This would suggest that either the contacts with the sample are bad or that the sample is inhomogeneously doped [40]. Further information on the van der Pauw method for measuring resistivity can be found in reference [40].

3.5 Optical Transmission Experiments

Optical transmission measurements were conducted on the $SrTiO_3$ substrates in an effort to correlate particular optical features with the ferromagnetic moment. Optical measurements were conducted on a broad spectrum of wavelengths ranging from the ultraviolet (190nm) to infrared (2500nm). To cover this range several optical measurement devices were invoked which used a variety of optical techniques discussed in this section. The basic experiment involves measuring a background spectrum (I_b) without the sample being present and subsequently placing the sample in the optical

path to remeasure the spectrum (I_s). The optical transmission can then be calculated via equation 3.12.

$$Transmission = \frac{I_s}{I_b} \tag{3.12}$$

3.5.1 Optical Monochromator

An optical monochromator is a device which outputs monochromatic (single wavelength) light. The monochromator operates by first taking a broadband (multiple wavelengths) source and through either optical dispersion or diffraction it will separate out the wavelengths until only a single selected wavelength remains. For this to be possible first the light from the broadband source must be collimated by a reflecting mirror. This collimated light then travels to a prism or a diffraction grating to be separated out into individual components. The individual component is then selected by a final focusing mirror which is set to focus on a narrow exit slit where the now monochromatic light can be used for experimentation.

3.5.2 Fourier Transform Infrared Spectroscopy

Fourier transform infrared spectroscopy (or FTIR) as the name suggests involves applying a Fourier transform to a spectrum of infrared wavelengths. Unlike the optical monochromator that was mentioned in section 3.5 the FTIR utilizes an interferometer; most commonly this is a Michelson interferometer. A Michelson interferometer operates by first directing a beam of monochromatic collimated light into a beam splitter. One of these beams is directed to a stationary mirror which then reflects it back into the beam splitter; the other beam is reflected off of a linearly movable mirror and is once again directed back into the beam splitter. The two separate beams are joined again and are finally directed into the detector. When the movable

mirror is exactly the same distance away from the beam splitter as the fixed mirror, total constructive interference occurs when the two separate beams are rejoined in the beam splitter. This initial setup where the path difference between the two light beams is zero is called the zero path difference. As one of the mirrors is moved a difference in the distance the light has to travel is created. When this distance (d) is an integer number (n) of wavelengths (λ) then total constructive interference is observed. This can be seen in equation

$$d = n\lambda \tag{3.13}$$

3.13, with the zero path difference corresponding to n = 0. As would stand to reason total destructive interference would occur when the path difference is equal to a

$$d = (n + \frac{1}{2})\lambda \tag{3.14}$$

half integer value, as seen in equation 3.14. This shifting between total constructive and total destructive interference is the core process and what gives the interferometer its name, as it is a device that measures interference patterns.

Where the FTIR differs from a standard Michelson interferometer is that the light source is not monochromatic, but a range of infrared wavelengths. Also seen in figure 3.5 is the location of the sample to be examined. One can either measure the transmittance of the sample using the given setup or the setup can be modified slightly to measure the reflectance of the sample. As many wavelengths of light are being used the interference pattern for any integer above zero becomes very complex requiring the use of a Fourier transform to separate out the individual wavelengths. In the case of the FTIR the zero path difference creates a large amount of total constructive interference which quickly diminishes as the distance the mirror is moved increases. From this central feature (centerburst), shown in the left portion of figure 3.6, a Fourier transform can be applied to extract the individual wavelengths, shown

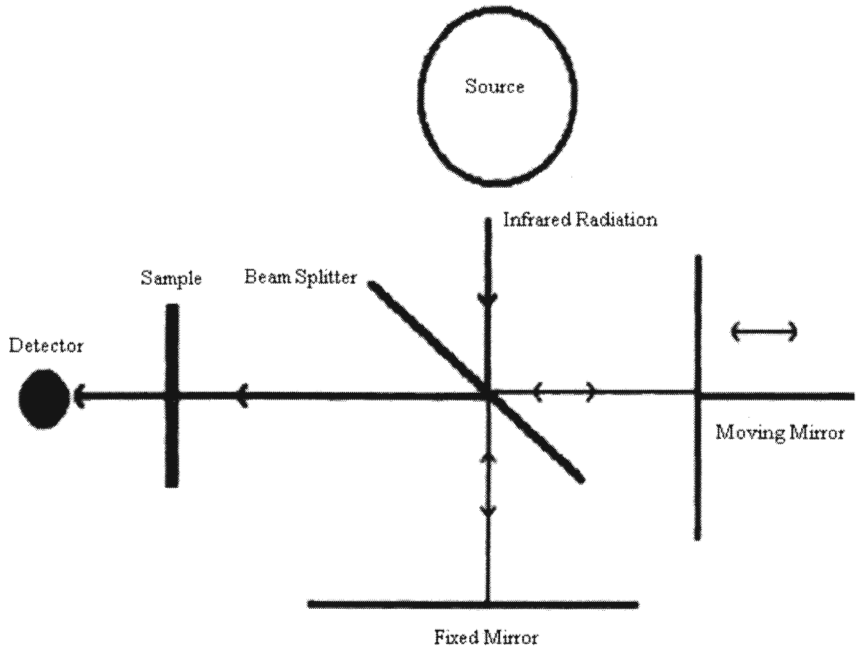

Figure 3.5: **Optical diagram of the Fourier transform infrared spectrometer [41].**

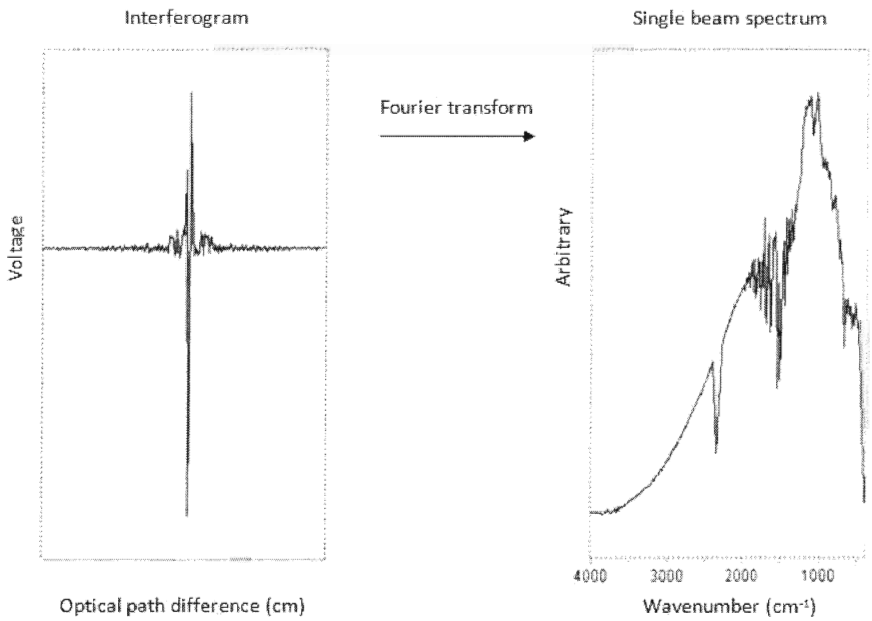

Figure 3.6: **Decomposition of centerburst (left) to individual wavenumbers (right) [41].**

in the right portion. It should be noted that the Fourier integral uses an infinite optical path length which is not physically possible, so the integral is truncated to an appropriate range which is limited by how far the mirror can move. Figure 3.6 also shows that the spectrum fluctuates as a function of wavenumber or wavelength. As a result a background scan is needed to compare the measured result against. It should also be noted that FTIR is sensitive to atmospheric gasses, which even under vacuum can be present in minute amounts potentially leading to false peaks. Further information and detail on Fourier transform infrared spectroscopy can be found in reference number [41].

3.6 Sample Reduction and Oxidation

3.6.1 Reduction

Samples were reduced by heating them in a controllable high temperature tube furnace under vacuum ($\sim 5\times10^{-5}$ Torr). The sample to be reduced was placed in an Al_2O_3 boat. This boat was inserted into a quartz tube which was mounted in the furnace. The quartz tube was closed at one end and had a vacuum line attached to the other. The boat was then pushed so that the sample rested in the center of the oven. A thermocouple (K-type) was then inserted under the quartz tube so that the tip of the thermocouple would rest just below the sample. The oven would then be closed and sealed with quartz fiber placed around the openings to allow for higher internal temperatures. Once a sufficient level of vacuum was reached ($\sim 10^{-5}$ Torr) the controller connected to the thermocouple was activated. The oven was then driven up to a set temperature as quickly as possible. The controller would then be used to maintain the oven at this set temperature. When it came time to cool the oven down, the controller was turned off and the oven was allowed to cool down without external

assistance. This rapid quenching was desired to lock in any features that had been changed as a result of the reduction. Only when the oven had completely cooled was the vacuum removed. This was done to prevent oxygen and other contaminants from seeping back into the heated crystal.

3.6.2 Air Annealing (Oxidation)

Some samples were annealed in air rather than in vacuum. The only difference between the two procedures is that the Al_2O_3 boat containing the $SrTiO_3$ substrate was placed in a quartz tube which was left open at both ends. As with the reduction process the oven is brought up to temperature and subsequently cooled as rapidly as possible to maintain the characteristics acquired through the air annealing.

3.7 Pellet Pressing

Throughout the course of this thesis many pellets of $SrTiO_3$ were pressed from a powder. A pellet pressing die was used to press the pellets into a cylindrical shape (5mm diameter with varying height) while a hydraulic press was used to apply the force required to make the pellet. The die was constructed out of supposedly non-magnetic materials (an aluminum plunger and a plastic cylinder) to keep magnetic contamination to an absolute minimum. Unfortunatly, it was later found that both the plastic and aluminum used were ferromagnetic. Through trial and error it was found that the minimum pressure the pellets needed to be pressed at was 1.4×10^7Pa. This pressure was required in order for the pellets to have sufficient structural integrity to withstand handling with Teflon tweezers, being jolted while undergoing SQUID measurement and remaining in one piece during reduction under vacuum.

3.8 Sample Polishing

$SrTiO_3$ substrates were polished using a manual (hand) polishing setup consisting of a weighted plug and a holder for said plug. The sample was mounted to the bottom of the plug (which resembles a cork) with the surface to be polished facing out. The sample was affixed with an acetone soluble adhesive to allow for easy cleaning. Rough polishing was done using either six or eight hundred grit emorypaper. The emorypaper was well lubricated with kerosene with more being applied throughout the rough polishing process to keep the system well lubricated. The holder (a cylinder with a hole in the center for the plug) was placed on the emorypaper and the plug was inserted and allowed to fall into place under the force of gravity. It is important to note that no external force should be applied to the top of the plug as the weight of the plug alone exerts enough force to allow the sample to come into contact with the polishing surface, further force could damage the sample and polishing surface. The holder was then moved in a figure eight pattern with a relatively slow but consistent speed. This process was kept up until all large scratches on the surface of the crystal were removed; a microscope was also used in this step to aid in searching for surface scratches. Upon completion of the rough polishing both the holder and plug (with sample attached) were cleaned in an ultrasonic cleaner in a distilled water bath. The goal of this cleaning is to remove all of the debris from the polishing equipment. It is important to remove all of this debris as this debris will contaminate the fine and ultrafine polishing pads and will lead to surface scratching of the final sample. After cleaning is complete and the plug and holder should be dried and the adhesive on the sample should be checked for damage from the ultrasonic cleaning and reapplied if necessary. This same figure eight process is then repeated with a polishing pad using a six micron diamond paste as an abrasive. The lubricant was changed from kerosene

to MetaDi Fluid (manufactured by Buehler) which is a lubricant designed for use with a diamond based compound. After a second thorough cleaning and inspection the process was repeated a third time with a new polishing pad and a one micron diamond compound. The sample was then polished in the figure eight pattern and observed under a microscope until an acceptable amount of defects are seen. With the one micron diamond paste as an abrasive the crystal will obtain a mirrored finish which shows any flaws in polishing that were previously camouflaged. If a large amount of flaws are seen then the whole polishing process must be repeated. For this thesis all of these hand polished surfaces of single $SrTiO_3$ crystals had a limited amount of these defects (six micron scratches).

Chapter 4

Results

4.1 Overview

In September 2008 we started SQUID work with $SrTiO_3$ (STO) substrates purchased from three manufacturers: CrysTec (CRS), MTI Corporation (MTI) and Semiconductor Wafer, Inc. (SWI). All of the substrates were (100) oriented having been grown using the Verneuil method and prepared as described in section 1.6.2. Samples were mounted such that the plane of the substrate was parallel to the generated magnetic field of the SQUID (as mentioned in section 3.1), using clear plastic mounting straws. The straws had been previously measured and had been found to have no moment, making them ideal for sample mounting. All SQUID measurements were done at 295°K (unless otherwise stated) to avoid contamination. This contamination stems from oxygen (or other contaminants) freezing on the straw and/or sample. As the ferromagnetic moment of STO is very small and already pushing the limits of what the SQUID can measure the contribution from contaminants can easily dominate the signal.

4.2 Pure (as Purchased) $SrTiO_3$

Initial measurements were conducted on two individual samples from all three manufacturers. All samples measure 5mm×5mm×1mm and have both faces (5mm×5mm)

factory polished while the four sides (5mm×1mm) are left unpolished (rough). Figure 4.1 shows the total measured magnetic moment for these initial samples. When the standard analysis technique (as described in section 2.2) is performed a primarily diamagnetic response can be seen from all six samples with an average susceptibility (χ) of -9.5×10$^{-8}\frac{emu}{g}$ ± 6×10$^{-9}\frac{emu}{g}$. Figure 4.1 shows that the response of the STO substrate samples is similar with all three manufacturers. Of interest, in each of the six (as received) samples, a small deviation around zero applied field can be seen. By subtracting out the pure diamagnetism (by using the susceptibility calculated from the linear regions) a small ferromagnetic signal can be observed. Figure 4.2 shows two examples of magnetic responses with the diamagnetism removed. In both cases (more so with the MTI-001 sample) hysteresis can be observed. The opening of these hysteresis loops is very small and is within the bounds of the magnetometer error.

Measurements were also conducted on a pair of as purchased $SrTiO_3$ single crystals from Crystec that had different surface characteristics from those shown in figures 4.1 and 4.2. Both samples measured 5mm×5mm×0.5mm with one face polished while the rest of the surfaces were left rough. Both crystals were clear however the unpolished face rendered them translucent rather then transparent. Figure 4.3 shows the magnetic moment from the single crystal samples, labeled CRS-003 and CRS-004. Around zero applied field a feature can be seen once again (upper part of figure 4.3). The diamagnetic susceptibility for both samples (χ being -9.3±0.4×10$^{-8}\frac{emu}{g}$ and -8.6±0.4×10$^{-8}\frac{emu}{g}$ for CRS-003 and CRS-004 respectively) agrees (within experimental error) with the samples that had both faces polished. The lower graph of figure 4.3 shows the same samples with their diamagnetic components removed. Both samples show a clear ferromagnetic hysteresis with saturation magnetizations of approximately 2×10^{-5} $\frac{emu}{g}$ and 4×10^{-5} $\frac{emu}{g}$ for CRS-003 and CRS-004 respectively. The inset shows the hysteresis curves between negative one thousand and one thou-

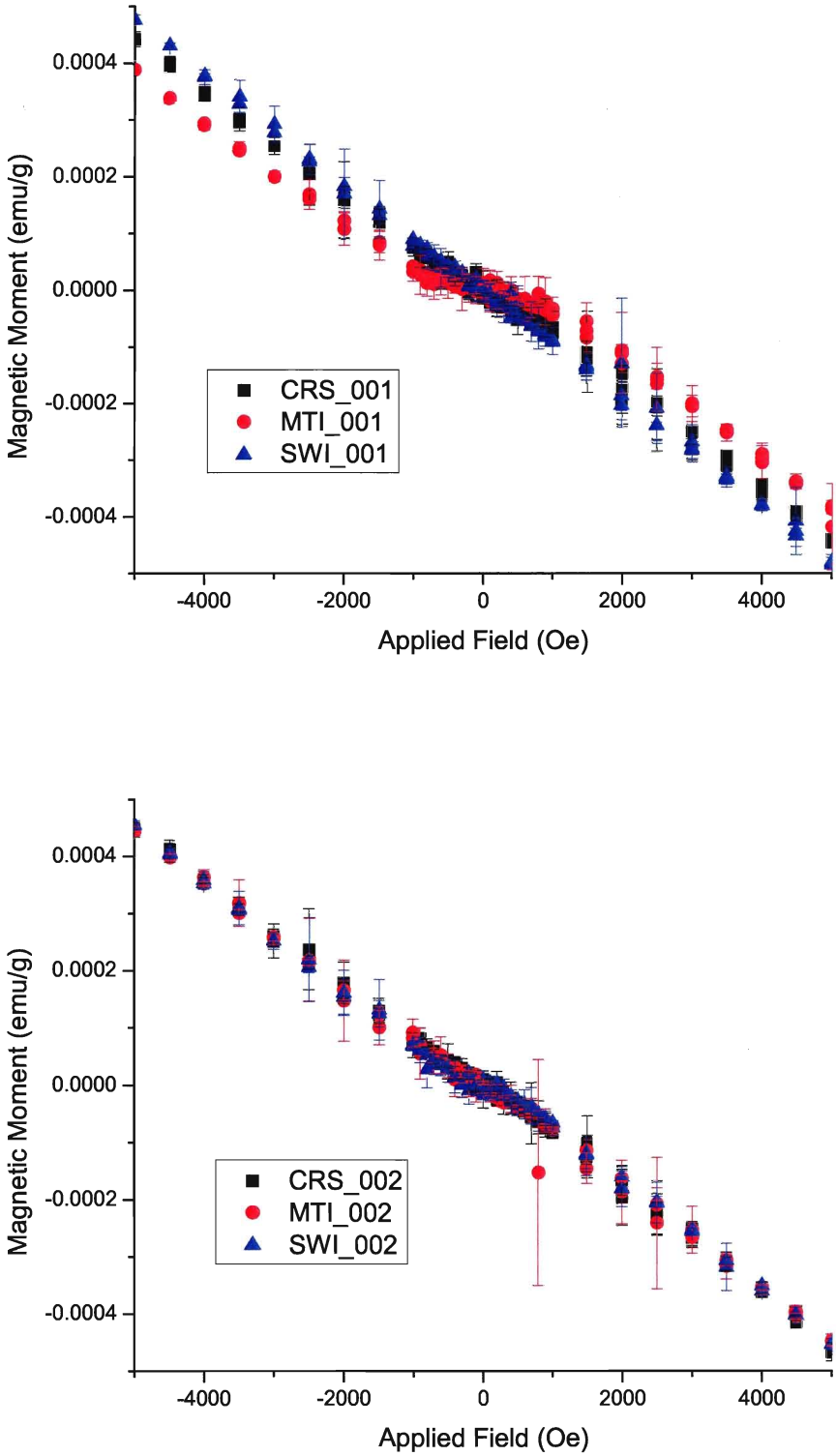

Figure 4.1: **Six initial $SrTiO_3$ samples as received. All samples in normalized units (emu/g).**

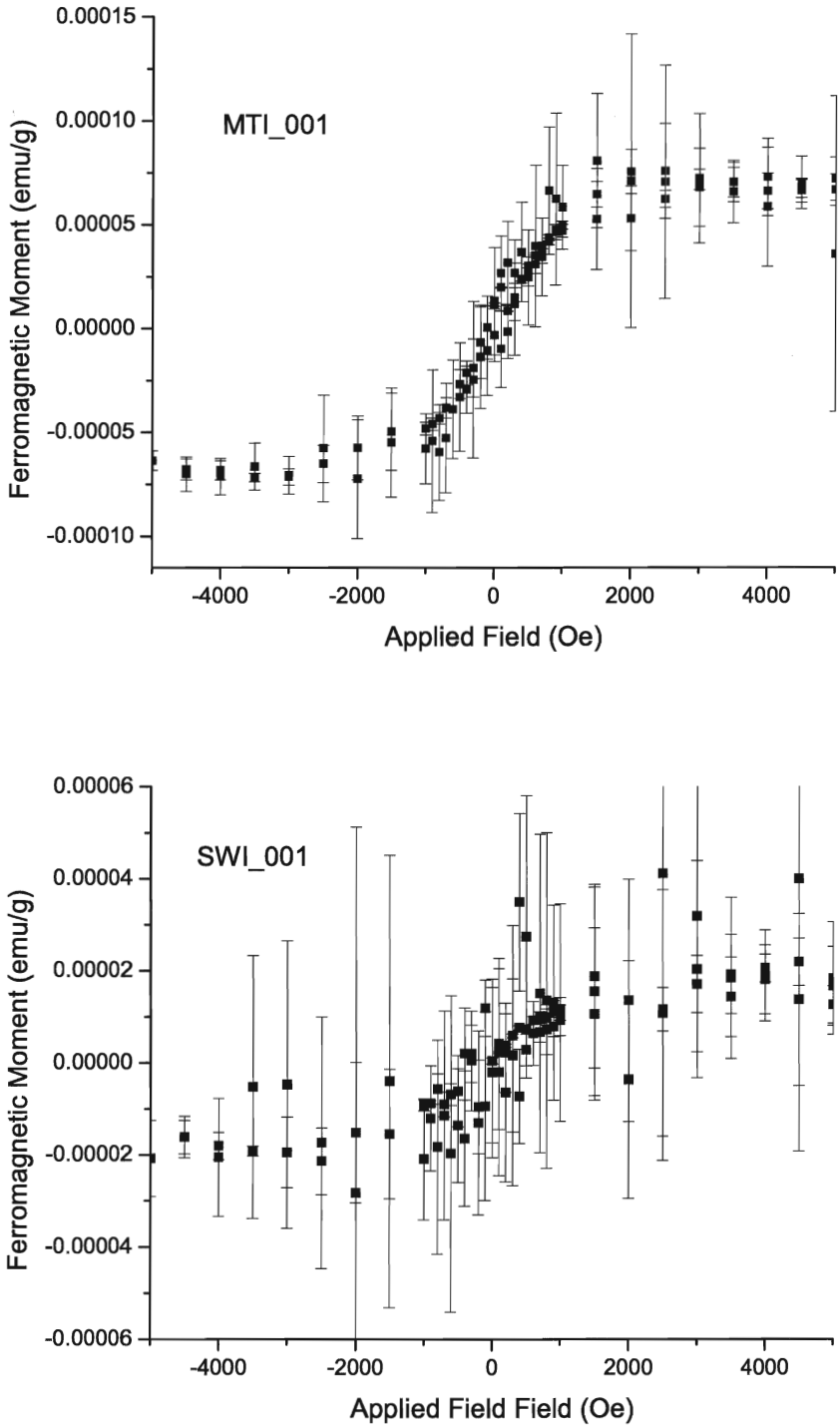

Figure 4.2: **Two samples as received with their diamagnetic components removed.**

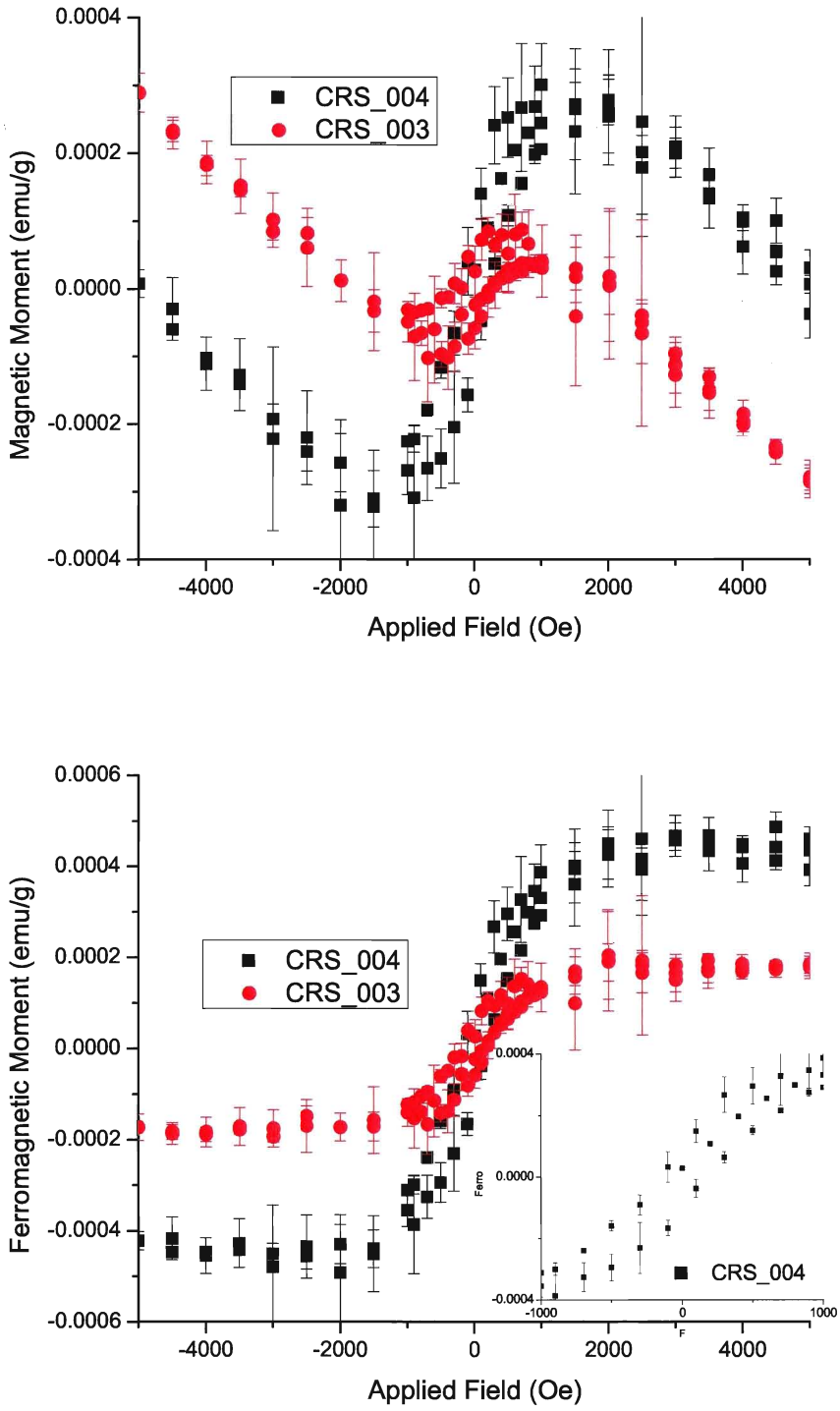

Figure 4.3: **Magnetic moment of Crystec 5mm×5mm×0.5mm single crystal $SrTiO_3$ as received (upper). Magnetic moment with diamagnetic contribution removed (lower), in normalized units (emu/g).**

sand oersted. Both curves have clear openings that are not lost to magnetometer error, a clearly ferromagnetic behavior. The ferromagnetic saturation for each of the two identical samples differs by a significant amount with CRS-004 having roughly twice the saturation moment of CRS-003. Both samples came from the same manufacturer and should have the same level of purity (99.99%) and should have been produced by the same method. Potential explanations could be the surface defects (such as dislocations and bubbles) as mentioned in section 1.6.1 or the presence of ferromagnetic contaminants (such as iron) on the surface of the crystal. As each individual crystal would be subjected to different stresses during the manufacturing process (due to different locations in the boule) each crystal would possess a different amount of these defects. This would suggest that these defects could potentially be a source of ferromagnetism. Many other one face polished samples were measured over the course of research for this thesis and a wide range of ferromagnetic saturation moments were found as seen in appendix A. All of these samples share the same manufacturer, purity and production methods and measured results have been normalized per gram to allow for direct comparison of samples.

To test for the presence of external contaminants as suggested by some previous research [19] sample CRS-003 was cleaned. This cleaning took place in an ultrasonic cleaner in an acetone bath for an hour and a half. A second cleaning took place with the same cleaning method except the acetone bath was replaced with an ethanol bath. The goal of these cleanings was to use the ultrasonic cleaner to remove lose contaminants that the crystal may have scratched off of surfaces that it has come into contact with. CRS-003 was measured after cleaning however the cleaning had no effect on the magnetic response. This supports the theory that the moment originates from features present in the crystal structure that can not be shaken loose as opposed to external contaminants that the crystal had acquired through storage and handling.

This cleaning method however, would not work if the contaminants present in the single crystal were fused or otherwise embedded into the crystal itself. In order to remove contaminants such as these the surfaces would need to be removed. This removal was accomplished through polishing as described in section 3.8.

4.3 Polishing of Single Crystals

Results obtained from the 5mm×5mm×0.5mm Crystec samples showed that one face polished samples have a significant amount more ferromagnetic signal when compared to the two face polished samples, when normalized per gram. Using the polishing procedure outlined in section 3.8, one face rough samples were polished. After polishing, all samples still had a small number of visible surface scratches, however, the bulk of the surface was polished to a smooth finish. Figure 4.4 (upper panel) shows sample CRS-004 before and after polishing of the rough 5mm×5mm face. After polishing the large ferromagnetic hysteresis has been reduced considerably. After normalization the two face polished CRS-004 sample resembles that of the 5mm×5mm×1mm samples from figure 4.1. The central feature around zero applied field is still more pronounced in the polished CRS-004 however this can be attributed to the four 5mm×0.5mm sides of the crystal as well as imperfections in the polishing which would be magnified after normalization due to the reduced mass of CRS-004. The reduction in ferromagnetism is more clearly seen in figure 4.4 (lower panel) which shows the ferromagnetic contribution to the magnetic moment for CRS-004. Polishing the surface of CRS-004 removed approximately seventy five percent of the existing ferromagnetic moment. This would suggest that the origin of the ferromagnetism in the $SrTiO_3$ would be more highly located on the rough surfaces of the sample. The suggestion of a surface based ferromagnetism agrees with results found from other oxide semiconductors

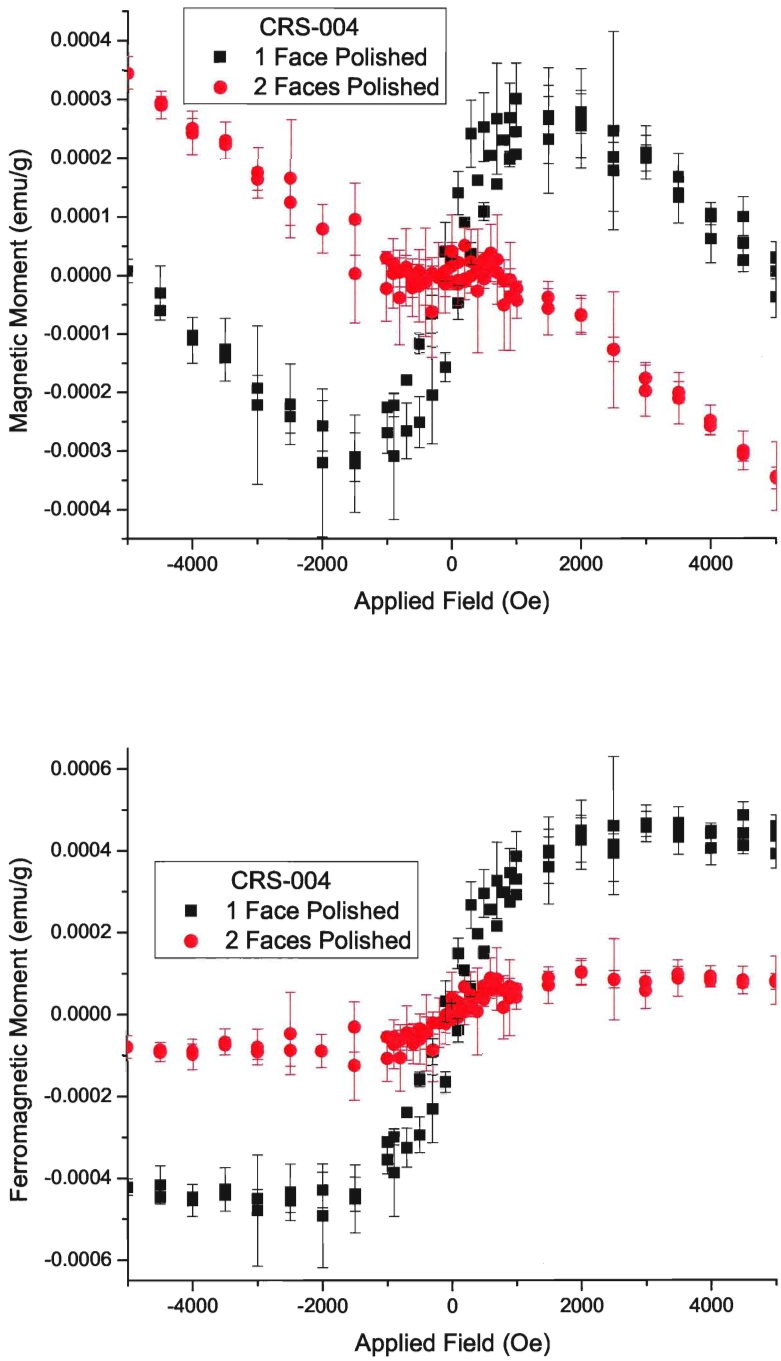

Figure 4.4: **CRS-004 with one and two faces polished (upper). Ferromagnetic contribution (lower), in normalized units (emu/g).**

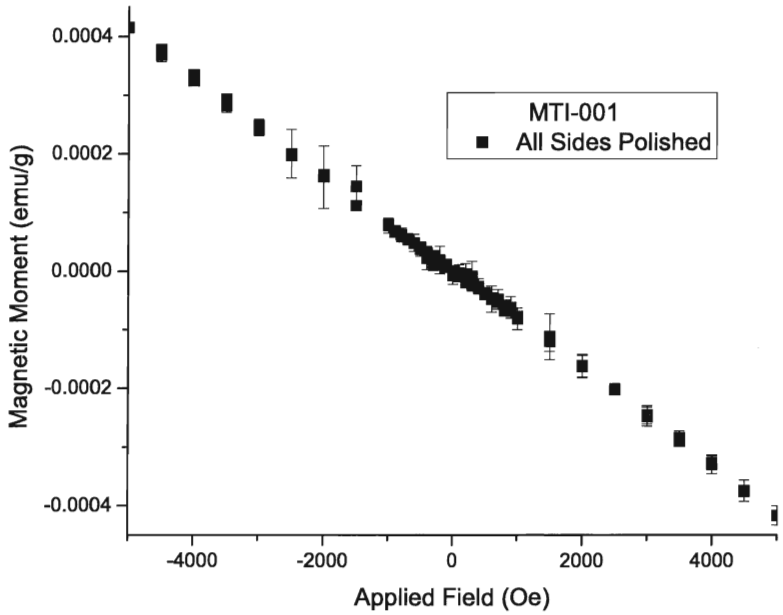

Figure 4.5: **Effect of side polishing on MTI-001, in normalized units (emu/g).**

such as TiO_2 [15], HfO_2 [13] and ZnO [17, 18]. However, this surface based ferromagnetism could originate from impurities such as non-perovskite phases [23, 26], tweezer contamination [19] or embedded impurities left over from the manufacturing process, from a diamond saw cut for example.

To further examine this surface effect ferromagnetism the four 5mm×1mm sides of previously measured samples were polished using the same procedure outlined in section 3.8. The four sides have a total surface area of $20mm^2$ which is comparable to the $25mm^2$ surface area of the faces. The result of polishing these sides can be seen in comparing figure 4.5 with figure 4.1. Polishing of the sides reduced the ferromagnetic deviation around zero applied field, essentially leaving nothing but a pure diamagnetism. This result strongly suggests that ferromagnetism in $SrTiO_3$

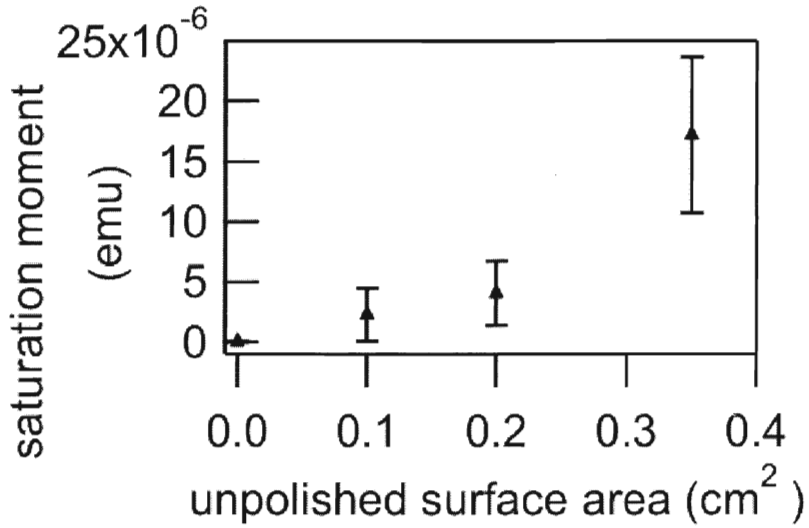

Figure 4.6: **The average ferromagnetic saturation moment as a function of unpolished surface area. Uncertainty bars show standard deviation between samples as presented in appendix A**

originates from the unpolished surface of the crystal. Other samples showed the same effect when they had their sides and faces polished, as can be seen in appendix A with samples such as STO-D and STO-E.

In order to furthur visualize the effect of surface polishing all of the measured results were compiled into figure 4.6. This figure clearly relates a high measured saturation moment to a large amount of unpolished surface area.

This surface effect ferromagnetism is not easily reintroduced however. Two face polished sample SWI-002 was deliberately roughened with four hundred grit emory-paper using the same procedure as the initial polishing step, mentioned in section 3.8. Upon visual inspection the roughened side of the sample resembled that of the as received samples with one rough side, in essence the transparent crystal face was rendered translucent. The sample was cleaned using an ultrasonic cleaner with an acetone bath to remove contamination left over from the roughing process. The sam-

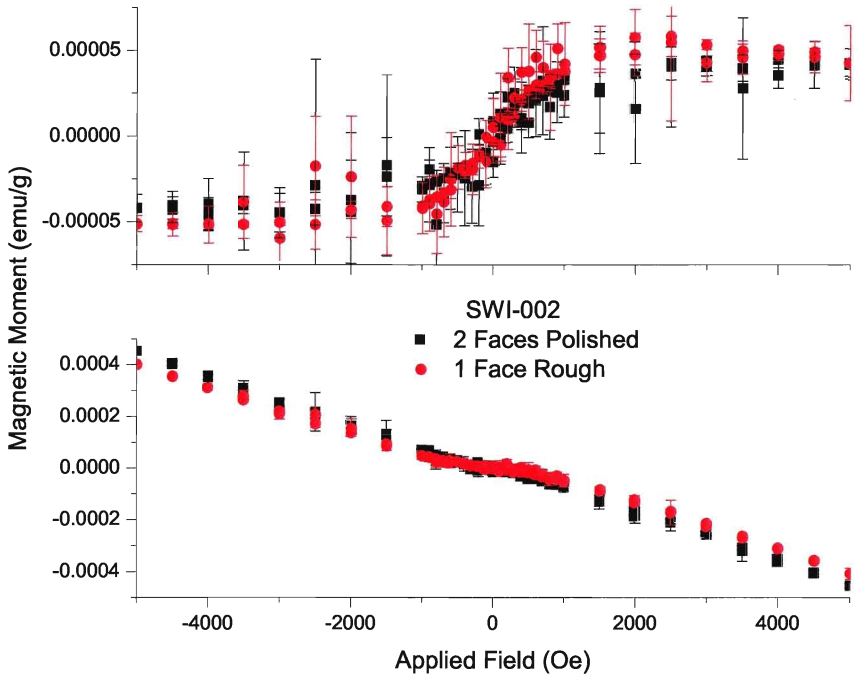

Figure 4.7: **Ferromagnetic moment with diamagnetic contribution removed (upper). Magnetic moment of SWI-002 as received (2 faces polished) and 5.5 months after 1 face roughing (lower), both in normalized units (emu/g).**

ple was then measured with the SQUID magnetometer and no change in the magnetic moment of the sample was observed. Figure 4.7 shows two different measurements of sample SWI-002 both with normalized units for direct comparison. The lower portion shows SWI-002 as received and five and a half months after roughing while the upper portion shows the ferromagnetic moment obtained when the diamagnetism is removed. The lower portion shows that even after a considerable amount of settling time there was little change in the deviation around zero applied field. The upper graph shows that the act of roughing up the surface does not appear to have an effect on the ferromagnetic saturation moment as it remained virtually unchanged when magnetometer error is taken into account. These results suggest that the rough surface alone is not the source of the ferromagnetism but how the surface is created could still be a cause. This suggests that the polishing procedure used induces less stress on and in the crystal than a diamond saw or wire saw cut. With less stress induced on the crystal, stress induced defects such as bubbles and dislocations [24] would not be as abundant as they would be with a diamond/wire saw cut.

4.4 $SrTiO_3$ Powder and Pellets

A $SrTiO_3$ powder (manufactured by Afla Aesar) was measured for comparison with single crystals. The powder was chosen as the work on the single crystals suggests that the ferromagnetism originates from the unpolished surfaces. This powder consists of 0.05μm - 0.15μm particles with surface areas ranging from $12.5\frac{m^2}{g}$ - $25\frac{m^2}{g}$. The difference in surface area when compared to the traditional 5mm$\times$5mm$\times$1mm sample (approximate surface area 6×10^{-4} $\frac{m^2}{g}$.) is large, on the order of ten thousand. As the powder cannot be measured in the SQUID as is, a container is required to hold the powder during measurement. For this container a number 2 gelatin capsule (or

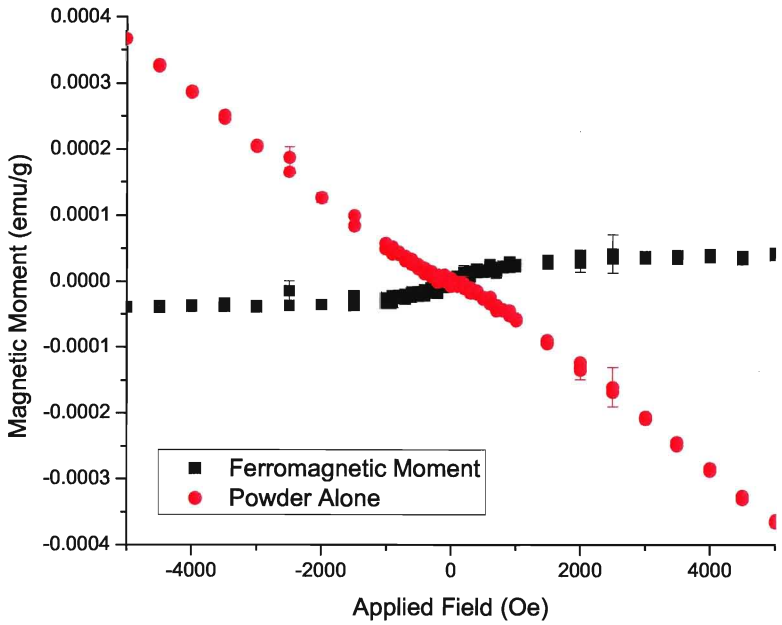

Figure 4.8: **$SrTiO_3$ powder measured moment with capsule contribution removed, in normalized units (emu/g).**

gelcap) was used with a wad of paper placed at the top to prevent the powder from escaping during the initial SQUID vacuum pumping process. As the gelcap and paper possess an intrinsic moment two separate measurements were conducted, one with and one without powder. In this way the response from the gelcap and paper could be subtracted out leaving the magnetic response of the powder alone (Figure 4.8). Once again a primarily diamagnetic response was measured however the small deviation during the application of small field persisted. The calculated diamagnetism (χ) using the analysis technique from section 2.2 is $8.12\times10^{-8}\ \frac{emu}{g} \pm 5\times10^{-10}\ \frac{emu}{g}$. When this diamagnetism is subtracted out once again the magnetometer noise is larger than the potential ferromagnetic hysteresis observed.

This same powder was then pressed into pellets using the procedure outlined in

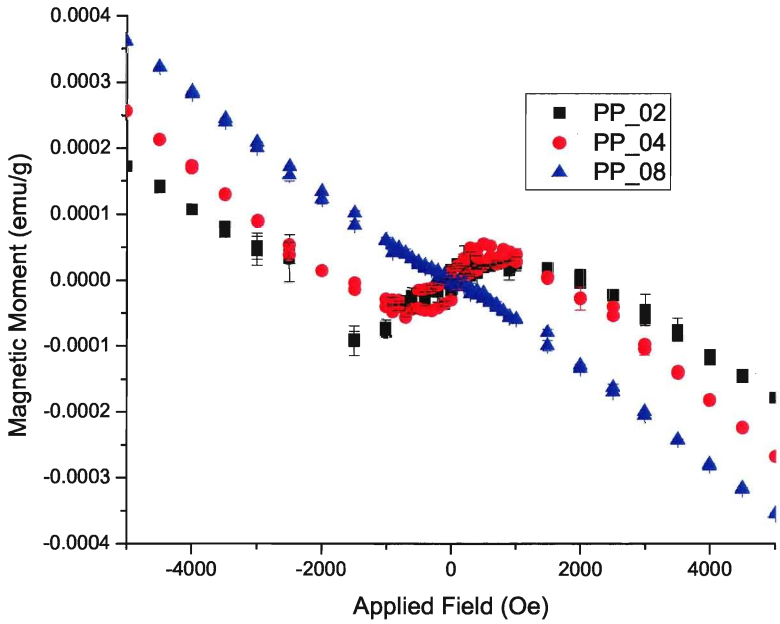

Figure 4.9: **Magnetic Moment vs Applied Field for $SrTiO_3$ pellets with gelcap contribution removed. Pellets pressed in order of 02, 04 then 08. All measurements have normalized units (emu/g).**

section 3.7. The downside to using this procedure was that the pellets, upon being removed from the plastic die had obtained a ring of material from the die itself. This contamination itself was embedded into the pellet and not easily removed. This contamination however was somewhat consistent on the pellets made with the die, each pellet having an equally sized ring of contamination. The pellets were measured in much the same way as the powder with a separate gelcap being measured for each pellet. After subtracting out contribution to the magnetic moment from the gelcap the moment for the pellet alone was obtained. Measurements of early (initial) pressed pellets showed a clear hysteresis curve near zero applied field. However, as further pellets were pressed and measured this hysteresis was gradually reduced in

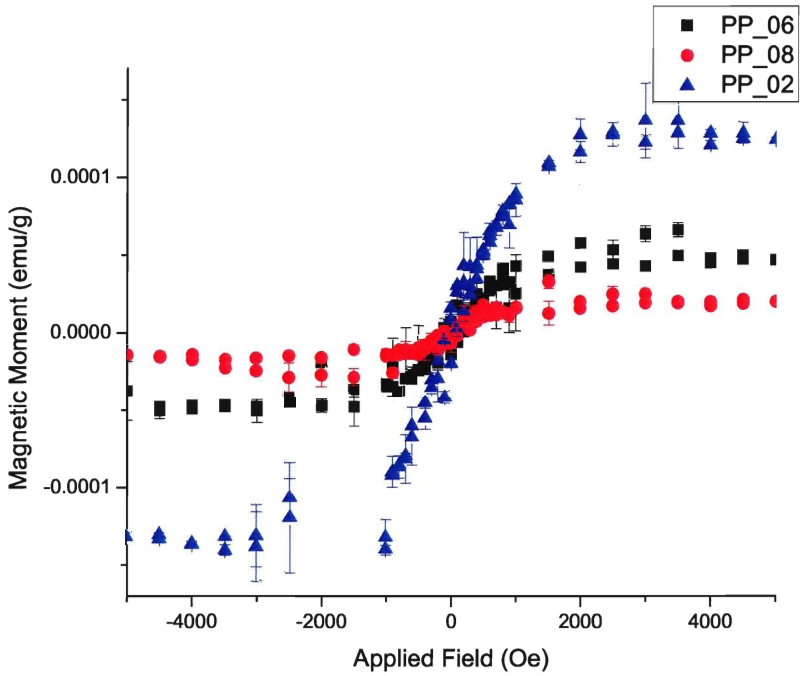

Figure 4.10: **Ferromagnetic Moment vs Applied Field for $SrTiO_3$ pellets with gelcap and diamagnetic contributions removed. Pellets pressed in order of 02, 06 then 08. All measurements have normalized units (emu/g).**

magnitude. Figure 4.9 shows this gradual decline of the hysteresis with respect to pellet pressing order (chronological order). This would suggest that the supposedly non-magnetic materials of the pellet die are somehow affecting the magnetic properties of the pellets. This reduction of hysteresis effect can be better seen in Figure 4.10 which shows the ferromagnetic saturation moment with respect to applied field. This graph clearly shows that the ferromagnetic component decreases as more pellets were created. To further test this effect small pieces of the pellet pressing die were removed and measured separately, as the die was constructed from two separate materials both were measured. The pieces (Al-Chunk and the plastic called Black-Chunk from

appendix A) both were found to have a substantial ferromagnetic moment perhaps originating from the cutting tools. All pellets pressed did show some amount of ferromagnetic moment around zero applied field with the later pellets showing less of a ferromagnetic moment. The ferromagnetic moment of the later pellets begins to approach that of the loose powder when normalized per gram. This suggests that the act of pressing the powder into a pellet does not imbue it with a ferromagnetic moment, instead it suggests that the moment measured originated from varying levels of contaminants originating from the pellet pressing die.

4.5 Niobium Doped $SrTiO_3$

Samples were also purchased from MTI Corporation that were doped with 0.7% and 1% niobium. The crystals appeared black rather then clear because niobium takes the place of the titanium in the $SrTiO_3$ crystal. This change renders the $SrTiO_3$ metallic, similar to the act of removing an oxygen atom to create an oxygen vacancy. The upper graph in figure 4.11 shows the effect of this doping on two 5mm×5mm×0.5mm Nb:$SrTiO_3$ samples both with one face polished and all other surfaces left rough. Once again a feature is clearly visible around zero applied field, with a transition to a straight diamagnetic response at higher fields. The diamagnetic susceptibility of the niobium doped strontium titanate is less than that of the pure strontium titanate. This difference in susceptibilities can be attributed to the increase in a paramagnetic component stemming from the excess free carriers from the niobium. The increased amount of niobium in the sample also can be seen in the susceptibilities, with the 1% Nb doped sample having more free electrons so the diamagnetic susceptibility, as expected, is lower. χ for 1% being -3.2×10^{-8} $\frac{emu}{g}$ ± 1×10^{-9} $\frac{emu}{g}$ as compared to -3.7×10^{-8} $\frac{emu}{g}$ ± 2×10^{-9} $\frac{emu}{g}$ for the 0.7% doped sample. The lower part of

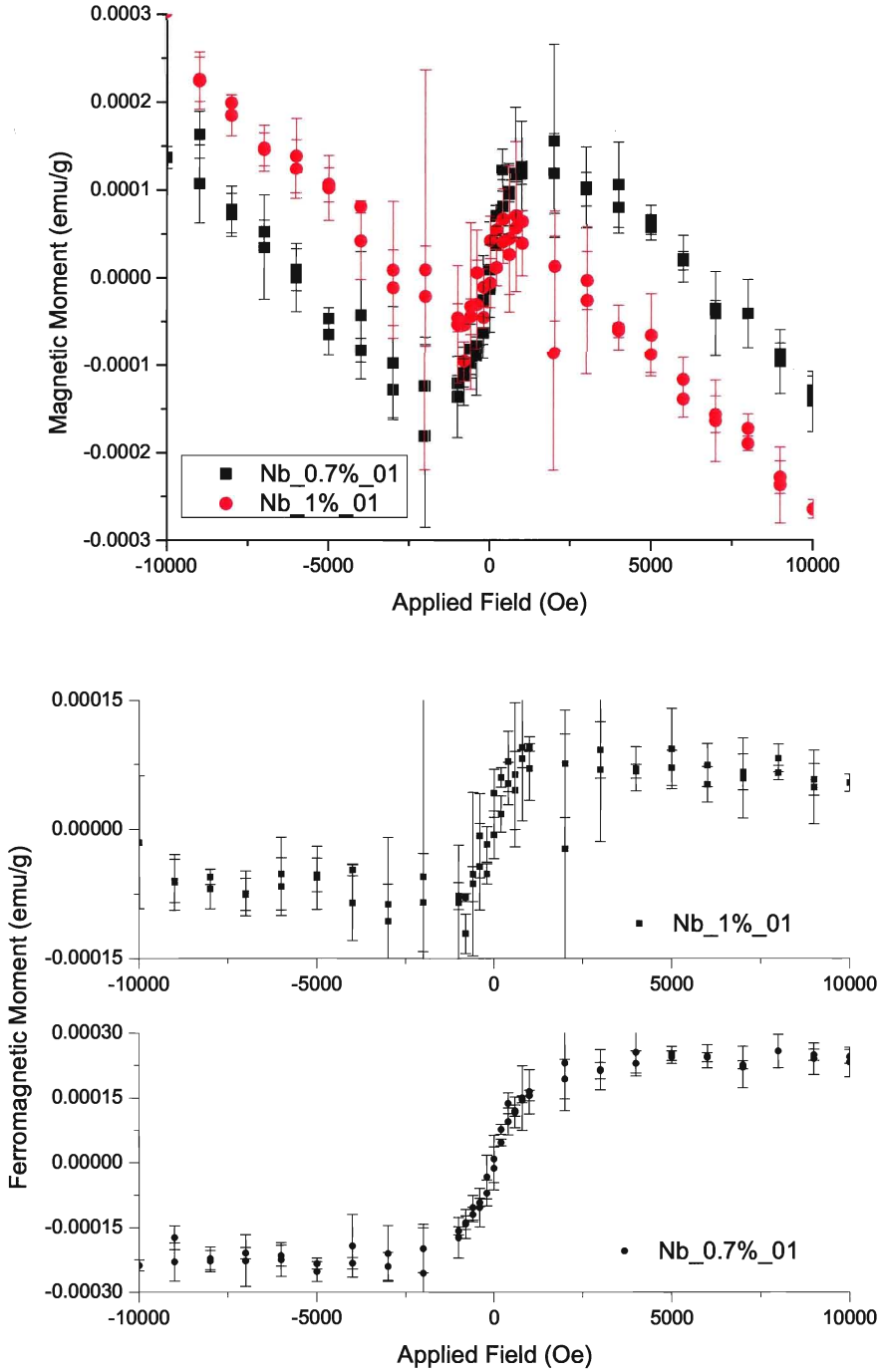

Figure 4.11: **Magnetic moment of Nb:$SrTiO_3$ with Nb concentrations of 0.7% and 1.0% (upper). Magnetic moment with diamagnetic contribution removed (lower), in normalized units (emu/g).**

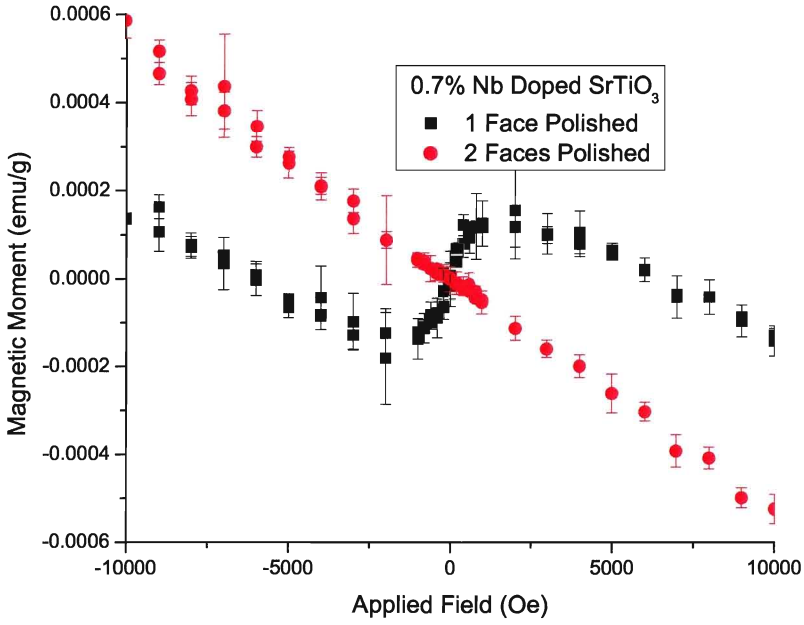

Figure 4.12: Effect of face polishing on 0.7% Nb doped $SrTiO_3$, in normalized units (emu/g).

figure 4.11 shows the individual Nb:$SrTiO_3$ samples with their respective diamagnetic contributions removed. This figure shows that the ferromagnetic saturation for the 0.7% is nearly twice that of the 1% sample. Also visible around zero applied field (more so for the 1% sample) a potential hysteresis curve can be seen, however any opening is lost to measurement error.

To test the effect of polishing on the niobium doped samples the rough face of the single crystal was polished using the same procedure (outlined in section 3.8) as with the pure single crystals. Once again a small number of surface scratches were still visible on the surface that had been polished, however the vast majority of the surface roughness was removed. Figure 4.12 shows the effect of face polishing on two separate 0.7% niobium doped $SrTiO_3$ samples. As seen with CRS-004 before polishing

of the rough face a large ferromagnetic moment is observed however this is almost completely removed when the face is polished. While two separate samples were compared these results were similar to those found by using the same 1% niobium doped sample (before and after polishing) as seen in appendix A.

4.6 Energy-Dispersive X-ray Spectroscopy

Energy-Dispersive X-ray Spectroscopy (or EDX as outlined in section 3.3) was performed on a number of one face polished samples. The purpose of these measurements was to determine if a significant amount of a particular impurity was present on the surface. The maximum energy was deliberately kept low to restrict the EDX measurement to just the surface of the sample. An approximate penetration depth of 0.6μm was calculated through equation 4.1 [39] where x is the penetration depth in microns, E_0 is the incident electron energy in keV and ρ is the density of the material measured in $\frac{g}{cm^3}$.

$$x = \frac{0.1E_0^{1.5}}{\rho} \tag{4.1}$$

EDX measurements were performed on both the rough and polished faces of several samples and showed the same result which can be seen in figure 4.13. As these impurities could be localized, several measurements were performed on different locations of the same face on each $SrTiO_3$ crystal. No peaks from magnetic impurities were noticed however there was a peak visible at 3.7KeV which originates from Calcium.

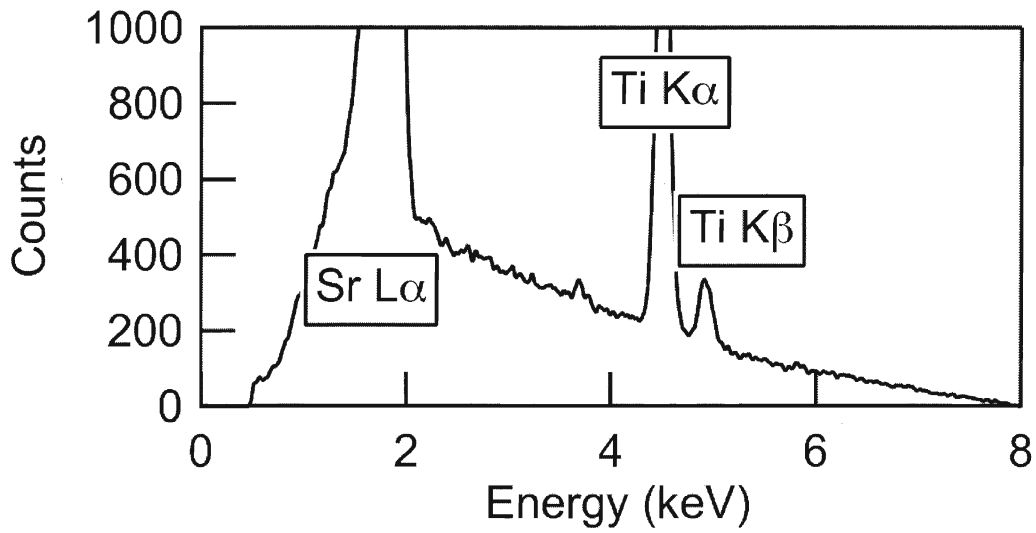

Figure 4.13: **EDX measurement for as received $SrTiO_3$ sample.**

4.7 Effects of Reduction

4.7.1 Single and Double Face Polished Samples

Reduction experiments were performed to introduce oxygen vacancies, anneal out bubbles and dislocations (as mentioned in section 1.6.1), and to otherwise change the physical properties of the samples. As seen earlier in figure 1.9, previous work [21] had shown that when a non-ferromagnetic $SrTiO_3$ sample was reduced at 900°C it became ferromagnetic. In an attempt to recreate this work, six as purchased two face polished samples (all of which have little to no ferromagnetic moment as seen in figure 4.1) were reduced using the procedure outlined in section 3.6.1. These reductions were done at a range of temperatures from 600°C to 1100°C as seen in figure 4.14. As can be clearly seen reduction at 900°C did not create the moment previously measured. This systematic reduction shows no creation of magnetic moment however the optical and electrical properties of the sample did change which can be seen in sections 4.7.2 and section 4.7.3 respectively.

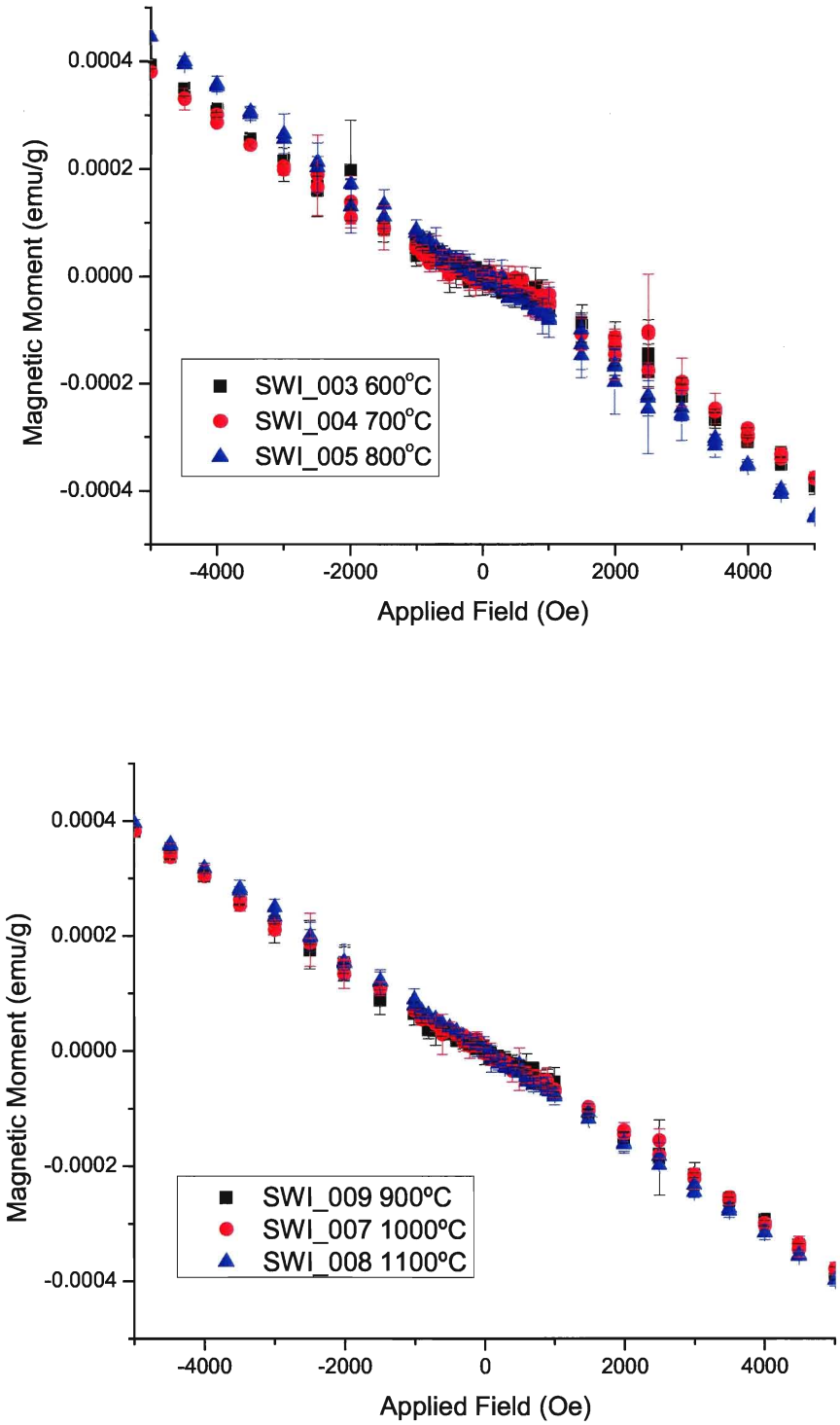

Figure 4.14: **Systematic reduction of two face polished $SrTiO_3$, in normalized units (emu/g).**

The same systematic reduction experiment was performed on one face polished samples. As previous findings had shown these one face polished samples to already posses a significant unique moment (see figure 4.3) each of these samples was measured before and after the reduction procedure to view the effect induced by reduction. The results of the low temperature (600°) reduction can be seen in figure 4.15 which shows that the reduction reduced the magnitude of the ferromagnetic moment observed. Similarly the results of the high temperature (1100°) reduction also show a more drastic reduction in the ferromagnetic moment observed, which can be seen in figure 4.16. While this gradual destruction of the ferromagnetic moment with respect to the reduction temperature contradicts previous findings, it is systematic and reproducible. The full results of these reduction experiments can be seen in appendix A. Also, the reduction experiments did produce some other results of interest, these can be found in appendix B.

4.7.2 Optical data

Optical work was done on the two face polished $SrTiO_3$ samples that had been systematically reduced. The goal of the optical measurements was to reinforce and quantify the observed darkening of the samples. Optical measurements were done using the procedures outlined in section 3.5 and 3.5.2 and can be seen in figure 4.17[1]. These graphs clearly show the observed darkening of the crystals (in the form of reduced visible optical transmission) along with some other features of interest. The foremost being the band edge at 372nm (approximately 3.3eV) visible in the upper graph. Also visible in both the upper and lower graphs are a series of systematic peaks and troughs which lessen in intensity at greater reduction temperature.

[1]Note that SWI-005 is absent from half of the figure as it was unable to be mounted for measurement properly

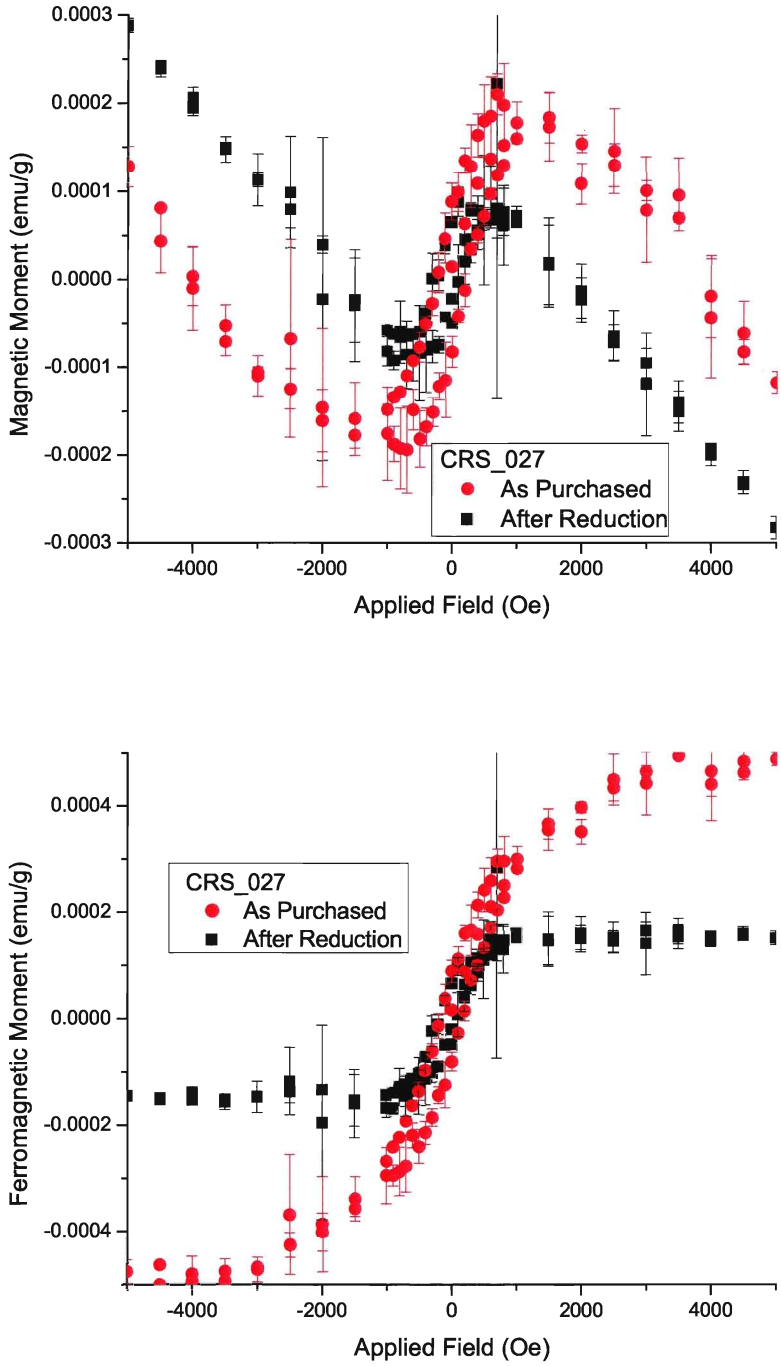

Figure 4.15: **Effect of reduction at 600°C on one face polished $SrTiO_3$ (Upper). With diamagnetic contribution removed (Lower), in normalized units (emu/g).**

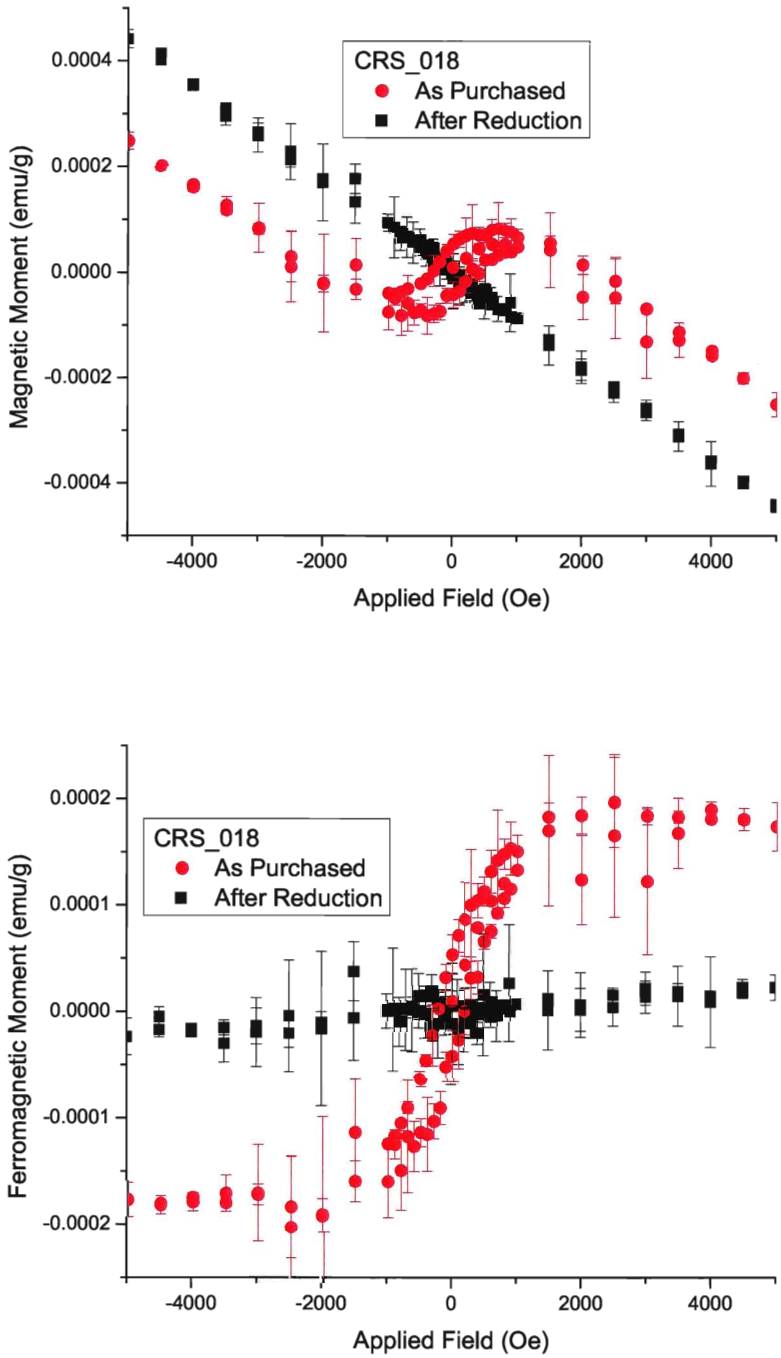

Figure 4.16: **Effect of reduction at 1100°C on one face polished $SrTiO_3$ (Upper). With diamagnetic contribution removed (Lower), in normalized units (emu/g).**

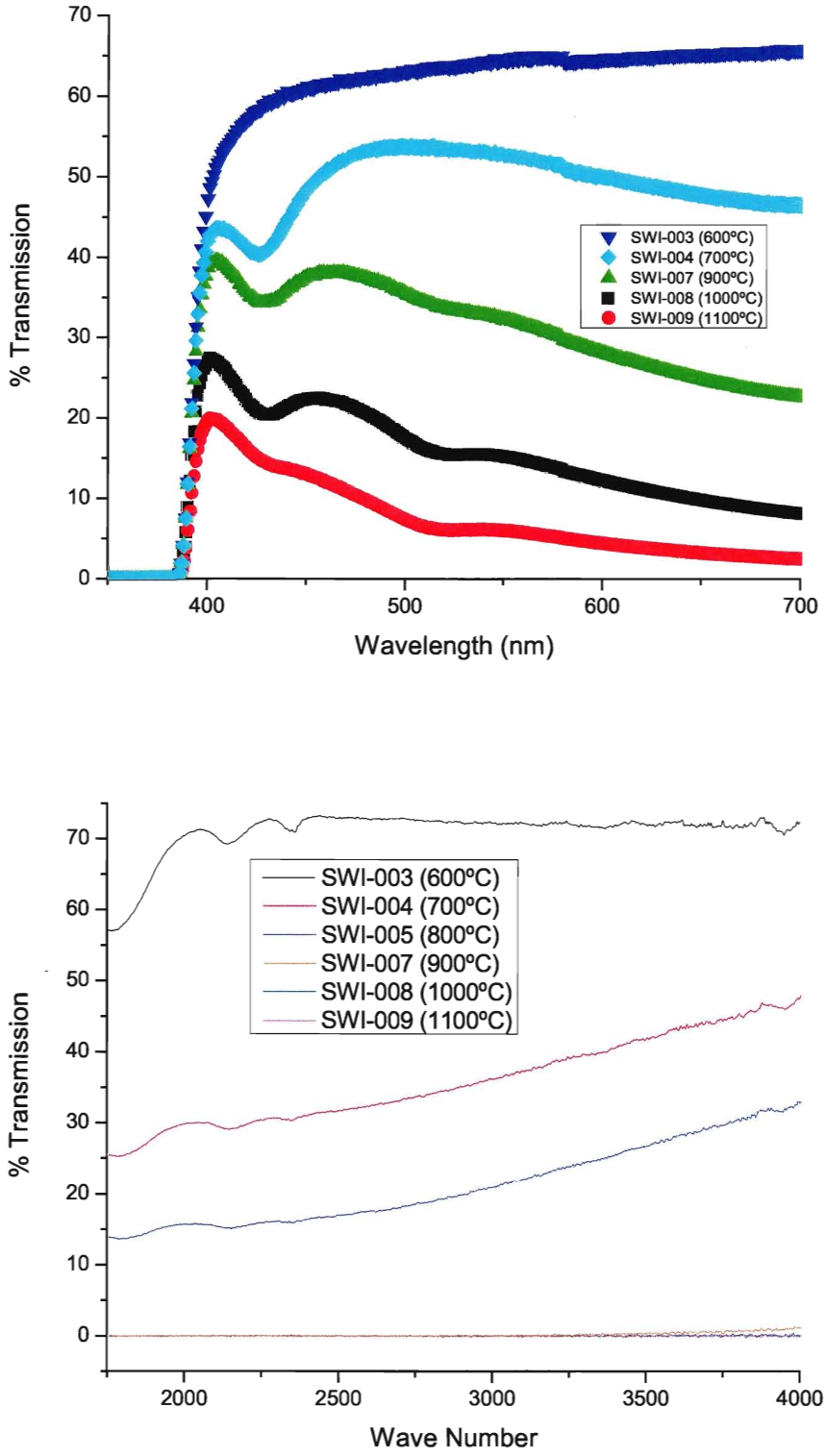

Figure 4.17: **Optical transmission of systematically reduced two face polished $SrTiO_3$ for visible (Upper) and for infrared (Lower).**

Sample Name	Reduction Temperature (°C)	Room Temperature Resistivity (mΩ·cm)
SWI-005	800	903
SWI-009	900	132
SWI-007	1000	35
SWI-008	1100	22

Table 4.1: Room temperature resistivity for reduced $SrTiO_3$ substrates.

4.7.3 Resistivity Measurements

Resistivity measurements were done on a selection of reduced $SrTiO_3$ samples to ensure that the free carriers induced through reduction (as mentioned in section 3.6.1) were actually present in the samples. In order for the resistivity to be measured through the van der Pauw method (as mentioned in section 3.4) it was first necessary to evaporate a thin layer of chromium followed by a thin layer of gold on the corners of the samples in order to make contacts with the sample that possessed acceptable resistances. Figure 4.18 shows the measured resistivity for four reduced two face polished samples. This figure shows that as the reduction temperature is increased the resistivity of the sample drops which suggests that reduction is introducing free carriers. Table 4.1 shows the room temperature resistivity values for the reduced samples.

$$\rho \approx \frac{10^{21}}{n} \tag{4.2}$$

These room temperature (300°K) resistivities were then used with a calibration equation [28] to calculate an approximate carrier concentration as seen in equation 4.2, where ρ is the room temperature resistivity and 'n' is the hall free carrier concentration. These approximate carrier concentrations were then used in figure 4.19,

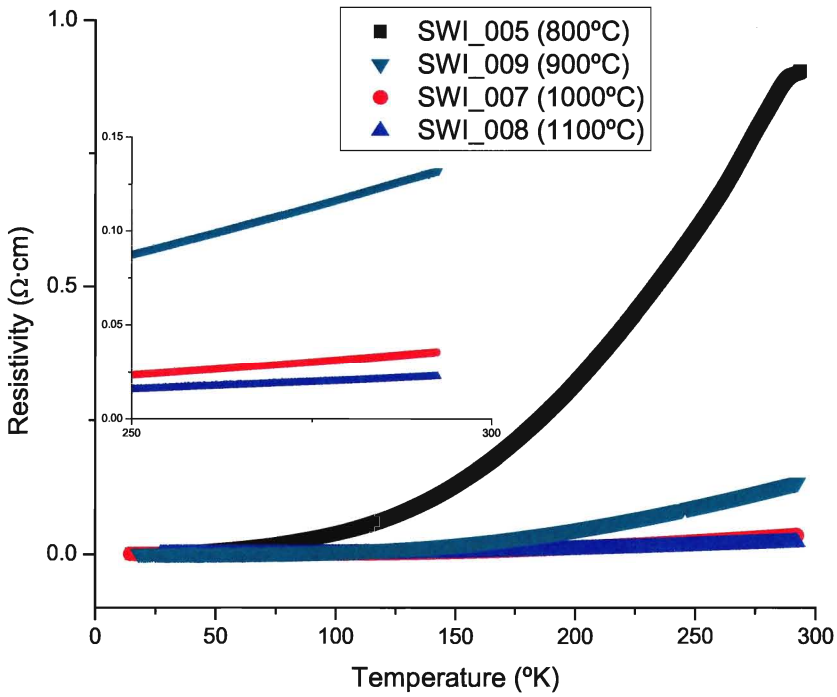

Figure 4.18: **Resistivity versus temperature measurements for reduced $SrTiO_3$ substrates.**

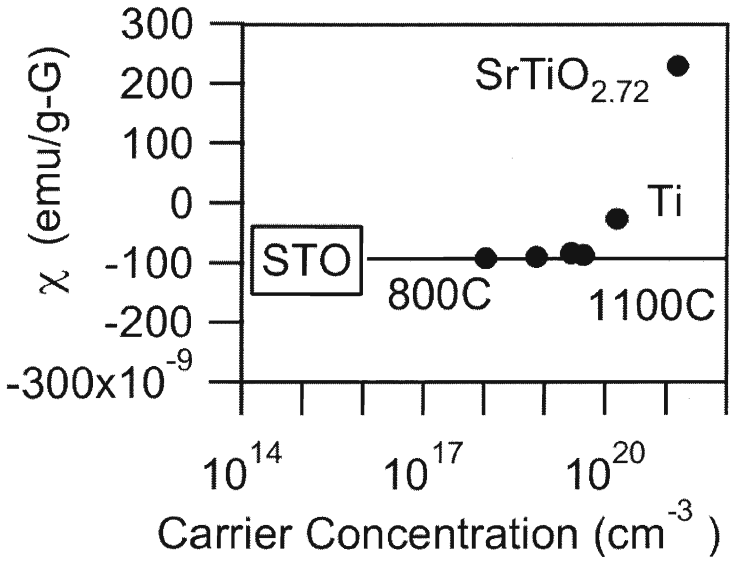

Figure 4.19: **Room temperature susceptibility vs carrier concentration for reduced $SrTiO_3$ substrates at 800°C, 900°C, 1000°C, and 1100°C. 'Ti' represents a single crystal reduced in a quartz tube containing powdered Ti to enhance the reduction. '$SrTiO_{2.72}$' represents a grossly non-stiochiometric single crystal. The horizontal line indicates the measured room temperature susceptibility of pure $SrTiO_3$.**

which compares the room temperature susceptibility of reduced strontium titanate versus the carrier concentration. This figure shows that as the reduction temperature is increased the carrier concentration is increased along with an increasingly paramagnetic change in the magnetic susceptibility. The results in figure 4.19 agree to within 10% of previous measurements [42].

Sample Name	Reduction Temperature (°C)	Approximate Crystallite Size (± 2nm)
Base Powder	N/A	39
PP-07	600	43
PP-08	800	45
PP-05	900	46
PP-04	1000	56
PP-06	1100	69

Table 4.2: Approximate crystallite size as a function of reduction temperature as calculated via the Scherrer equation using the (110) and (200) lines.

4.7.4 Effect of Reduction on Pressed Pellets

The pellets that were pressed earlier (as mentioned in section 4.4) were then systematically reduced in the same way as the single crystals were. The magnetic properties of these pellets after reduction however did not mirror those of the single crystals. As each pellet possessed a different amount of impurities which could have potentially reacted with the aluminum oxide boat (discussed further in appendix B). These impurity levels and reactions prevent the magnetic data from coming back with any sort of systematic pattern. Full results of the magnetic work done on the reduced pellets can be seen in appendix A.

X-ray diffraction measurements were also done on these reduced pellets similar to those mentioned in section 3.2. These x-ray measurements were used as a basis for measurements using the Scherrer equation (as mentioned in section 3.2, equation 3.8) in order to determine the approximate size of the $SrTiO_3$ crystallites. Table 4.2 shows the approximate crystallite size as calculated using an average of the two most intense peaks ((110) and (200), as seen in figure 4.24). As seen in table 4.2 a clear

relation between the increase in reduction temperature and the increase in particle size is observed. This result mirrors those seen in figure 1.8. The magnetic moments of the reduced pressed pellets did not change systematically. This is probably because of the embedded impurities coming from the pellet die referred to in the discussion of figure 4.9.

4.8 Effects of Oxidization

Oxidization experiments were carried out in much the same way as the reduction experiments and for similar reasons, to test the effect of oxidization on the $SrTiO_3$ samples. Once again a series of systematic oxidizations were performed on one face polished samples using the oxidization procedure outlined in section 4.8. Figure 4.20 shows the effect of a low temperature (600°C) oxidization on a one face polished sample. Similarly, figure 4.21 shows the effect of a high temperature (1050°C) oxidization. Figure 4.22 shows a more direct comparison of the magnetization as a result of annealing on the one face polished substrates. These figures (along with the additional measurements listed in appendix A) show a systematic reduction in the ferromagnetic signal with respect to the oxidization temperature.

With the systematic oxidization there was a gradual colour change with samples prepared at a higher temperature visibly appearing more yellow. As this change in colour only occurred in samples with one face polished, optical work to determine the magnitude of this colour transition was not feasible. It was not feasible as a combination of the scattering from the rough surface combined with the increase in opacity prevented accurate optical transmission measurements. To further explore the source of this colour change sample CRS-015 was deliberately contaminated with iron from stainless steel tweezers and then oxidized at 1000°C. Table 4.3 shows the

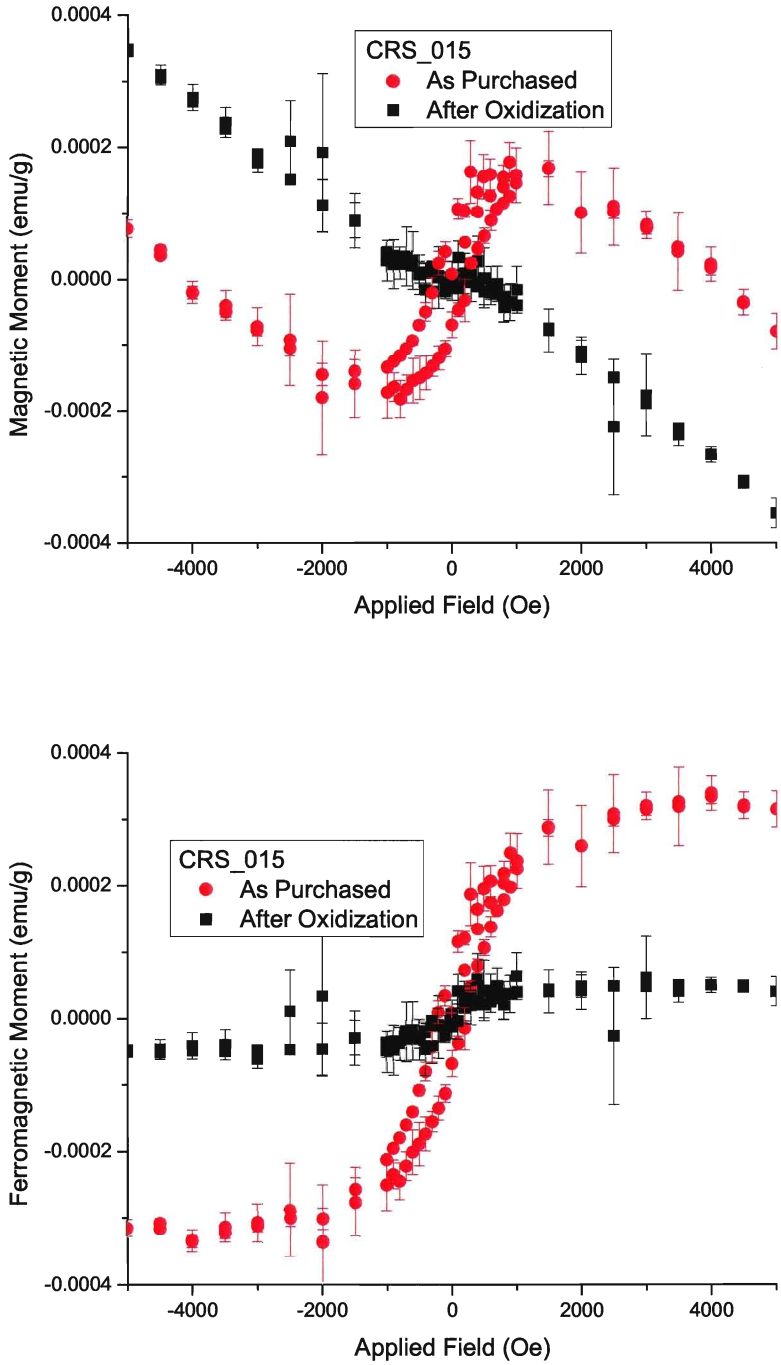

Figure 4.20: **Effect of Oxidization at 600°C on one face polished $SrTiO_3$ (Upper). With diamagnetic contribution removed (Lower), in normalized units (emu/g).**

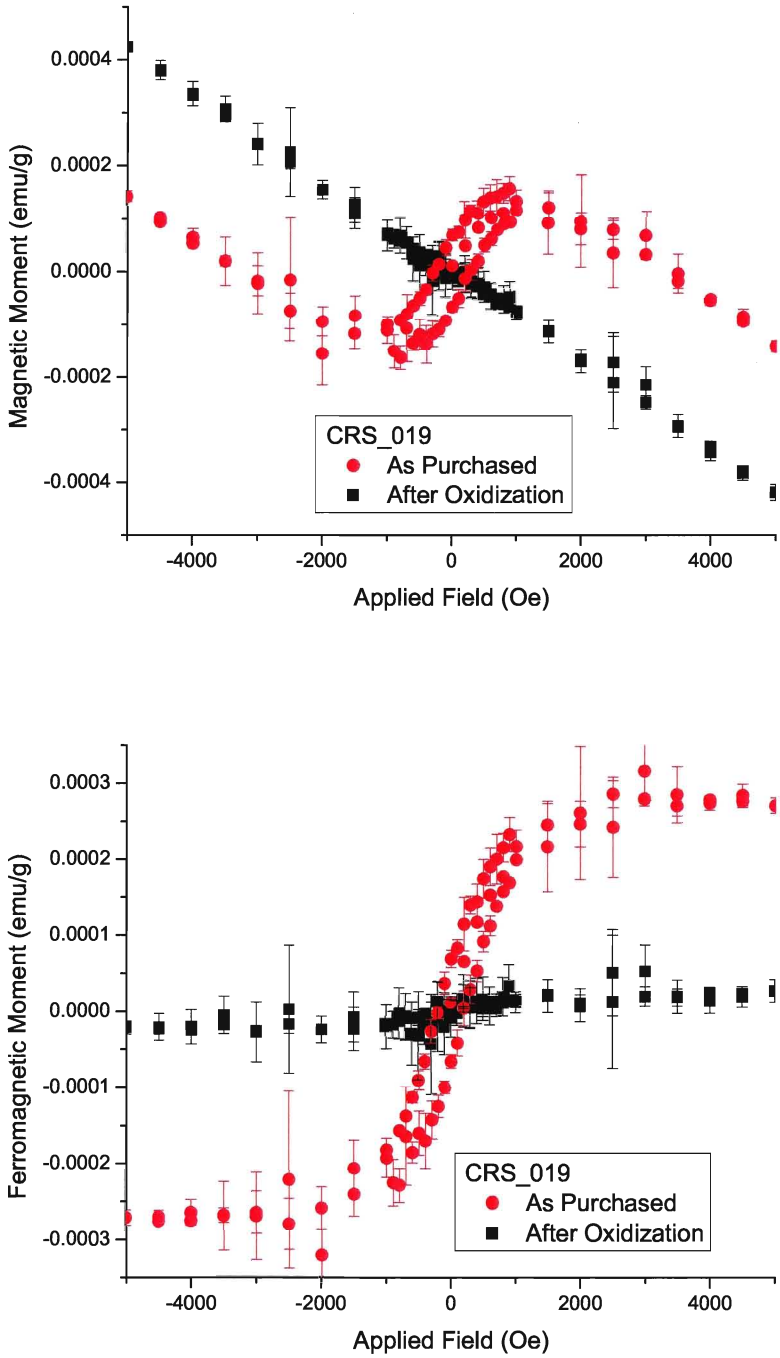

Figure 4.21: **Effect of Oxidization at 1050°C on one face polished $SrTiO_3$ (Upper). With diamagnetic contribution removed (Lower), in normalized units (emu/g).**

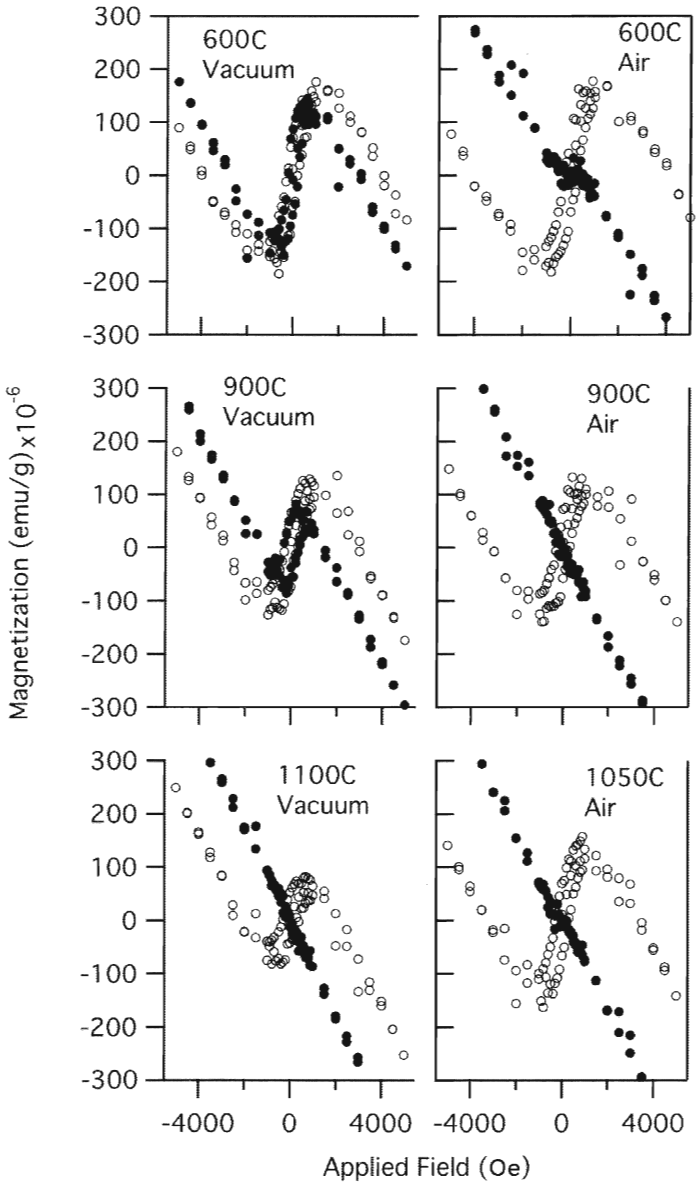

Figure 4.22: **$SrTiO_3$ substrates before (open circles) and after (closed circles) annealing (air or vacuum) at select temperatures, in normalized units (emu/g).**

Mass (mg±0.2)	Experiment	Ferromagnetic Saturation Moment ($\frac{emu}{g}$)
61.5	Iron Contamination	3.5×10^{-4}
64.2	Oxidization at 1000°C	4×10^{-5}

Table 4.3: Mass changes with respect to experimental procedure and net change in ferromagnetic moment for one face polished CRS-015.

Material	Magnetic Order	T_c or T_N (K)	M_{sat}(300°K) $\frac{emu}{g}$	References
Fe	Ferromagnetic	1043	220	[43]
FeO	Antiferromagnetic	200	0[a]	[44]
Fe_3O_4	Ferrimagnetic	858	30-90	[43, 45, 46, 47]
γ-Fe_2O_3	Ferrimagnetic	878	50-75	[47]
α-Fe_2O_3	Antiferromagnetic	955	0.5[a]	[48, 49]

Table 4.4: Properties of iron and iron oxides. [a]The magnetization of α-Fe_2O_3 does not saturate. The value listed is for T=295 K and H=1T , well above any fields used in this thesis.

changes in CRS-015 before and after oxidization. After oxidization several features were observed: the yellowing of the sample, the increase in mass and the reduction in the ferromagnetic moment. This increase in mass during oxidization was separately observed in other $SrTiO_3$ samples which also went yellow. This feature was not observed with reduced samples. One possible cause for this change in the properties of the sample would be from rusting of surface iron. As iron changes into certain types of rust it would lose its ferromagnetic nature, change in colour, and it would increase in mass as it would attract additional oxygen atoms. A summary of iron oxide properties can be seen in table 4.4. A further summary of visual measurements on the annealed samples can be seen in appendix B.

4.9 X-ray Diffraction Measurements

X-ray diffraction measurements (as described in section 3.2) were done on both single crystal $SrTiO_3$ and powdered $SrTiO_3$. As sample CRS-003 possessed both a polished and unpolished face it was an excellent candidate for x-ray diffraction. The difference in these surfaces is important for x-ray diffraction measurements as the penetration depth of the incident x-rays is of the order of 10μm. Figure 4.23 shows x-ray diffraction data for the single crystal with the counts having a log scale. Three clear peaks can be seen which correspond to the (100), (200) and (300) lattice planes respectively. The locations ($2\theta \approx 22.77°$, 46.48°, and 72.57°) of these lines agree with previous measurements from the International Centre for Data Diffraction. The inset in figure 4.23 shows in more detail the effect of surface polishing. It can be clearly observed that the unpolished side of the single crystal $SrTiO_3$ has a larger line width than the polished side. This broadening of the diffraction lines show that there is more crystalline disorder on the unpolished side than the polished side as mentioned in section 3.2. Figure 4.24 shows the x-ray results for the $SrTiO_3$ powder as received. These peaks agree with what theory (section 3.2) predicts as well as what is listed by the International Centre for Data Diffraction. Other potential peaks can be observed (for example around 26°) however their relative intensities are approaching the noise threshold. As a result these potential peaks could be either noise artifacts or impurities present in the $SrTiO_3$ powder.

Annealing in either air of vacuum effects the x-ray peak linewidth on the unpolished side. The upper panel of figure 4.25 shows the (003) line and the effects of annealing. This graph shows that when the sample is annealed (regardless of environment) the amount of disorder/stress/strain present on the unpolished face of the sample decreases. The lower panel then plots the full width at half maximum (as

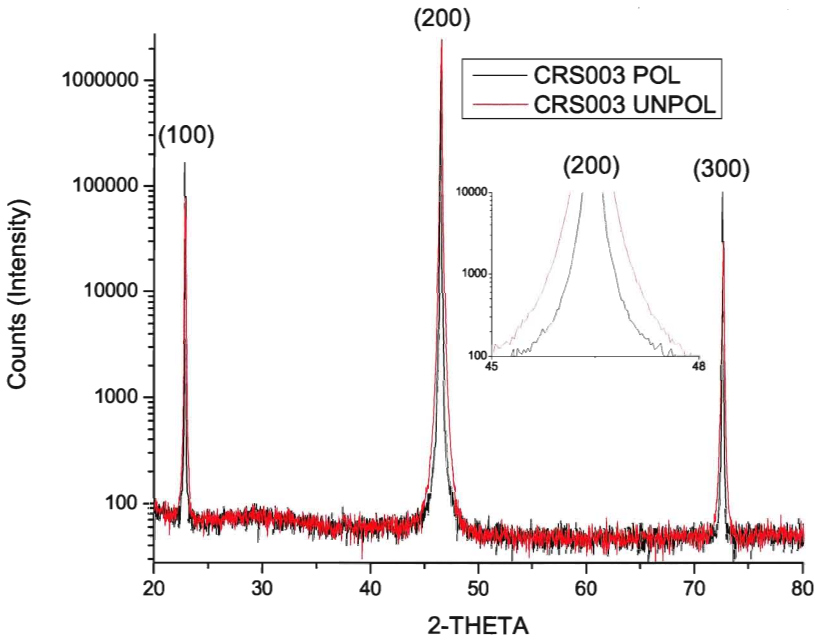

Figure 4.23: **Single crystal $SrTiO_3$ x-ray diffraction for the polished and unpolished faces.**

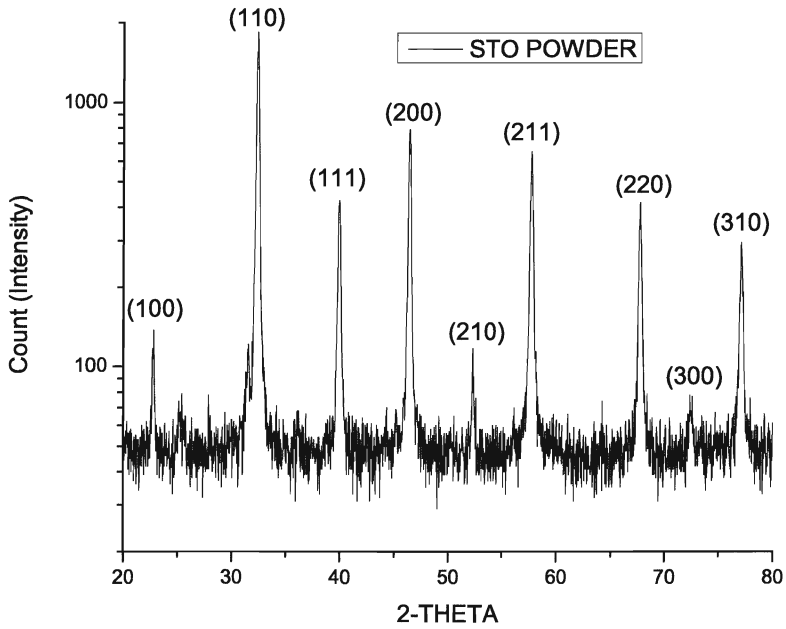

Figure 4.24: **$SrTiO_3$ powder x-ray diffraction.**

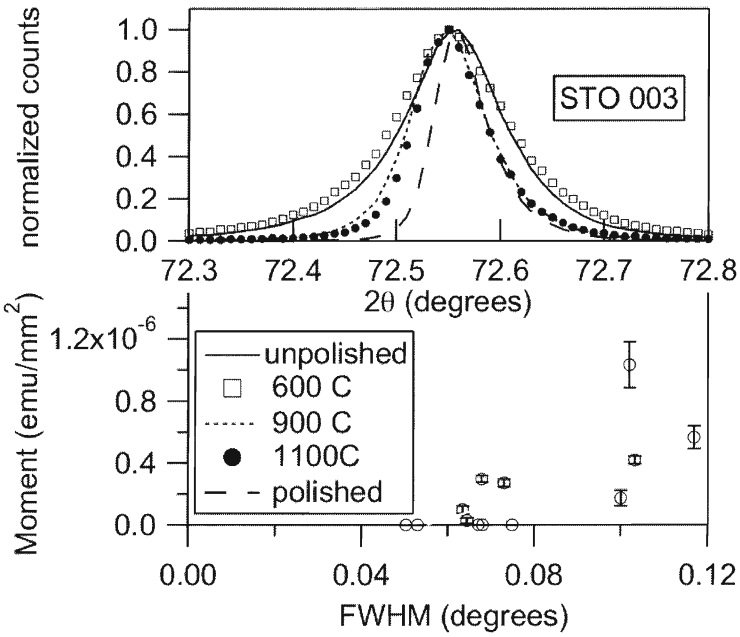

Figure 4.25: **(Upper) Effect of annealing on full width at half maximum (peak 003) on unpolished surfaces (unless otherwise listed). (Lower) Remanent moment (295°K) versus full width at half maximum (003 peak) of various annealed (air and vacuum) samples.**

mentioned in section 3.2) versus the measured magnetic moment. This plot slows a weak relation between measured magnetic moment and disorder in the crystal.

4.10 Effects of Argon Ion Bombardment

In order to further explore the effect of surface disorder on the magnetic properties of $SrTiO_3$ ion bombardment was used. Ar ions were put through a potential of 45kV (yielding energies of 10keV for Ar^+ and 90keV for Ar^{2+}) and sputtered over a polished face of the target sample. Care was taken to mount the samples using non-

ferromagnetic adhesive to prevent contamination. Approximate penetration depth calculations were done using SRIM (The Stopping and Range of Ions in Matter, www.srim.org) and suggested that for the ions and samples we would be using we could expect a large number of vacancies to be created. The upper portion of figure 4.26 shows one example of a SRIM calculation for 10KeV Ar^+ ions into $SrTiO_3$. Of note is the ion (penetration) range at 92Å as well as the vacancies induced per ion at 104.4. While both of these are approximate numbers averaged out over the 20,000 ions calculated they suggest that ion bombardment at this energy will induce a large volume of vacancies located at the surface of the sample. The lower portion of figure 4.26 shows the magnetic moment of a two face polished $SrTiO_3$ sample after being bombarded with approximately 10^{17}, 10KeV Ar^+ ions. This figure shows that a considerable amount of ion bombardment has little (if any) effect on the magnetic properties of the sample. Multiple samples were prepared with different amounts and energies of Ar^+ ions and showed the same result.

4.11 Effects of Acid Etching

Prior experimental results have shown that the ferromagnetism originated on the surface of the $SrTiO_3$ substrates. One explanation of this ferromagnetism was that trace amounts of iron were present on the surface of the sample, with origins similar to that mentioned in reference [19]. A quick look at the relative hardness of both $SrTiO_3$ (6-6.5 on the mohs scale) and stainless steel (5-6 on the mohs scale) shows that is it possible for the $SrTiO_3$ to scratch off potentially ferromagnetic particles from various stainless steel tools it would come into contact with, such as tweezers. Thus, acid etching experiments were conducted on the $SrTiO_3$ samples in order to remove trace amounts of iron (or other ferromagnetic contaminants). In order to perform

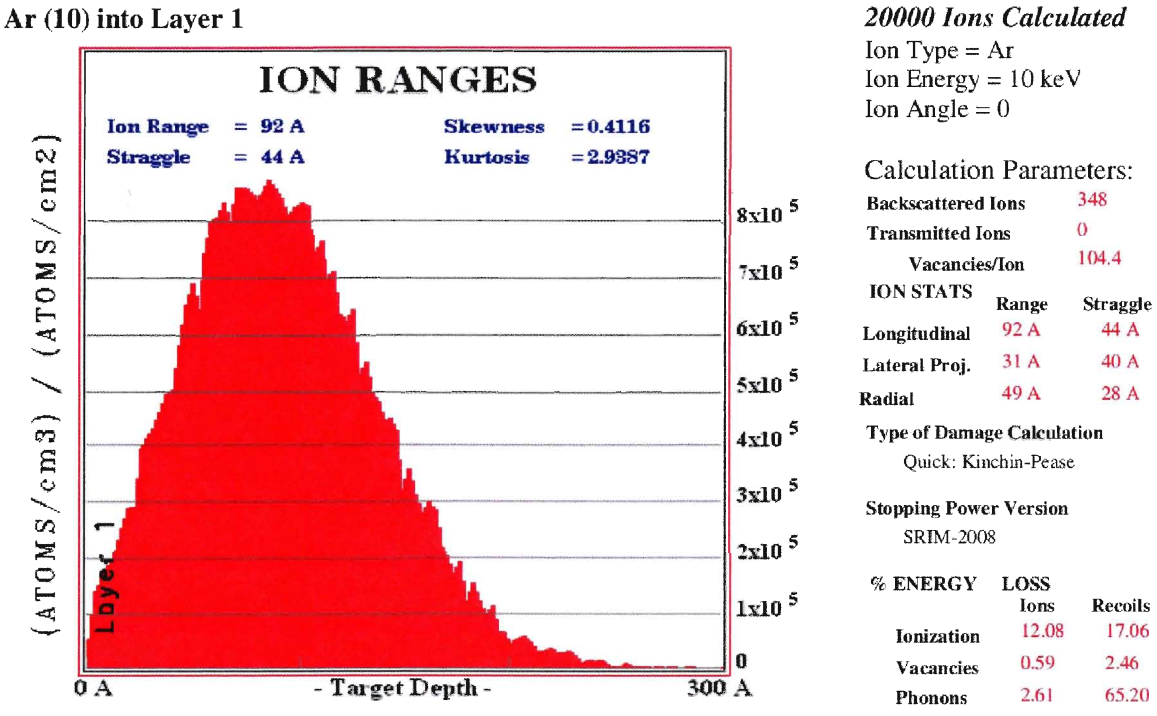

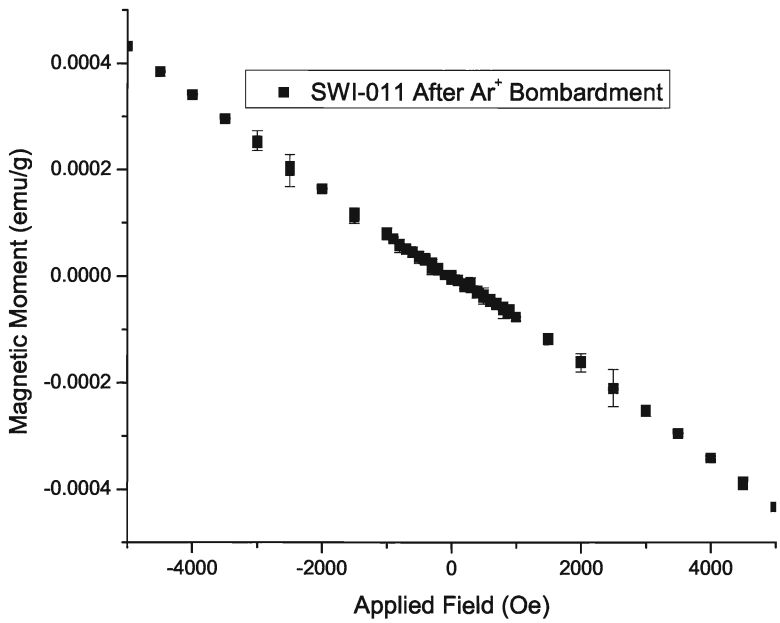

Figure 4.26: **Ar^+ ion penetration depth (approximate) for 10KeV in $SrTiO_3$ (Upper). Effect of Ar^+ Bombardment on two face polished $SrTiO_3$ (Lower), in normalized units (emu/g).**

Time (Minutes)	Mass of CRS-031 (mg±0.2) HNO_3 ($\sim 15.8 \frac{mol}{L}$)	Mass of CRS-014 (mg±0.2) HCl ($\sim 11.7 \frac{mol}{L}$)
0	61.6	61.5
10	61.3	61.4
20	61.3	61.3
30	61.2	61.3
60	61.2	61.2
90	61.2	61.2
120	61.2	61.1
600	61.1	60.9

Table 4.5: Mass changes with respect to time for nitric acid and hydrochloric acid on one face polished $SrTiO_3$ substrates.

the etching the samples were placed in beakers of acid and placed in an ultrasonic cleaner to ensure that the etching was thorough and that any debris removed from the surface of the samples was shaken clear. Table 4.5 shows the effect of acid etching on two one face polished $SrTiO_3$ substrates which had a measureable ferromagnetic moment. The purpose of this initial acid etching test was to determine if the acid(s) would remove a noticeable amount of mass from the sample and if there was a large difference between nitric and hydrochloric acid. As can be seen in table 4.5 there is a significant change in mass of the samples when etched with acid, however given a considerable amount of time there is little difference between the two different acids.

Acid etching experiments further supported that the source of ferromagnetism on the surface of $SrTiO_3$ originated from iron contamination. Sample MTI-001 (which previously had all sides and faces polished, figure 4.5) was ion bombarded, however proper handling procedure was not observed and the sample was mounted using a

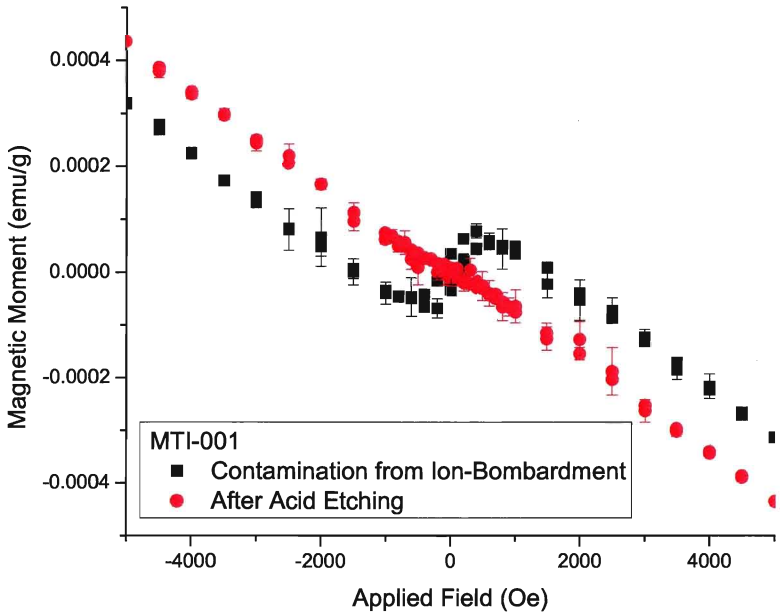

Figure 4.27: **MTI-001 with ion bombardment (iron contaminated) and after acid etching, in normalized units (emu/g).**

stainless steel screw. Table 4.6 shows the results of a nitric acid cleaning on the sample. This measureable loss in mass had a significant effect on the magnetic moment of the sample as seen in figure 4.27. This reduction in moment suggests a direct relation between the mass lost through acid etching to be the source of the measured magnetic moment. This loss in magnetic moment after acid cleaning has been tested to be repeatable and examples can be seen in appendix A. Similarly the opposite has also been observed, an increase in magnetic moment after deliberately contaminating a sample with stainless steel tweezers. Also included in table 4.6 are mass losses for an as-purchased two face polished substrate (CRS-028) which shows a slight loss in mass and a legacy sample STO-D which shows a similar mass decrease to other samples which had a significant ferromagnetic moment. Figure 4.28 shows the variations

Time (Minutes)	MTI-001 (mg±0.2) HNO_3 ($\sim 15.8 \frac{mol}{L}$)	CRS-028 (mg±0.2) HNO_3 ($\sim 15.8 \frac{mol}{L}$)	STO-D (mg±0.2) HNO_3 ($\sim 15.8 \frac{mol}{L}$)
0	117.8	126.8	52.9
10	117.4	126.7	52.6
20	117.4	126.7	52.6
30	117.3	126.6	52.5
60	117.3	126.6	52.5
90	117.4	126.6	52.5
120	117.3	126.5	52.5
1080	117.3	126.5	52.4

Table 4.6: Mass changes with respect to time for two face polished $SrTiO_3$ substrates with (MTI-001) and without (CRS-028) four side polishing. Also showing the mass change in highly reduced STO-D.

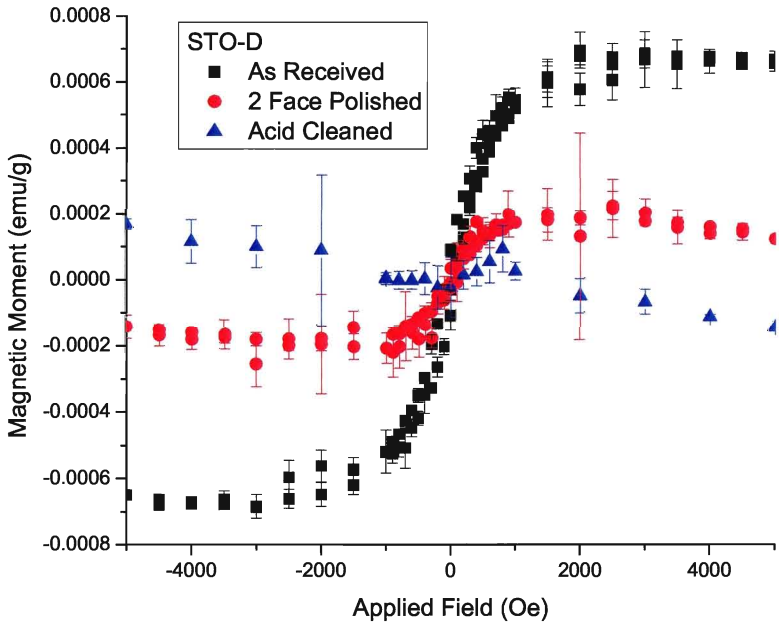

Figure 4.28: **Magnetic moment of legacy (inherited) sample STO-D after polishing and acid etching, in normalized units (emu/g).**

in magnetic moment when a heavily ferromagnetic $SrTiO_3$ sample is subject to both polishing and acid etching. These results along with those from figures 4.4 and 4.5 suggest that polishing the second face of the crystal does remove the bulk of the contamination however the four sides of the crystal must be polished or an acid cleaning is required to completely remove the surface contamination.

Chapter 5

Conclusions

All two face samples (as purchased) possessed diamagnetic susceptibilities which agreed with those found previously by reference [42]. At the same time each of these samples possessed a slightly different ferromagnetic contribution which could be viewed through the procedure outlined in section 2.2. These early results suggest that the manufacturing procedure for these crystals could lead to sample dependent properties, which agrees with findings suggested by reference [29]. This difference in the 'as purchased' samples becomes more evident in one face polished samples and can be easily seen in figure 4.3. It was also found that one face samples possess more ferromagnetism than two face polished samples which can be seen in figure 4.4. This suggests that the ferromagnetism measured is directly related to the rough surface. Hence the ferromagnetic signal can also originate from the four sides of the substrate. Figure 4.5 shows the effect of manually polishing the four sides of an as purchased crystal. This result strongly suggests that the ferromagnetism originates from surface contamination.

Previous findings which were conducted on sapphire substrates were able to isolate this spontaneous ferromagnetism to a surface effect [50]. The ferromagnetic response from the Al_2O_3 was measured and the surface was scanned with particle induced x-ray emission (PIXE) to check for surface impurities. While iron was measured on both surfaces, it was found to be more concentrated on the unpolished surface ($\sim 230\frac{ng}{cm^2}$ for unpolished, $\sim 10\frac{ng}{cm^2}$ for polished). It was found that the mass of iron found was

sufficient to create the ferromagnetic moment measured in most but not all samples, however a simple correlation was not possible [50]. To approximate the amount of surface iron present on the unpolished $SrTiO_3$ substrates we worked backwards from the measured moment and unpolished surface area (figure 4.6) using a value of $220\frac{emu}{g}$ for the saturation magnetization of iron [43]. This analysis give us an approximate value $190\frac{ng}{cm^2}$ which agrees with the value measured for Al_2O_3 [50]. Once again this amount of surface iron is sufficient to generate the ferromagnetic signals measured.

This hypothesis is further supported by the reduction and oxidizing experiments which were conducted. The aim of these annealing experiments was to decrease the surface disorder of the samples and in the case of reduction to create an excess of free carriers. It was found that these free carriers were created (figure 4.18). However, there was no creation of any ferromagnetism as seen in figures 4.16 and 4.21 for reduction and oxidization respectively. This same effect can be seen more clearly in figure 4.22 which shows a direct comparison between annealing in vacuum and air. While this contradicts previous work done (figure 1.9) it was found to be repeatable over multiple sets of experiments which can be seen in appendix A. As the measurements that led to figure 1.9 were done before careful attention was paid to iron contamination, this furthur highlights the need for careful handling of $SrTiO_3$ substrates.

In a further attempt to induce a defect or vacancy based ferromagnetism in $SrTiO_3$ several samples were subject to Ar ion bombardment. Calculations from SRIM suggested that the penetration depth of the ions would be roughly 92Å with a large number of vacancies being created (figure 4.26). However, three samples being bombarded with an increasingly greater number of higher energy ions yielded no change in the ferromagnetic moment (the result for the highest ion energy sample being visible in figure 4.26). These results combined with those from sample reduction strongly

support the hypothesis that ferromagnetism can not be induced in $SrTiO_3$ through oxygen vacancies.

To more conclusively test the iron contamination originating from the stainless steel tweezers as suggested by previous work on similar substrates [19] several samples were deliberately contaminated and subsequently etched in acid (either HCL or HNO_3) to remove the introduced iron. It was found that when a non-ferromagnetic sample was rubbed with steel tweezers (to simulate heavy handling of the sample) a ferromagnetic moment was created. This contamination induced moment was similar in magnitude to that of the (as purchased) one face polished samples. It was also found that this induced contamination had a similar behavior (loss of ferromagnetic moment) in an air annealing environment. This contamination can originate from sources other then tweezers, for example figure 4.27 shows the effect of acid etching on a sample which had been contaminated via a stainless steel mounting screw. As one would expect this contamination can be measured (mass) as it is added and removed as seen in table 4.6.

In conclusion it appears that ferromagnetism in strontium titanate was the result of sample contamination. As purchased strontium titanate single crystals should be cleaned (acid etched) prior to use to remove processing and handling based contaminants. Failure to properly prepare the strontium titanate could lead to spurious bulk property measurements of thin films grown on these substrates. Several potential sources of ferromagnetism were tested on numerous $SrTiO_3$ samples all of which failed to induce a ferromagnetic response. It has been found that in accordance with theory, pure strontium titanate behaves as a diamagnet, with Pauli paramagnetic contributions to magnetic susceptability added by reducing the crystals at higher temperatures.

Appendix A

Summary of SQUID Measurements

Mass(mg)	Sample	χ ($\frac{emu}{Oe \cdot g}$)	FM Sat. ($\frac{emu}{g}$)	Sample Notes
23.3	Al-Chunk	5.56E-07	1.50E-04	Aluminum from pellet die
23.0	Black-Chunk	-4.57E-07	4.00E-04	Black plastic from pellet die
126.6	CRS-001-1	-9.39E-08	3.00E-05	2 FP unmodified sample
122.6	CRS-001-2	-8.94E-08	4.00E-06	2 FP unmodified sample
127.2	CRS-002-1	-9.59E-08	3.00E-05	2 FP unmodified sample
127.2	CRS-003-1	-9.26E-08	2.00E-04	1 FP unmodified sample
62.1	CRS-003-2	-9.91E-08	1.50E-04	1.5 hrs of Ultrasonic Cleaning
62.1	CRS-004-1	-8.59E-08	4.50E-04	1 FP unmodified sample
62.1	CRS-004-2	-8.29E-08	4.50E-04	1 FP unmodified sample (5°K)
60.5	CRS-004-3	-8.51E-08	8.00E-05	2 FP unmodified sample
61.7	CRS-007-1	-8.53E-08	2.50E-04	1 FP unmodified sample
61.5	CRS-008-1	-7.72E-08	2.00E-04	1 FP unmodified sample
61.3	CRS-010-1	-9.12E-08	2.50E-04	1 FP unmodified sample
61.3	CRS-010-3	-9.20E-08	1.00E-04	1 FP, (R)900°C
61.8	CRS-011-1	-8.63E-08	2.50E-04	1 FP unmodified sample
61.8	CRS-011-2	-8.48E-08	7.00E-05	1 FP,(R)1000°C
61.7	CRS-012-1	-8.83E-08	2.00E-04	1 FP unmodified sample
61.7	CRS-012-2	-8.38E-08	1.00E-04	1 FP, (R)1000°C
62.7	CRS-013-1	-4.20E-08	2.50E-04	1 FP unmodified sample
61.6	CRS-013-2	-8.49E-08	1.00E-04	1 FP, Nitric acid cleaned

Mass(mg)	Sample	χ ($\frac{emu}{Oe \cdot g}$)	FM Sat. ($\frac{emu}{g}$)	Sample Notes
61.5	CRS-014-1	-8.29E-08	3.00E-04	1 FP unmodified sample
61.5	CRS-014-2	-7.53E-08	2.00E-04	1 FP, (R)600°C
61.5	CRS-015-1	-7.87E-08	3.00E-04	1 FP unmodified sample
–	CRS-015-2	-7.91E-08	5.00E-05	1 FP, (O)600°C
–	CRS-015-3	-9.29E-08	3.50E-04	After tweezer rub
64.2	CRS-015-4	-8.97E-08	4.00E-05	(O)1000°C
60.9	CRS-016-1	-7.93E-08	2.00E-04	1 FP unmodified sample
60.9	CRS-016-2	-8.72E-08	1.50E-04	1 FP, (R)900°C
61.3	CRS-017-1	-7.49E-08	2.50E-04	1 FP unmodified sample
62.0	CRS-017-2	-8.48E-08	4.00E-06	1 FP, (O)900°C
61.8	CRS-018-1	-8.51E-08	2.00E-04	1 FP unmodified sample
61.8	CRS-018-3	-9.31E-08	1.50E-05	1 FP, (R)1100°C
61.8	CRS-019-1	-8.26E-08	2.50E-04	1 FP unmodified sample
62.3	CRS-019-2	-8.92E-08	2.00E-05	1 FP, (O)1050°C
61.9	CRS-020-1	-9.81E-08	4.00E-04	1 FP unmodified sample
61.9	CRS-020-3	-4.33E-08	2.00E-04	1 FP, (R)700°C
61.9	CRS-022-1	-8.10E-08	3.50E-04	1 FP unmodified sample
61.9	CRS-022-2	-4.12E-08	1.50E-04	1 FP, (R)900°C
60.7	CRS-023-1	-7.91E-08	3.50E-04	1 FP unmodified sample
60.9	CRS-023-2	-7.32E-08	5.00E-05	1 FP, (O)900°C
61.4	CRS-024-1	-8.64E-08	2.50E-04	1 FP unmodified sample
61.4	CRS-024-2	-9.87E-08	8.00E-05	1 FP, (R)1100°C
61.6	CRS-025-1	-5.31E-08	4.00E-04	1 FP unmodified sample
63.4	CRS-025-2	-9.43E-08	6.00E-05	1 FP, (O)1100°C
61.8	CRS-026-1	-1.09E-07	4.50E-04	1 FP unmodified sample
61.9	CRS-026-2	-8.96E-08	1.00E-04	1 FP, (O)700°C

Mass(mg)	Sample	χ ($\frac{emu}{Oe \cdot g}$)	FM Sat. ($\frac{emu}{g}$)	Sample Notes
61.3	CRS-027-1	-1.21E-07	5.00E-04	1 FP unmodified sample
61.3	CRS-027-2	-8.67E-08	1.50E-04	1 FP, (R)600°C
61.7	CRS-031-1	-9.10E-08	3.50E-04	1 FP unmodified sample
61.4	CRS-031-2	-4.43E-08	5.00E-04	Acid cleaned then tweezer rub
58.8	Gelcap-1	-3.53E-07	8.00E-05	Number 2 Gelcap
55.6	Gelcap-3	-3.33E-07	5.00E-05	Number 2 Gelcap
133.1	MTI-001-1	-9.07E-08	7.00E-05	2 FP unmodified sample
133.1	MTI-001-2	-9.43E-08	3.00E-05	2 FP unmodified sample
117.8	MTI-001-3	-8.61E-08	1.50E-05	2 FP and 4 Sides Polished
–	MTI-001-4	-9.31E-08	1.50E-04	After Ar^+ Sputtering
117.4	MTI-001-5	-9.10E-08	2.00E-05	After Acid Cleaning
132.1	MTI-002-1	-9.33E-08	2.00E-05	2 FP unmodified sample
59.7	$Nb_{0.007}$-01-1	-3.74E-08	2.50E-04	1 FP unmodified sample
56.1	$Nb_{0.007}$-02-1	-5.48E-08	1.00E-06	2 FP
70.3	$Nb_{0.01}$-01-1	-3.18E-08	1.00E-04	1 FP unmodified sample
67.4	$Nb_{0.01}$-01-5	-3.74E-08	5.00E-05	2 FP
61.5	$Nb_{0.01}$-02-1	-2.85E-08	5.00E-06	2 FP
492.4	Powder-1	-8.12E-08	4.00E-05	Powder (CAS:12060-59-2)
188.6	PP-02-1	-6.07E-08	1.30E-04	Raw Pressed Pellet
187.0	PP-02-2	-5.57E-08	1.20E-04	PP-02, (R)700°C
271.2	PP-04-1	-7.79E-08	2.50E-04	Raw Pressed Pellet
265.2	PP-04-2	-5.34E-08	8.00E-05	PP-04, (R)1000°C
217.7	PP-05-1	-5.52E-08	8.00E-05	Raw Pressed Pellet
192.1	PP-05-2	1.05E-07	6.00E-04	PP-05, (R)900°C
192.1	PP-05-3	1.05E-07	6.00E-04	Repeat of PP-05-2
219.1	PP-06-1	-8.12E-08	5.00E-05	Raw Pressed Pellet

Mass(mg)	Sample	χ ($\frac{emu}{Oe \cdot g}$)	FM Sat. ($\frac{emu}{g}$)	Sample Notes
213.2	PP-06-2	-7.81E-08	3.00E-05	PP-06, (R)1100°C
195.7	PP-07-2	-7.06E-08	4.00E-05	Raw Pressed Pellet
190.7	PP-07-3	-6.70E-08	6.00E-05	PP-07, (R)600°C
236.2	PP-08-1	-7.50E-08	2.00E-05	Raw Pressed Pellet
230.9	PP-08-2	-7.24E-08	5.00E-05	PP-08, (R)800°C
250.5	PP-09-1	-7.86E-08	4.00E-05	Raw Pressed Pellet
246.7	PP-09-2	-7.44E-08	2.50E-05	PP-09, (R)900°C
63.2	STO-C-1	-8.49E-08	8.00E-05	No Faces Polished
62.2	STO-C-2	-8.74E-08	5.00E-05	$\frac{1}{2}$ of 1FP
66.3	STO-D-1	n/a	7.00E-04	1 FP, (R) with Ti
63.9	STO-D-2	n/a	1.50E-04	2 FP, divot still present
52.8	STO-D-4	-3.60E-08	8.50E-05	2 FP and 4 Sides Polished
52.4	STO-D-5	-3.55E-08	3.00E-05	STO-D-4 Acid Cleaned
127.9	STO-E-1	-8.31E-08	2.50E-04	1 FP, (R)
126.1	STO-E-2	-8.63E-08	1.00E-04	2 FP
117.3	STO-E-3	-8.96E-08	4.00E-05	2 FP and 4 Sides Polished
124.7	STO-I-1	-9.73E-08	5.00E-05	1 FP, as Received
122.3	STO-I-2	-9.64E-08	1.00E-05	2 FP
122.0	SWI-001-1	-9.94E-08	2.00E-05	2 FP unmodified sample
116.9	SWI-002-1	-9.91E-08	4.00E-05	2 FP unmodified sample
116.9	SWI-002-2	-9.67E-08	1.50E-05	2 FP unmodified sample
116.9	SWI-002-3	-8.48E-08	3.00E-05	2 FP unmodified sample (5°K)
108.3	SWI-002-5	-9.56E-08	3.00E-05	1 FP, 1 Face Rough
108.3	SWI-002-6	-8.19E-08	4.00E-05	SWI-002-5 After 1.5 Months
108.3	SWI-002-7	-8.88E-08	4.00E-05	SWI-002-5 After 2 Months
108.3	SWI-002-8	-9.03E-08	5.00E-05	SWI-002-5 After 5.5 Months

Mass(mg)	Sample	χ ($\frac{emu}{Oe \cdot g}$)	FM Sat. ($\frac{emu}{g}$)	Sample Notes
123.7	SWI-003-1	-8.76E-08	5.00E-05	2 FP, (R)600°C
119.9	SWI-004-1	-8.72E-08	6.00E-05	2 FP, (R)700°C
124.0	SWI-005-1	-9.43E-08	2.50E-05	2 FP, (R)800°C
123.7	SWI-006-1	-8.03E-08	1.10E-04	2 FP, (R)900°C
121.6	SWI-006-2	-8.53E-08	6.00E-05	2 FP, (O)900°C
121.5	SWI-006-3	-9.22E-08	9.00E-05	2 FP, (R)900°C
120.0	SWI-007-1	-7.84E-08	1.50E-05	2 FP, (R)1000°C
108.6	SWI-007-2	-8.43E-08	1.50E-05	2 FP and 4 Sides Polished
124.2	SWI-008-1	-8.00E-08	2.00E-06	2 FP, (R)1100°Cs
110.9	SWI-008-2	-8.66E-08	1.00E-06	2 FP and 4 Sides Polished
121.6	SWI-009-2	-7.83E-08	1.50E-05	2 FP, (R)900°C
110.3	SWI-009-3	-8.31E-08	1.00E-05	2 FP and 4 Sides Polished
121.5	SWI-011-3	-8.91E-08	1.50E-05	Heavily Ar^+ bombarded
123.0	SWI-012-2	-8.62E-08	1.00E-06	Ar^+ bombarded

Table A.1: Summary of SQUID measurements with (FP) face polished, (R) reduced, (O) Oxidized in air.

Appendix B

Pellet Reduction in Al_2O_3 Boats

During the course of the reduction experiments for this thesis several observations were made which may warrant further investigation. During the initial reductions of the two face polished single crystals it was seen that there was a gradual darkening of the crystals (as seen in figure 4.17). During the course of these reductions the same Al_2O_3 boat was used. It was noticed that the boat as purchased was a cream colour however after several reductions the boat appeared dirty, leaving behind a cleaner patch where the sample had been sitting. As both the substrate and boat were isolated in vacuum (approximately 5×10^{-6} Torr) inside a quartz tube the sources of origin for this dirt are very limited.

It was also observed that when a pellet made from pressed powder was reduced in a cream boat (dirty or otherwise) the boat itself would change to a bright white colour upon removal from the oven. It was found that when a single crystal was reduced in one of these bright white boats the previously observed darkening was not found. A summary of visual measurements on reduced samples for both cream and white boats can be seen in tables B.1 and B.2 respectively. Similarly, when samples were oxidized in both cream and white boats different visual observations were made as can be seen in tables B.3 and B.4 respectivly. It is interesting to note that the iridescence was visible in both cream and white boats which the colour change was not as severe. Also of note was the presence of side lines that formed on the faces of several samples. These side lines take the form of two dark stripes located on opposing sides of the

Name	Temperature (°C)	Colour	Polished Surface
CRS-027	600	Clear	Unchanged
CRS-020	700	Light grey	Unchanged
CRS-022	900	Light grey	Unchanged
CRS-011	1000	Grey	Unchanged
CRS-024	1100	Dark Grey	Unchanged

Table B.1: Visual observations for reduced samples in a cream Al_2O_3 boat.

face separated by a much larger undarkened stripe that occupied the center of the crystal face. While these lines were observed on the faces of a few samples, they were not consistently formed.

It should also be noted that prior to oxidization sample CRS-013 was cleaned with nitric acid, removing any potential surface impurities which may have contributed to the yellowing of the crystal. Conversely, sample CRS-015 was deliberatly contaminated with stainless steel tweezers and subsequently turned very yellow after being annealed in air. This would suggested that surface impurities are reacting during the annealing process leading to furthur corruption of the sample.

It was noticed that as samples were air annealed they tended to have a mass increase (visible in appendix A). Figure B.1 (upper panel) shows x-ray diffraction data for one of these air annealed samples that had turned yellow. There are several additional lines that are present and are quite distinct from the base $SrTiO_3$ lines. These lines were compared to known data for iron oxide(s) and a match could not be found.

Name	Temperature (°C)	Colour	Polished Surface
CRS-014	600	Clear	Scuffed
CRS-016	900	Clear	Unchanged
CRS-010	900	Clear	Unchanged
CRS-012	1000	Clear	Unchanged
CRS-018	1100	Very light grey	Unchanged

Table B.2: Visual observations for reduced samples in a white Al_2O_3 boat.

Name	Temperature (°C)	Colour	Polished Surface
CRS-026	700	Clear	Iridescent
CRS-023	900	Clear	Iridescent
CRS-015	1000	Very yellow	Not visible
CRS-025	1100	Grey with side lines	Not visible

Table B.3: Visual observations for oxidized samples in a cream Al_2O_3 boat.

Name	Temperature (°C)	Colour	Polished Surface
CRS-017	900	Light yellow	Iridescent
CRS-019	1050	Yellow with side lines	Iridescent
CRS-013	1100	Clear	Scuffed

Table B.4: Visual observations for oxidized samples in a white Al_2O_3 boat.

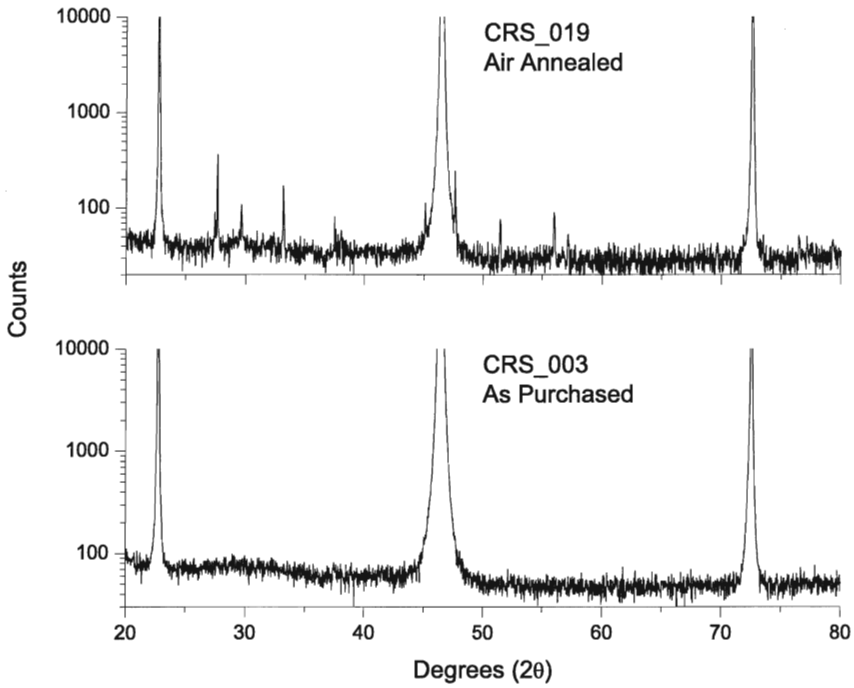

Figure B.1: **X-ray diffraction lines for as purchased single crystal (lower) and for air annealed single crystal (upper).**

Bibliography

[1] R.A. Buhrman J.M. Daughton S. von Molnár M.L. Roukes A.Y. Chtchelkanova S.A. Wolf, D.D. Awschalom and D.M. Treger. Spintronics: A Spin-Based Electronics Vision for the Future. *Science*, 2001.

[2] G.A. Prinz. Magnetoelectronics. *Science*, **282**.1660, 1998.

[3] G. Kirczenow. Ideal spin filters: A theoretical study of electron transmission through ordered and disordered interfaces between ferromagnetic metals and semiconductors. *Physical Review B*, **63**.054422, 2001.

[4] L.W. Molenkamp A.T. Filip G. Schmidt, D. Ferrand and B.J. van Wees. Fundamental obstacle for electrical spin injection from a ferromagnetic metal into a diffusive semiconductor. *Physical Review B*, **62**.R4790, 2000.

[5] D. Grundler. Ballistic spin-filter transistor. *Physical Review B*, **63**.161307, 2001.

[6] E.I. Rashba. Theory of electrical spin injection: Tunnel contacts as a solution of the conductivity mismatch problem. *Physical Review B*, **64**.R16267, 2000.

[7] R.N. Louie S.K. Upadhyay and R.A. Buhrman. Spin filtering by ultrathin ferromagnetic films. *Applied Physics Letters*, **74**.3881, 1999.

[8] S.D. Kim R. Vlutters P.S. Anil Kumar R. Jansen, O.M.J. van't Erve and J.C. Lodder. The spin-valve transistor: Fabrication, characterization, and physics (invited). *Journal of Applied Physics*, **89**.7431, 2001.

[9] S. Bandyopadhyay and M. Cahay. *Introduction to Spintronics.* CRC Press, 2008.

[10] M.I. Dyakonov. *Spin Physics in Semiconductors.* Springer, 2008.

[11] F. Matsukura A. Oiwa A. Endo S. Katsumoto H. Ohna, A. Shen and Y. Iye. (Ga,Mn)As: A new diluted magnetic semiconductor based on GaAs. *Applied Physics Letters*, **69**.363, 1996.

[12] P. Stamenov C.B. Fitzgerald J.M.D. Coey, M. Venkatesan and L.S. Dorneles. Magnetism in hafnium dioxide. *Physical Review B*, **72**.024450, 2005.

[13] S.B. Ogale L.F. Fu S.J. Welz N.D. Browning V. Zaitsev B. Varughese C.A. Cardoso A. Curtin S. Dhar S.R. Shinde T. Venkatesan S.E. Lofland M.S. Ramachandra Rao, D.C. Kundaliya and S.A. Schwarz. Search for ferromagnetism in undoped and cobalt-doped $HfO_{2-\delta}$. *Applied Physics Letters*, **88**.142505, 2006.

[14] D.W. Boukhvalov L.D. Finkelstein D.H. Kim T-W. Noh A. Moewes G.S. Chang, E.Z. Kurmaev and T.A. Callcott. Clustering of impurity atoms in Co-doped anatase TiO_2 thin films probed with soft x-ray fluorescence. *Journal of Physics: Condensed Matter*, **18**.4243, 2006.

[15] J.G. Keeth S.B. Ogale S.R. Shinde J.R. Simpson H.D. Drew S. Guha, K. Ghosh and T. Venkatesan. Temperature-dependent optical studies of $Ti_{1-x}Co_xO_2$. *Applied Physics Letters*, **83**.3296, 2003.

[16] S.W. Jung H-J. Kim G-C. Yi S-I. Lee M.V. Yablonskikh T.M. Pederson A. Moewes G.S. Chang, E.Z. Kurmaev and L.D. Finkelstein. Local electronic structure of Mn dopants in ZnO probed by resonant inelastic x-ray scattering. *Journal of Physics: Condensed Matter*, **19**.276210, 2007.

[17] D.W. Boukhvalov L.D. Finkelstein S. Colis-T.M. Pedersen A. Moewes G.S. Chang, E.Z. Kurmaev and A. Dinia. Effect of Co and O defects on the magnetism in Co-doped ZnO: Experiment and theory. *Physical Review B*, **75**.195215, 2007.

[18] A. Bakin A. Waag H. Ahlers U. Siegner S. Sievers M. Albrecht W. Schoch N. Izyumskaya V. Avrutin S. Sorokin S. Ivanov A.C. Mofor, A. El-Shaer and J. Stoimenos. Magnetic property investigations on Mn-doped ZnO layers on sapphire. *Applied Physics Letters*, **87**.062501, 2005.

[19] M. Frank D. Abraham and S. Guha. Absence of magnetism in hafnium oxide films. *Applied Physics Letters*, **87**.252502, 2005.

[20] N. Rangarajan U. Siddesh A. Sundaresan, R. Bhargavi and C.N.R. Rao. Ferromagnetism as a universal feature of nanoparticles of the otherwise nonmagnetic oxides. *Physical Review B*, **74**.161306, 2006.

[21] A. Henry. Magnetic Properties of Pure and Reduced Strontium Titanate. Bachelor's thesis, Bachelor of Science, Brock University, 2008.

[22] M.M. Yazdanian. Preparation of $SrMg_xRu_{1-x}O_3$ Thin Films by Pulsed Laser Deposition. Master's thesis, Master of Science, Brock University, 2004.

[23] K. Szot and W. Speier. Surfaces of reduced and oxidized $SrTiO_3$ from atomic force microscopy. *Physical Review B*, **60**.5909, 1999.

[24] Y. Zhu R. Wang and S.M. Shapiro. Structural Defects and the Origin of the Second Length Scale in $SrTiO_3$. *Physical Review Letters*, **80**.2370, 1998.

[25] R. Carius U. Zastrow K. Szot, W. Speier and W. Beyer. Localized Metallic Conductivity and Self-Healing during Thermal Reduction of $SrTiO_3$. *Physical Review Letters*, **88**.075508, 2002.

[26] J. Herion K. Szot, W. Speier and Ch. Freiburg. Restructuring of the surface region in $SrTiO_3$. *Applied Physics A*, **64**.s003390050443, 1996.

[27] O. Bunk C.M. Schlepütz B.D. Patterson R. Herger, P.R. Willmott and B. Delley. Surface of Strontium Titanate. *Physical Review Letters*, **98**.076102, 2007.

[28] C. Dreher C.C. Homes A.W. McConnell B.P. Clayman W.H. Gong D.A. Crandles, B. Nicholas and J.E. Greedan. Optical properties of highly reduced $SrTiO_{3-x}$. *Physical Review B*, **59**.12842, 1999.

[29] K. Shibata A. Ogi T. Konya S. Mochizuki, F. Fujishiro and K. Inaba. Optical, electrical, and X-ray-structural studies on Verneuil-grown $SrTiO_3$ single crystal: Annealing study. *Physica B: Condensed Matter*, **10**.1016, 2007.

[30] K. Ishiwata, S. Mochizuki, F. Fujishiro and K. Shibata. Optical properties of highly reduced $SrTiO_{3-x}$. *Physica B*, **376**.816, 2006.

[31] P. Hartman. *Crystal Growth: An Introduction.* North-Holland publishing company, 1973.

[32] US Patent Number 5518776, 1996.

[33] US Patent Number 4487755, 1984.

[34] B.D. Cullity and C.D. Graham. *Introduction to Magnetic Materials, Second Edition.* IEEE Press & Wiley, 2009.

[35] K.H.J. Buschow and F.R. De Boer. *Physics of Magnetism and Magnetic Materials.* Kluwer Academic Publishers, 2003.

[36] J. Clarke and A.I. Braginski. *The SQUID Handbook, Vol. 1.* Wiley-VCH, 2004.

[37] B.D. Cullity and S.R. Stock. *Elements of X-Ray Diffraction, Third Edition.* Prentice Hall, 2001.

[38] I. Lucks, P. Lamparter and E.J. Mittemeijer. An evaluation of methods of diffraction-line broadening analysis applied to ball-milled molybdenum. *Journal of Applied Crystallography*, **37**.S0021889804003140, 2004.

[39] P.J. Potts. *A Handbook of Silicate Rock Analysis.* Blackie and Son Ltd., 1987.

[40] P.Y. Yu and M. Cardona. *Fundamentals of Semiconductors.* Springer, 2001.

[41] B.C. Smith. *Fundamentals of Fourier Transform Infrared Spectroscopy.* CRC Press, 1996.

[42] H.P.R. Frederikse and G.A. Candela. Magnetic Susceptibility of Insulating and Semiconducting Strontium Titanate. *Physical Review*, **147**.583, 1966.

[43] Charles Kittel. *Introduction to Solid State Physics, 5th ed.* John Wiley and Sons, 1975.

[44] C.J. Chen R.K. Chiang, H.Y. Lai and C.R. Lin. Characterization of Monodisperse Wüstite Nanoparticles following Partial Oxidation. *Journal of Physical Chemestry*, **114**.4258, 2010.

[45] F.C. Fonseca G.F. Goya, T.S. Berquó and M.P. Morales. Static and dynamic magnetic properties of spherical magnetite nanoparticles. *Journal of Applied Physics*, **90**.3520, 2003.

[46] I.A. Presnyakov R.J. Gambino V.S. Zaitsev, D.S. Filimonov and B. Chu. Physical and chemical properties of magnetite and magnetite-polymer nanoparticles and their colloidal dispersions. *Journal of Colloid and Interface Science*, **212**.49, 1999.

[47] R. Strobel and S.E. Pratsinis. Direct synthesis of maghemite, magnetite and wustite nanoparticles by flame spray pyrolysis. *Advanced Powder Technology*, **20**.190, 2009.

[48] C.B. Koch K. Lefmann F. Bødker, M.F. Hansen and S. Mørup. Magnetic properties of hematite nanoparticles. *Physical Review B*, **61**.6826, 2000.

[49] S.T. Lin. Magnetic properties of hematite single crystals. i. magnetization isotherms, antiferromagnetic susceptibility, and weak ferromagnetism of a natural crystal. *Physical Review*, **116**.1447, 1959.

[50] P. Esquinazi R. Höhne A. Setzer K. Schindler H. Schmidt R. Salzer, D. Spemann and T. Butz. Possible pitfalls in search of magnetic order in thin films deposited on single crystalline sapphire substrates. *Journal of magnetism and magnetic materials*, **317**.53-60, 2007.